ALGORITHM FOR REMOTE SENSING OF TROPOSPHERIC AEROSOL FROM MODIS

Product ID: MOD04

Revised October 26, 1998

Yoram J. Kaufman[1] and Didier Tanré[2]

Points of contact: A. Chu[3], S. Mattoo[4], and L. A. Remer[1]

[1] NASA Goddard Space Flight Center, Code 913, Greenbelt, MD 20771, USA

[2] Laboratoire d'Optique Atmospherique, Université de Sciences et Techniques de Lille, Villeneuve d'Ascq, France, on frequent visits to NASA/GSFC

[3] Science Systems and Applications, Inc. (913), NASA/GSFC, Greenbelt, MD 20771, USA.

[4] Space Application Corporation/ARD (913), NASA/GSFC, Greenbelt, MD 20771, USA

This document describes the algorithms for simultaneous remote sensing of aerosol from EOS-MODIS over land and ocean. The algorithm will be used to monitor the aerosol optical thickness (proportional to the aerosol total loading) and size distribution (integrated on the vertical column) of the ambient (undisturbed) aerosol, over most of the globe (oceans and the moist parts of the continents) on a daily basis. The size distribution will be derived only over the oceans. These aerosol products will be used to monitor the aerosol mass concentration, optical properties, and radiative forcing.

At launch, over the land the aerosol optical thickness will be derived using the dark target approach. Therefore the method will be limited to the moist (and some semi-arid) parts of the continents excluding snow and ice cover. Dust will be sensed only over the ocean. Methods using contrast reduction, variation in the apparent brightness and IR remote sensing will be studied and implemented post launch. The algorithms take advantage of the MODIS wide spectral range and high spatial resolution with daily global coverage (e.g., 500 m at 0.47 to 2.13 μm with 250 m at 0.66 and 0.86 μm and 1 km at 3.8 μm). These unique MODIS characteristics should allow excellent cloud rejection while maintaining high statistics of cloud free pixels. The wide spectral range allows sophisticated derivation of aerosol size distribution over the ocean and efficient identification of pixels with dark surface cover over the land. The present algorithm as applied to the MODIS data should allow unprecedented capability of remote sensing of aerosol. Aerosol mass concentration per unit area will be derived. The aerosol information will be used to study aerosol climatology, to monitor the sources and sinks of specific aerosol types (e.g., sulfates and other industrial/urban aerosol and biomass burning aerosol), to serve as inputs for climate modeling and detection of the finger prints of anthropogenic climate change, and to perform atmospheric corrections of remotely sensed surface reflectance over the land.

Over the ocean the measured radiance in a wide spectral range (0.55-2.13 μm) is inverted into the aerosol optical thickness and volume distribution (in the range of 0.08-5 μm radius). In the inversion, it is assumed that the aerosol size distribution is bi-modal log-normal. The ratio between the log-normal modes and the mean particle size of the dominant mode are determined from the MODIS spectral radiances. Daily optical thicknesses, size parameters, and secondarily-derived parameters: the mass concentration, asymmetry parameter, backscattering ratio, Angstrom exponents, reflected flus, transmitted fluxes and the potential CCN concentration are stored on a resolution of 10x10 pixels (of 1 km nadir resolution).

Over the land, at launch, the algorithm uses the low opacity of most aerosol types in the mid-IR (2.13 and 3.8 μm) and the presence of many dark surface covers in the blue and red channels (0.47 and 0.66 μm). The dark pixels are identified using a correlation between the land reflectance in the mid IR and in the blue and red channels. For pixels that are identified to have low reflectance in the mid-IR, reflectance in the blue and red is estimated and used to derive the optical thickness in these two channels. Daily optical thickness and mass concentration are stored on a resolution of 10x10 pixels (of 1 km nadir resolution).

1. INTRODUCTION

The impact of atmospheric aerosols on the radiative budget has been broadly demonstrated (Coakley and Cess, 1985; Joseph 1984; Tanré et al., 1984, Charlson et al., 1992). Hansen and Lacis (1990) pointed out that one of the greatest source of uncertainties in climate modeling is due to aerosols. Radiative forcing by aerosol may explain the difference between the observed and modeled temperature trends. In fact, the interaction with solar and terrestrial radiation by aerosols perturbs the radiative budget via scattering and absorption of sunlight (Liou et al., 1978; Coakley et al, 1983). By acting as CCN (Cloud Condensation Nuclei) or IN (Ice Nuclei - Twomey and Warner, 1967; Hobbs and Locatelli, 1970; Charlson et al., 1987; Wigley, 1989; Hegg, 1990), aerosol particles also modify the cloud microphysics. As a result, aerosol particles may change the cloud radiative properties (Twomey 1977a; Twomey et al., 1984; Albrecht, 1989; Coakley et al., 1987; Radke et al., 1989; Kaufman and Nakajima, 1993). The direct effect of aerosol on radiation budget and the indirect effect on cloud albedo may cause a cooling effect that may counter balance the warming due to the increase in CO_2 concentration (Twomey et al., 1984; Wigley, 1989; Kaufman et al., 1991; Charlson et al., 1992). Present estimates of the aerosol forcing vary in a broad range from -0.6w/m^2 to -4.0w/m^2 if combining both the direct and indirect effects of sulfate aerosol (Charlson et al., 1992; Kaufman and Chou, 1993; Langner et al., 1992; Kiehl and Briegleb, 1993; Kaufman and Tanré, 1994) and biomass burning aerosol (Penner et al., 1992). Dust originated from local area change is also suspected to be a major forcing (Li et al., 1996; Tegen et al., 1996). The direct aerosol effect is due to direct reflection of sunlight to space by the aerosol particles and the indirect effect is by the modification of cloud properties, which in turn modifies the radiative budget. Recent paper shows the importance of inclusion of aerosol in climate model to find the finger prints of man made climate change (Santer et al., 1996).

Aerosol particles also play an important role in many biogeochemical cycles. Ocean serves a major source of natural aerosols like dimethylsulfide (DMS) produced by phytoplankton (Andreae and Barnard, 1984) and through air-sea exchange, it contributes greatly to the global cycles of carbon, nitrogen and sulphur aerosols (Duce, 1983). In addition to the contribution to the marine sulfur budget, DMS plays a significant role on the global climate as well (Charlson et al., 1987). Liquid water from ocean also can be transferred to the atmosphere through air bubbles at the surface as well as sea salt aerosols when water evaporates (Heathershaw, 1974; Fairall et al., 1983, Hoppel et al., 1990). Biomass burning is an important source of organic particles, while the arid and semi-arid regions are mainly the sources for mineral dust (Prospero, 1981; Pye, 1987). In tropospheric chemistry, aerosols also serves as the liquid phase that increases the speed of chemical reactions (Crutzen, 1983; Taylor et al., 1983).

To fully understand these processes, the aerosol characteristics (composition, size distribution and total content) have to be determined on a global scale, and only satellite approach, combining information from remote sensing over land and ocean, can achieve this objective. Since there is no simple way for obtaining the aerosol spectral information over the land, except for the limited range between the blue and the red channels over dense vegetation, the aerosol size distribution will be derived only over the ocean ($0.55\mu m \leq \lambda \leq 2.13\mu m$), while the aerosol total content (given by its optical thickness) will be derived from both over the ocean and large parts of the continents at representative wavelengths. It has been already demonstrated that the spectral dependence of the optical thickness carries out information on the aerosols size distribution (King et al., 1978). One can reasonably expect that the spectral dependence of the satellite signal (radiance) can be used in a similar way, though in some cases it is more difficult (Kaufman et al., 1990; Durkee et al., 1986, 1991) due to simultaneous wavelength variation of the optical thickness and the scattering phase function, both resulting from the composite radiance. The first description of the algorithm for MODIS was published as part of the review paper of the MODIS Atmospheric group (King et al., 1992). Recent reviews of remote sensing of aerosol and its radiative forcing is given by Kaufman (1995) and of the application of remote sensing of aerosol over the land for atmospheric corrections are summarized by Kaufman and Tanré (1996).

Aerosol should be routinely sensed over the land and ocean. Because the sources of most of the aerosols (mainly the anthropogenic aerosols) are over the land, the remote sensing of aerosol over the land is particularly important to test our understanding of the sources and transformations in the atmosphere and the anthropogenic contribution to these processes. According to Kiehl et al. (1993) and Jones et al. (1994), a large part of the radiative forcing is concentrated over the land as opposed to the ocean. The remote sensing of aerosols over the ocean is more accurate and informative due to the dark and uniform ocean reflectance (except glint). Oceans occupy 2/3 of the earth surface, and consequently interact with 2/3 of the solar radiation. A combination of simultaneous routine of sensing the aerosols over land and ocean is the key for the determination of the role of aerosol in the atmospheric environment and the role of human activity involved in the aerosol formation.

Due to the difference in the reflective properties of the surface under the semi-transparent aerosol layer, the aerosol retrieval algorithms over land and ocean are very different, so are the spectral channels used in the inversion. The sensitivity to the MODIS channel characteristics is also different as well as the assumptions and sources of errors. Therefore, they are developed as separate computer codes to accommodate these.

2. OVERVIEW AND BACKGROUND INFORMATION

2.1 Experimental Objective

The objective of this investigation is to monitor atmospheric aerosols over the land and ocean simultaneously. The aerosol optical thickness and the aerosol mass loading are monitored over most of the globe (oceans and the moist parts of the continents) on a daily basis. The size distribution of the ambient (undisturbed) aerosol will be derived only over the ocean. Over the land, the aerosol optical thickness will be derived using the dark target approach but limited to the moist parts of the continents excluding snow and ice cover. Dust will be monitored only over the oceans. Methods such as using contrast reduction, variation in the apparent brightness and IR spectral techniques for dust will be studied and implemented post launch. The retrieved aerosol information will be used to study aerosol climatology, the sources and sinks, the transport of specific aerosol types (e.g., sulfates and biomass burning aerosol) in aerosol forcing of climate, and for atmospheric correction of remotely sensed surface reflectance over the land.

2.2 Historical Perspective

Present and past satellite measurements are limited to reflectance measurements in one channel such as from geostationary satellites (e.g., GOES or METEOSAT) or two channels from polar orbiters (e.g., AVHRR/NOAA). The algorithms used for retrieving the aerosol components have to assume an aerosol model for deriving the total aerosol content. The aerosol model is taken from literature as the most representative one for the local conditions (Shettle and Fenn, 1979; D'Almeida et al., 1991). Such method has been successfully applied over water (Griggs, 1975, 1977; Mekler at al., 1977, Koepke and Quenzel, 1979) to produce an operational product from NOAA AVHRR measurements (Rao et al., 1989), and most of the remote sensing studies have been devoted to Saharan dust (Fraser, 1976; Carlson, 1979, Norton et al., 1980, Dulac et al., 1992). Note that a climatology of dust events is under investigation by Jankowiak and Tanré (1992) recently. On the other hand, over the land, there has been so far no real attempt to retrieve aerosol content on a global scale since the surface albedo is generally unknown and variable with wavelength. Over the dark dense vegetation, which has a very low reflectance in the blue and red regions, some algorithms have been developed (Kaufman and Sendra, 1988; Holben et al. 1992). By assuming an invariant surface reflectance, the algorithms have been used for multi-temporal studies (Fraser et al., 1984; Tanré et al., 1988; Kaufman et al., 1990; Holben et al., 1992). The blue channel on MODIS (not present on

the AVHRR) offers a possibility to extend the derivation of aerosol optical thickness over the land to additional surfaces, since surface reflectance is usually darker in the blue channel and the aerosol scattering is expected to be larger.

2.3 CHARACTERISTICS OF THE MODIS INSTRUMENT

The MODIS (MODerate Resolution Imaging Spectrometer) instrument is designed to fly on the EOS (Earth Orbiting System) AM and PM platforms, with a daily global coverage. It is dedicated to perform measurements in the solar to thermal infrared spectrum region from 0.415 to 14.235 µm (Salomonson et al., 1989). The characteristics of seven spectral bands which are potentially useful for the remote sensing of aerosols are reported in Table 1-a. The spectral domain of interest is covered by three of the four focal planes, the visible (VIS from 0.412 to 0.551 µm), the near infrared (NIR from 0.650 to 0.940 µm), and the short-wavelength/medium-wavelength infrared (SWIR/MWIR from 1.240 to 4.565 µm). The spectral stability is expected to be better than 2 nm and the instantaneous field of view varies between 250 and 500 m. The Noise Equivalent Differential Spectral Luminance (NeΔL in W/m^2/µm/sr) is also reported, as well as the Ne$\Delta\rho$ computed from

$$Ne\Delta\rho = Ne\Delta L \frac{\pi}{F_O \cos(\theta_S)} \qquad \text{(Eq.1)}$$

where F_0 is the extraterrestrial solar irradiance and $\theta_s = \cos^{-1}(\mu_s)$ is the solar zenith angle. In Table 1-a, Ne$\Delta\rho$ is given for an overhead sun ($\theta_s = 0°$).

Because the aerosol loading is usually expressed by the aerosol optical thickness instead of reflectance or radiance values, we computed the corresponding Ne$\Delta\tau$ using the single scattering approximation,

$$Ne\Delta\tau = Ne\Delta\rho \frac{4\mu_v\mu_s}{\omega_O P(\Theta)} \qquad \text{(Eq.2)}$$

$$= \frac{\pi Ne\Delta L}{F_O} \frac{4\mu_v}{\omega_O P(\Theta)}$$

where $\mu_v = \cos(\theta_v)$, θ_v is the viewing angle, and ω_o and $P(\Theta)$ the single scattering albedo and phase function. The Ne$\Delta\tau$ reported in Table 1-b is estimated in the most unfavorable conditions, i.e., in 2.13 µm channel where the aerosol optical thickness is expected to be minimum. Two cases are selected, pure maritime conditions and the presence of Saharan dust. Again, the most conservative conditions of a nadir observation ($\mu_v = 1$) and the lowest value of the phase function obtained for a scattering angle around 120° are selected. Following Shettle and Fenn (1979), a value of 0.05 is considered for the phase function of the dust-like model, while for maritime conditions the phase function is expected to be slightly larger, at around 0.08. The

results show the Noise Equivalent Differential Spectral Thickness of 2.4×10^{-2} for Saharan dust and 1.5×10^{-2} for maritime conditions (see Table-1-b). When the aerosol product is not given on a pixel by pixel basis (0.5×0.5 km²) but rather over a grid of 10×10 km² or 50×50 km², the noise is reduced by a factor of 20 and 100 respectively. From Hoppel et al. (1990), who reported that the Ångström parameters for a very clean air condition, the expected optical thickness, τ^{st}, in the 2.13 μm channel would be around 0.01 for maritime aerosols. For dust, however, a minimum value of 0.05 should be assumed (Tanré et al., 1988b). The signal to noise ratio SNR (defined by $Ne\Delta\tau/\tau^{st}$) as reported in Table 1-b, confirms that the optical characteristics cannot be retrieved for these conditions on a single pixel scale. The results obtained from coarser grids can be used with good confidence since the signal is at least 10 times larger than the noise.

Table 1-a. Characteristics of the MODIS channels used for the aerosols retrieval over Ocean; $Ne\Delta\rho$ corresponds to a sun at zenith ($\theta_S = 0°$).

Center Wavelength	$Ne\Delta L$	$Ne\Delta\rho$	Maximum Reflectance	SNR	Pixel Size at Nadir (m)
470	0.145	$2.35\ 10^{-4}$	0.96	243	500
550	0.127	$2.11\ 10^{-4}$	0.86	228	500
659	0.169	$3.39\ 10^{-4}$	1.38	128	250
865	0.123	$3.99\ 10^{-4}$	0.92	201	250
1240	0.045	$3.12\ 10^{-4}$	0.47	120	500
1640	0.027	$3.63\ 10^{-4}$	0.94	275	500
2130	0.009	$3.06\ 10^{-4}$	0.75	110	500

Table 1-b. Aerosol optical thickness sensitivity resulting only from the radiometric noise. Dust and maritime conditions are considered.

Grid Size (Km²)	$Ne\Delta\tau$ (Dust)	SNR	$Ne\Delta\tau$ (Maritime)	SNR
0.5x0.5	$2.4\ 10^{-2}$	2.0	$1.5\ 10^{-2}$	0.66
10x10	$1.2\ 10^{-3}$	42	$0.8\ 10^{-3}$	13
50x50	$2.4\ 10^{-4}$	208	$1.5\ 10^{-4}$	66

3. ALGORITHM DESCRIPTION - OCEAN

3.1 Strategy

Our strategy for the aerosol retrieval over the ocean is based on look-up table (LUT) approach, i.e., radiative transfer calculations are pre-computed in terms of the aerosol and surface parameters. The measured spectral radiance is then compared with pre-calculated values from LUT until the best (least-squares) fit is obtained. This best fit, or several of the best fits consists of the answer of the inversion. The input parameters, aerosols models and ocean surface conditions, required for performing the computations are hereafter described.

Aerosols models

Aerosols are formed by two main processes, a primary source which includes dispersion of material from the Earth's surface (like soil dust, sea salt particles, biomass burning, industrial debris), and a secondary source resulting from atmospheric chemical reactions or condensation or coagulation processes (see Mészráros (1981) and Hidy (1984) for more details). There are several classifications of atmospheric aerosols but the most commonly used one is according to their sizes. Whitby (1978) showed that an actual size distribution can be expressed by a sum of log-normal functions, each representing a different physical or chemical process. He suggests three modes (1) a *nuclei* mode which is generated by spontaneous nucleation of the gaseous material for particle less than 0.04 µm in diameter, (2) the *accumulation* mode for particles between 0.04 and 0.5 µm diameter, mainly resulting from coagulation and in cloud processes (Hoppel et al., 1990), and (3) the *coarse* mode for particles larger than 1.0 µm in diameter originated from the Earth's surface (land and ocean). The classification is quite similar to the Junge's designation (1963) who referred to as Aitken, large and giant particles.

To model the aerosol size distribution, a multi-mode log-normal function is assumed. Shown below is the single-mode log-normal distribution function, as an example

$$n(r) = \frac{dN(r)}{dr} = \frac{N}{(2\pi)^{1/2}\sigma 2.3r} \exp\left\{-\frac{(\log r - \log r_m)^2}{2\sigma^2}\right\} \qquad \text{(Eq.3)}$$

where N is the number density (cm^{-3}), r_m the mean radius (µm) and σ the standard deviation of log(r), i.e., $\sigma^2 = <(\log r - \log r_m)^2>$. After the correction for stratospheric aerosol, the tropospheric aerosol model can be described by a bi-modal log-normal distribution, i.e., a sum of accumulation and coarse modes , expressed as

$$n(r) = \frac{dN(r)}{dr} = \sum_{j=1}^{2} \frac{dN_j(r)}{dr} \qquad \text{(Eq.4)}$$

where

$$\frac{dN_j(r)}{dr} = \frac{N_j}{(2\pi)^{1/2}\sigma 2.3r}\exp\left\{-\frac{1}{2\sigma^2}\left(\frac{\ln r - \ln r_m}{\ln(10)}\right)^2\right\} \qquad \text{(Eq. 5)}$$

the nuclei mode is not considered since it is too small to be detected from the scattered light.

The parameters of the two modes (called hereafter small (Si) and large (Lj) modes), as reported in Tables 2-a and 2-b, are the median radius, standard deviation and refractive index. The small mode mergers the contribution of an accumulation mode that is dominated by gas phase processes with that by cloud phase processes. The large mode mergers maritime particles with dusts. The selected aerosol models are derived mainly from ground based sampling of the aerosol characteristics, and they may not fully represent the optical properties of the ambient aerosol integrated along the vertical column.

In order to avoid this difficulty, there is a need to measure the climatology and variability of the size distribution and scattering phase function of the ambient undisturbed aerosol for the entire vertical column. A network of sun/sky radiometers is being developed and implemented to perform such measurements (Holben et al., 1996). A set of these data collected have been used to test and modify the present aerosol models (Nakajima et al, 1983; Kaufman et al., 1994; Kaufman and Holben, 1996). Based upon the data, a prevailing bi-modal log-normal aerosol volume distributions is shown in the radius range 0.05-10 μm.

Table 2-a: Parameters of the size distribution for the small mode.

Aerosol Model	Median Radius r^s_m	Standard Deviation σ^s	Refractive Index
S_A	0.035	0.40	1.45-0 .0035i
S_B	0.07	0.40	1.45-0 .0035i
S_C	0.06	0.60	1.45-0 .0035i
S_D	0.08	0.60	1.40-0 .0035i
S_E	0.10	0.60	1.40-0 .0035i

Table 2-b: Parameters of the size distribution for the large mode.

Aerosol Model	Median Radius r^l_m	Standard Deviation σ^l	Refractive Index
L_A	0.40	0.60	1.40-0 .0035i
L_B	0.60	0.60	1.40-0 .0035i
L_C	0.80	0.60	1.45-0 .0035i

L_D	0.40	0.60	1.45-0 .0035i
L_E	0.50	0.80	1.50-0 .0035i
L_F	1.00	0.80	1.50-0 .0035i

The Physical Processes

The satellite signal is composed by two contributions, atmospheric radiative transfer processes and surface reflection. The radiative transfer code from Ahmad and Fraser (1982) is used in generating look-up tables. It accounts for multiple scattering in the atmosphere by molecules and aerosol particles, and angular reflection by the surface of sun light, including polarization. The surface contribution over the ocean includes the specular reflection on the waves (called glitter) and the underwater Lambertian reflectance which forms the 'ocean color' and reflection by foam.

The specular reflection on the sea surface is calculated using a rough ocean model from Cox and Munk (1955). The probability distribution of surface slopes is assumed to be independent of the azimuth, and the reflection of the light by waves is given by the classical fresnel equation. As the glitter reflectance is several orders of magnitude larger than the aerosol contribution, it will be avoided by selecting pixels outside the specular direction (i.e., ±30° around the solar zenith angle and ± 30° around the solar azimuth angle). An effort is undergone to better define the glint mask. In addition to the direct glint, for even far from the specular direction, the surface glint can reflect the diffuse sky light to the satellite sensor, which should also be taken into account.

The percentage of the sea covered by foam depends on the wind speed (Koepke, 1984). The reflectance of the foam is independent of wavelength in the visible and decreases by a factor of 0.8, 0.5 and 0.25 at 1240, 1640 and 2130 nm, respectively (Whitlock et al., 1982). Recent measurements (Frouin et al., 1996) show that this spectral dependence is questionable (even at 865 nm) and may result in additional uncertainties. In the radiative transfer code we used, the foam reflectance is assumed to be isotropic (Payne, 1972).

The water-leaving radiance depends on turbidity and the pigment concentrations. From Morel and Prieur (1977), waters with high chlorophyll contents (referred to as case 1) show large variation in the reflectance relative to the pigment concentrations at 470 nm band, and at 555 nm it is also affected but to a smaller extent. Case 1 represents the open ocean conditions. In other spectral bands, the reflectances are almost unaffected. At the band of 659 nm, it can be affected by chlorophyll *a* fluorescence but the resulting error is almost negligible (Gordon, 1979). On the other hand, waters with higher concentrations of inorganic particles as opposed to phytoplankton (case 2) show large variation in 470, 550 and 659 nm channels. The resulting uncertainty in the reflectance is large but these conditions are usually representative of coastal zones only.

Description of the Look-Up Table (LUT)

The look-up tables to calculate the radiance of MODIS spectral bands are used in retrieving aerosol parameters of each mode - the small particle mode (5 cases) for the accumulation mode particles, and the large particle mode (6 cases) for the coarse particles.

Several values of aerosol total loading are considered for each mode and described by the optical thickness τ_a at 0.55 μm. Extreme conditions are included in the LUT, such as a pure molecular atmosphere ($\tau_a = 0.0$) and a very turbid atmosphere ($\tau_a = 2.0$) as observed during dust events (Tanré et al., 1988b) or in smoke plumes generated from biomass burning (Holben et al., 1991). Three intermediate values were considered ($\tau_a = 0.2, 0.5, 1.0$), and a linear interpolation between them is applied. Computations are performed for 15 zenith view angles ($\theta_v = 1.5°$ to 88 by step of 6°), 15 azimuth angles ($\phi_v = 0°$ to 180° by step of 12°), and seven sun incident angles (qs = 1.5°, 12°, 24°, 36°, 48°, 54°, 60°, 66°, and 72°). We tested the accuracy of this look-up table and found that the errors outside glint region are less than 2%.

The present computations are performed for wind speed of 7.0 m/s and zero water leaving radiances in all the channels. We are in the process to build additional LUT for other wind speeds and for different chlorophyll concentrations. The most appropriate LUT will be selected for the wind speed from assimilated data (Schubert et al., 1993; Data Assimilation Office (DAO) of Laboratory for Atmosphere at Goddard Space Flight Center (GSFC)) and from the chlorophyll content derived from other MODIS channels (Gordon, 1996).

3.2 Description of the Algorithm

Our approach to generate the LUT and to use them in the retrieval is based on the simplification suggested by Wang and Gordon (1994) that the multiple scattering radiance from two log-normal modes can be approximated by the weighted average of the radiances of each individual mode for the same optical thickness. While difficulties may be encountered when the two modes have different absorbing properties, this concept is quite suitable in our conditions. The advantage of this simplification is that the look-up tables are only needed for 11 aerosol models (5 small and 6 large) instead of all 5x6x10 combinations (10 is the number of relative concentrations between the modes). The inputs of the algorithm are the averaged cloud-free MODIS measurements in seven MODIS solar bands over a box of 10x10 km^2 (or 50x50km^2). The cloud screening and the data processing for handling the possible non-uniformity of the aerosol layer (different types and contents) within the box are not discussed here.

Principle

If the total radiance L^c_λ detected by the satellite can be written as

$$L^c_\lambda(\mu_s, \mu_v, \phi_v) = \eta \, L^s_\lambda(\mu_s, \mu_v, \phi_v) + (1-\eta) \, L^l_\lambda(\mu_s, \mu_v, \phi_v) \qquad \text{(Eq.6)}$$

where $L^s_\lambda(\mu_s, \mu_v, \phi_v)$ and $L^l_\lambda(\mu_s, \mu_v, \phi_v)$ are the radiances of the small (S_i) and large (L_j) modes respectively. The goal is to retrieve the ratio η and the particle sizes of the small and large modes which give the best fit to the measurements. The aerosol optical thickness at 550 nm is derived as a by-product.

The selection of the aerosol models is performed by minimizing the following quantity ε_{sl}

$$\varepsilon_{sl} = \sqrt{\frac{1}{n} \sum_{j=1}^{n} \left(\frac{L^{m_j}(\mu_s, \mu_v, \phi_v) - L^{c_j}(\mu_s, \mu_v, \phi_v)}{L^{m_j}(\mu_s, \mu_v, \phi_v) + 0.01} \right)^2} \qquad \text{(Eq.7)}$$

where $L^{m_j}(\mu_s, \mu_v, \phi_v)$ and $L^{c_j}(\mu_s, \mu_v, \phi_v)$ are the measured and the computed radiances of channel j. The radiances are normalized to reflectance units. We add a constant value of 0.01 to reduce the weighting of longer wavelengths in SWIR region in the retrieval. For clear-sky conditions, with strong spectral variation, $L^m_{2130}(\mu_s, \mu_v, \phi_v)$ is close to 0.0 with high uncertainty in the relative value. The constant of 0.01 in Eq. 7 minimizes the impact due to this uncertainty in the retrieval. MODIS has seven potentially useful bands for remote sensing of aerosol over the ocean. But in the shortest channel (470 nm), the surface contribution is very uncertain and provides no additional information on the ocean color. As it may result in errors in the aerosol contribution which we may not understand completely, it is therefore ignored in the retrieval algorithm and the summation in Eq. 7 is performed over 6 channels only, from 555 nm to 2130 nm.

Method

For the 5 small particle modes and the 6 large modes, the radiances $L^s_\lambda(\mu_s, \mu_v, \phi_v)$ and $L^l_\lambda(\mu_s, \mu_v, \phi_v)$ are computed using the LUT for 5 different values of the aerosol optical thickness τ_a at 550 nm (0.0, 0.2, 0.5, 1.0 and 2.0) given the geometrical condition of the observation. As already mentioned, the surface conditions in the LUT, such as wind speed and chlorophyll content, are selected from ancillary data. For a combination of small (S_i) and large (L_j) modes of any value of η, we can compute the total radiance $L^c_{550}(\mu_s, \mu_v, \phi_v)$ using Eq. 6, for the five optical thicknesses. From the measured radiance at 550 nm, the optical thickness is derived by linear interpolation between these five optical thickness values of each small and large mode combinations. The two modes that give the smallest residual error $\varepsilon_{sl}(\eta)$, for the best selected value of η, is the selected aerosol model. In this retrieval process, for each small and large mode combination and each value of η, the optical thicknesses in all seven channels are derived and the satellite radiances are used to compute the

quantity ε_{sl} in Eq. 7. The algorithm provides the aerosol model and associated parameters, which corresponds to the minimum value of ε_{sl} (called the "best" solution) as well as the parameters averaged over the models to give $\varepsilon_{sl} <3\%$ (called the "average" solution) of which the standard deviation of the reflectances is also computed.

By-products

Simultaneously, in addition to the derivation of the ratio between the modes, η, the characteristics of the two modes, the optical thickness, τ_a, and the associated parameters are also computed using the LUT, partly corresponding to the quantities that govern the radiative transfer and the aerosol direct forcing (such as single scattering albedo, asymmetry factor and backscattering ratio) and partly to physical properties like the number of particles, the number of cloud condensation nuclei (CCN) or the moments of the size distribution. The aerosol effective radius should be determined accurately, even if the actual size distribution does not follow a simple log-normal law (Hansen and Hovenier, 1974). Other physical parameters like CCN number depend strongly on the exact shape of the size distribution, which are not reliable at this stage. We do, however, compute all output parameters, including the CCN, and these are available in the hdf output file, but should only be used as a research tool. Further studies will show that for which aerosol types and for what conditions these additional parameters are representative. The definition of the parameters are recalled in the appendix.

3.3 Sensitivity Study

We have tested the algorithm twice. The first time was using values from the LUT computed from a preliminary choice of model parameters. The second time was using values listed in Table 2. The old and new model values span the same conditions. In the following section we report the results of the first sensitivity test using the preliminary LUT. The results of the second test are in good agreement to the first, and are not shown in this document.

We have tested the algorithm by applying it (1) to the conditions which are identical to those as tabulated in the LUT, and (2) to the conditions that at least one of the parameters (e.g., optical thickness, wind speed and refractive index) is not the same as tabulated in the LUT. In addition, we have performed simulations for considering the following issues such as sensor calibration, contamination by glint, wrong estimate of the water-leaving radiance. Results of the sensitivity study are provided for the following retrieved parameters

- the median radius and its standard deviation of each mode
- the optical thickness τ_a at 550 nm
- the ratio η between the contributions to the radiance of the two modes
- the effective radius of the complete size distribution r_{eff}
- and the asymmetry parameter g at 550 nm

Input data sets

Table 3-a describes the cases of sensitivity study for which the inputs are identical to those in the LUT (i.e., cases 0 to 11). In the cases of single mode, two small modes S_A and S_B (see Table 4-a) and one large mode L_A (see Table 4-b) are considered with aerosol optical thicknesses equal to 0.2, 0.5, 1.0 and 2.0. For the two modes

combined, S_A and L_A, with η =0.41, only two aerosol optical thicknesses of 0.2 and 0.5 are used.

In Table 3-b (cases 12 to 18), we check the results for the aerosol optical thickness values which are not included in the LUT, i.e., τ_a=0.35 and 0.85. The cases involve single mode of small mode S_B (cases 12 and 13) and large mode L_B (cases 14 and 15), and double modes of S_B and L_B (cases 16 to 19) with η=0.15 and 0.70. The effect of wind speed is also checked for simulations of a wind speed equal to 5.0 m/s (instead of 7.0 m/s) for aerosols models including S_A (case 19) and L_A (case 20), single mode, and S_A and L_a (double mode) with η=0.41 (case 21). The smallest value of the optical thickness (τ_a=0.20) has been selected since the impact is expected to be maximum in these conditions. The effect of the refractive index is tested by simulations of a refractive index of 1.5 with retrieval on 1.45 for single modes of S_A and L_D, and double mode of S_A and L_D with η=0.15 and 0.70 (cases 22 to 25). Again the smallest value of the aerosol optical thickness has been selected in the simulation since the multiple scattering, which occurs for large τ_a, is expected to smooth the effect of the actual phase function.

Table 3-a. Optical properties and effective radius of the input data sets included in the look-up table. The optical properties are given at 550 nm.

Case N°	Small Mode	r^s_{eff}	Large Mode	r^l_{eff}	r_{eff}	Ratio η	Opt. Thick. τ	Asy. Factor g
0	/	/	/	/	/	/	0.000	/
1	S_A	0.049	/	/	0.049	1.00	0.200	0.367
2	S_A	0.049	/	/	0.049	1.00	0.500	0.367
3	S_A	0.049	/	/	0.049	1.00	1.000	0.367
4	S_A	0.049	/	/	0.049	1.00	2.000	0.367
5	S_B	0.098	/	/	0.098	1.00	0.500	0.588
6	/	/	L_A	0.984	0.984	0.00	0.200	0.764
7	/	/	L_A	0.984	0.984	0.00	0.500	0.764
8	/	/	L_A	0.984	0.984	0.00	1.000	0.764
9	/	/	L_A	0.984	0.984	0.00	2.000	0.764
10	S_A	0.049	L_A	0.984	0.077	0.41	0.200	0.573
11	S_A	0.049	L_A	0.984	0.077	0.41	0.500	0.573

Table 3-b. Optical properties and effective radius of the input data sets which are not included in the look-up table. The optical properties are given at 550 nm.

Case N°	Small Mode	r^s_{eff}	Large Mode	r^l_{eff}	r_{eff}	Ratio η	Opt. Thick τ.	Asym. Factor g	Additional Variable
12	S_B	0.098	/	/	0.098	1.00	0.350	0.588	$\tau_a \neq$
13	S_B	0.098	/	/	0.098	1.00	0.850	0.588	$\tau_a \neq$

14	/	/	L_B	0.890	0.890	0.00	0.350	0.744	$\tau_a \neq$
15	/	/	L_B	0.890	0.890	0.00	0.850	0.744	$\tau_a \neq$
16	S_B	0.098	L_B	0.890	0.380	0.15	0.350	0.706	$\tau_a \neq$
17	S_B	0.098	L_B	0.890	0.380	0.15	0.850	0.706	$\tau_a \neq$
18	S_B	0.098	L_B	0.890	0.130	0.70	0.850	0.620	$\tau_a \neq$
19	S_A	0.049	/	/	0.049	1.00	0.200	0.367	$v=5m.s^{-1}$
20	/	/	L_A	0.984	0.984	0.00	0.200	0.764	$v=5m.s^{-1}$
21	S_A	0.049	L_A	0.984	0.077	0.41	0.200	0.572	$v=5m.s^{-1}$
22	S_A	0.049	/	/	0.049	1.00	0.200	0.367	$m=1.50$
23	/	/	L_D	2.970	2.970	0.00	0.200	0.805	$m=1.50$
24	S_A	0.049	L_D	2.970	0.395	0.15	0.200	0.711	$m=1.50$
25	S_A	0.049	L_D	2.970	0.086	0.70	0.200	0.481	$m=1.50$

Table 4-a. Optical properties and effective radius of the size distribution for the small mode. The optical properties are given at 550nm.

Aerosol Model	Effective Radius	Single Scat. Albedo	Asymmetry Factor	Backscattering Ratio
S_A	0.05	0.932	0.367	0.360
S_B	0.10	0.969	0.588	0.270
S_C	0.06	0.920	0.269	0.398
S_D	0.20	0.976	0.720	0.210
S_E	0.12	0.967	0.567	0.280

Table 4-b. Optical properties and effective radius of the size distribution for the large mode. The optical properties are given at 550 nm.

Aerosol Model	Effective Radius	Single Scat. Albedo	Asymmetry Factor	Backscattering Ratio
L_A	0.98	0.938	0.764	0.172
L_B	0.89	0.939	0.744	0.181
L_C	1.48	0.905	0.763	0.167
L_D	2.97	0.856	0.805	0.142
L_E	2.46	0.857	0.799	0.144
L_F	4.95	0.810	0.828	0.125

Results (with no additional errors)

We first assume the perfectly measured radiances, i.e., no calibration error and no uncertainty in the surface reflectance estimated, except for the error of wind speed.

The retrieved median radius and the standard deviation of the cases are reported in Tables 5-a and 5-b for the 'best' solutions and in Tables 6-a and 6-b for the 'average' solutions. To illustrate the results of the four quantities τ_a, η, r_{eff} and g, we adopt a scatter diagram plot of the retrieved values versus the input values (see Fig. 1). In the first quarter (denoted as (a)), the results are obtained with inputs that are identical to those as tabulated in the LUT; in the second quarter (b), we consider cases with optical thickness values which are not included in the LUT; in the third quarter (c), the impact of the wind speed is considered; and finally in the fourth quarter (d), we assess the effect of the refractive index. The black dots correspond to the 'best' solutions and the crosses to the 'average' solutions. The standard deviation is also given for the 'average' solution.
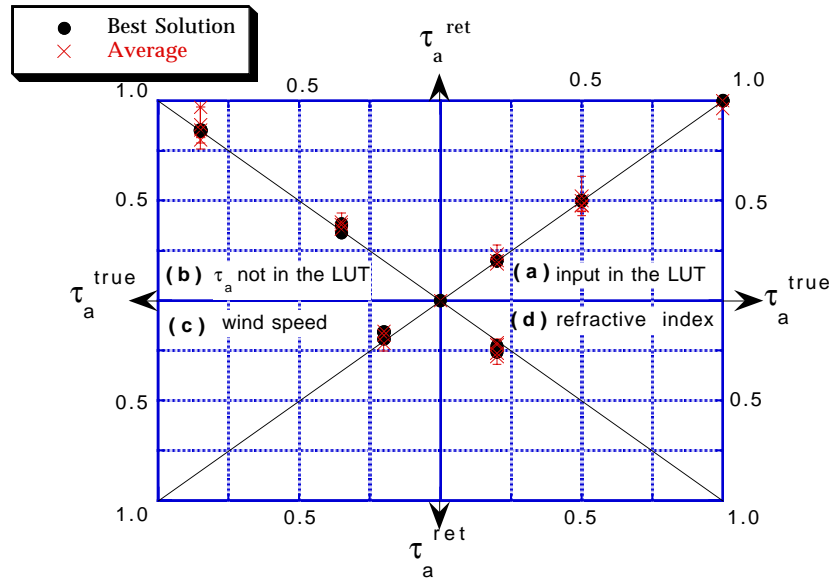
Figure 1. Scatter diagram of the optical thickness, the x-axis correspond to the input, the y-axis to the retrieved values. Each quarter is devoted to a specific sensitivity study. Quarter (a) corresponds to an inversion where all the input are included in the LUT. Quarter (b) corresponds to an inversion with values of the optical thickness not included in the LUT. Quarter (c) corresponds to a different wind speed. Quarter (d) corresponds to a different refractive index. The black dots correspond to the 'best' solutions and the crosses to the 'average' solutions (see the text).

• Median Radius and standard deviation

From Table 5-a, it is obvious that the 'best' solutions give perfect results when the inputs are the same as those included in the LUT. From Table 5-b, for those inputs which are not the same as included in the LUT, we basically retrieve the right values except for the following cases:

(a) model S_E instead of model S_B (cases 12 and 16)
(b) model S_C instead of model S_A (cases 19, 21 and 24)
(c) model L_B instead of model L_A (case 21)

Referring back to Tables 4-a and 4-b, it is clear that the alternative solutions correspond closely to the aerosols models which have the similar radiative properties to those in the inputs. For example, the small modes of S_E and S_C have very similar effective radius to S_B and S_A respectively, as well as the large mode of L_B compared to L_A. As shown in Tanré et al. (1996), we are often in conditions where the inverted effective radius shows large discrepancy as compared to the true value while the value of σ has nearly no impact. There are also conditions where single narrow size distributions can be retrieved (Kaufman et al., 1990), for instance, for smoke observed with scattering angles around 100°, where we were able to distinguish between narrow and broad size distributions.

In Tables 6-a and 6-b, the 'average' solutions are reported. The standard deviation computed for the median radius is usually small when only single mode is considered, but it becomes larger for the small and large combined modes cases, mainly due to the retrieval of the small mode r^s_m. As a general rule, the large mode can be retrieved within the error bars, but larger discrepancies may occur to the small mode.

Table 5-a. Input and retrieved characteristics of the aerosols models for the 'best' retrieval when all the parameters are included in the LUT.

Case N°	Input values				Retrieved values			
	Median Rad. r^s_m	Stand. Dev. σ^s	Median Rad. r^l_m	Stand. Dev. σ^l	Median Rad. r^s_m	Stand. Dev. σ^s	Median Rad. r^l_m	Stand. Dev. σ^l
1	0.02	0.60	/	/	0.02	0.60	/	/
2	0.02	0.60	/	/	0.02	0.60	/	/
3	0.02	0.60	/	/	0.02	0.60	/	/
4	0.02	0.60	/	/	0.02	0.60	/	/
5	0.04	0.60	/	/	0.04	0.60	/	/
6	/	/	0.40	0.60	/	/	0.40	0.60
7	/	/	0.40	0.60	/	/	0.40	0.60
8	/	/	0.40	0.60	/	/	0.40	0.60
9	/	/	0.40	0.60	/	/	0.40	0.60
10	0.02	0.60	0.40	0.60	0.02	0.60	0.40	0.60
11	0.02	0.60	0.40	0.60	0.02	0.60	0.40	0.60

Table 5-b. Input and retrieved characteristics of the aerosols models for the 'best' retrieval when some parameters are not included in the LUT.

Case N°	Input values				Retrieved values			
	Median Rad. r^s_m	Stand. Dev. σ^s	Median Rad. r^l_m	Stand. Dev. σ^l	Median Rad. r^s_m	Stand. Dev. σ^s	Median Rad. r^l_m	Stand. Dev. σ^l
12	0.04	0.60	/	/	0.08	0.40	/	/
13	0.04	0.60	/	/	0.04	0.60	/	/
14	/	/	0.60	0.40	/	/	0.60	0.40
15	/	/	0.60	0.40	/	/	0.60	0.40
16	0.04	0.60	0.60	0.40	0.08	0.40	0.60	0.40
17	0.04	0.60	0.60	0.40	0.04	0.60	0.60	0.40
18	0.04	0.60	0.60	0.40	0.04	0.60	0.40	0.60
19	0.02	0.60	/	/	0.04	0.40		
20	/	/	0.40	0.60	/	/	0.40	0.60
21	0.02	0.60	0.40	0.60	0.04	0.40	0.60	0.40
22	0.02	0.60	/	/	0.02	0.60	/	/
23	/	/	0.60	0.80	/	/	0.60	0.80
24	0.02	0.60	0.60	0.80	0.04	0.40	0.60	0.80
25	0.02	0.60	0.60	0.80	0.02	0.60	0.60	0.80

Table 6-a. Input and retrieved characteristics of the aerosols models for the 'average' retrieval when all the parameters are included in the LUT.

Case N°	Input Values				Retrieved values			
	Median Rad. r^s_m	Stand. Dev. σ^s	Median Rad. r^l_m	Stand. Dev. σ^l	Median Rad. r^s_m	Stand. Dev. σ^s	Median Rad. r^l_m	Stand. Dev. σ^l
1	0.02	0.60	/	/	0.03±0.01	0.47±0.10	/	/
2	0.02	0.60	/	/	0.03±0.01	0.52±0.10	/	/
3	0.02	0.60	/	/	0.03±0.01	0.52±0.10	/	/
4	0.02	0.60	/	/	0.03±0.01	0.52±0.10	/	/
5	0.04	0.60	/	/	0.06±0.02	0.50±0.10	/	/
6	/	/	0.40	0.60	/	/	0.40±0.02	0.60±0.11
7	/	/	0.40	0.60	/	/	0.40±0.02	0.60±0.11
8	/	/	0.40	0.60	/	/	0.40±0.02	0.60±0.11
9	/	/	0.40	0.60	/	/	0.40±0.02	0.60±0.11
10	0.02	0.60	0.40	0.60	0.06±0.02	0.51±0.10	0.67±0.23	0.62±0.14
11	0.02	0.60	0.40	0.60	0.05±0.02	0.47±0.10	0.58±0.19	0.60±0.14

Table 6-b. Input and retrieved characteristics of the aerosols models for the 'average' retrieval when some parameters are not included in the LUT.

Case N°	Input Values				Retrieved values			
	Median Rad. r^s_m	Stand. Dev. σ^s	Median Rad. r^l_m	Stand. Dev. σ^l	Median Rad. r^s_m	Stand. Dev. σ^s	Median Rad. r^l_m	Stand. Dev. σ^l
12	0.04	0.60	/	/	0.06±0.02	0.50±0.10	/	/
13	0.04	0.60	/	/	0.06±0.02	0.50±0.10	/	/
14	/	/	0.60	0.40	/	/	0.60±0.00	0.40±0.00
15	/	/	0.60	0.40	/	/	0.60±0.00	0.40±0.00
16	0.04	0.60	0.60	0.40	0.05±0.03	0.51±0.11	0.57±0.08	0.43±0.08
17	0.04	0.60	0.60	0.40	0.05±0.03	0.51±0.11	0.57±0.08	0.43±0.08
18	0.04	0.60	0.60	0.40	0.07±0.02	0.53±0.10	0.64±0.22	0.60±0.14
19	0.02	0.60	/	/	0.04±0.00	0.40±0.00		
20	/	/	0.40	0.60	/	/	0.50±0.10	0.50±0.10
21	0.02	0.60	0.40	0.60	0.06±0.02	0.51±0.10	0.67±0.23	0.62±0.14
22	0.02	0.60	/	/	0.03±0.01	0.49±0.10	/	/
23	/	/	0.60	0.80	/	/	0.70±0.19	0.75±0.09
24	0.02	0.60	0.60	0.80	0.06±0.02	0.51±0.10	0.78±0.21	0.75±0.09
25	0.02	0.60	0.60	0.80	0.03±0.01	0.50±0.11	0.70±0.19	0.70±0.11

• Optical thickness τ_a.

Note in Figure 1 that a very good agreement is obtained for the 'best' solutions (black dots). The average solutions (crosses), on the other hand, lead to slightly different values but in general the optical thicknesses are retrieved with good accuracy, even when uncertainties in the refractive index and wind speed are introduced. Cases for τ_a=2.0 are perfectly retrieved but are not reported on the plot, in order to keep a high resolution of the display results.

• Ratio η.

Similar conclusions can also be made for the ratio η, the contribution to the radiance of the small mode, when only the 'best' solutions (black dots) are considered (see Fig. 2). Large variations are observed in the 'average' solutions (crosses) for double modes, i.e., when $\eta \neq 0.0$ and 1.0. Because of the lack of uniqueness in the relationship between physical and optical properties (Tanré et al., 1996), large fluctuations in the retrieved physical properties may occur, (as already noticed in Tables 6-a and 6-b), and as a result the algorithm has to compensate them by selecting a wrong ratio η. It is interesting to note that the standard deviation (shown as error bars) is a good measure of the quality of the retrieval; when it is small, the 'average' and 'best' solution are similar and quite close to the true values.
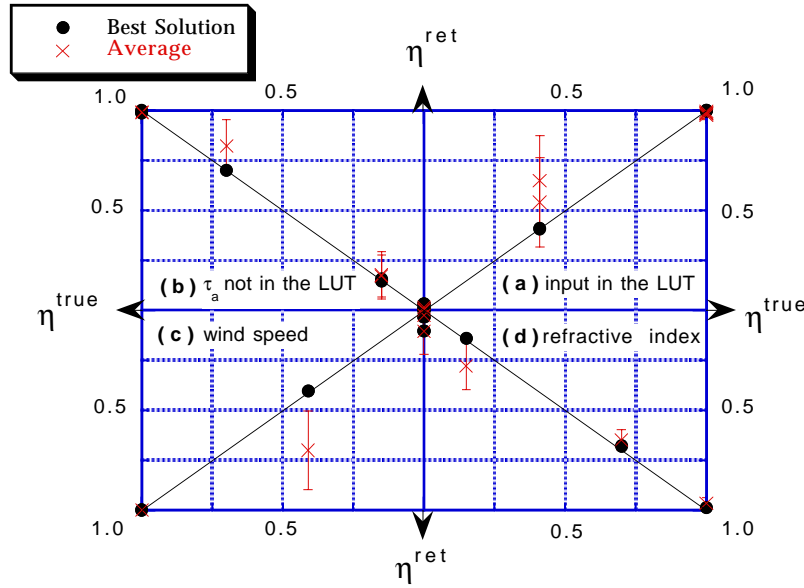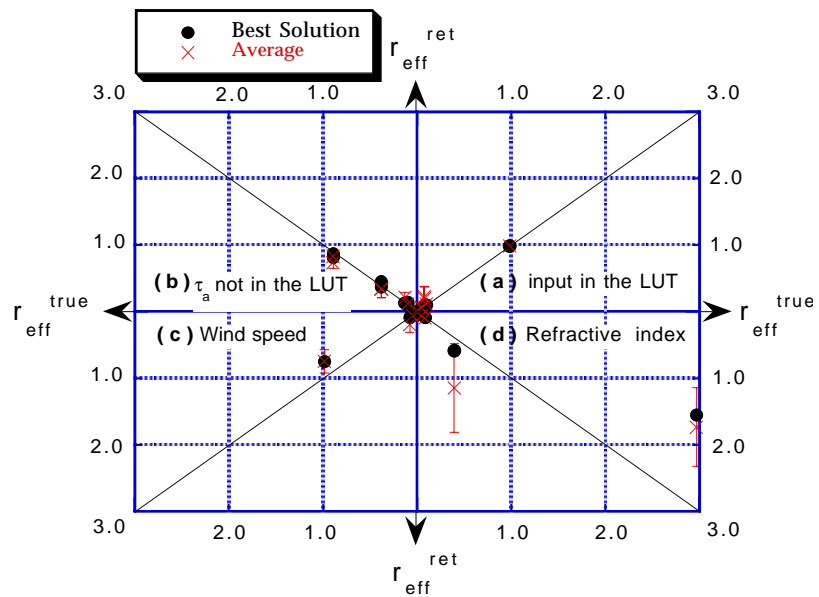
Figure 2. Same as in Fig. 1 but for the ratio η. Error bars correspond to the standard deviation of the 'average' solution.

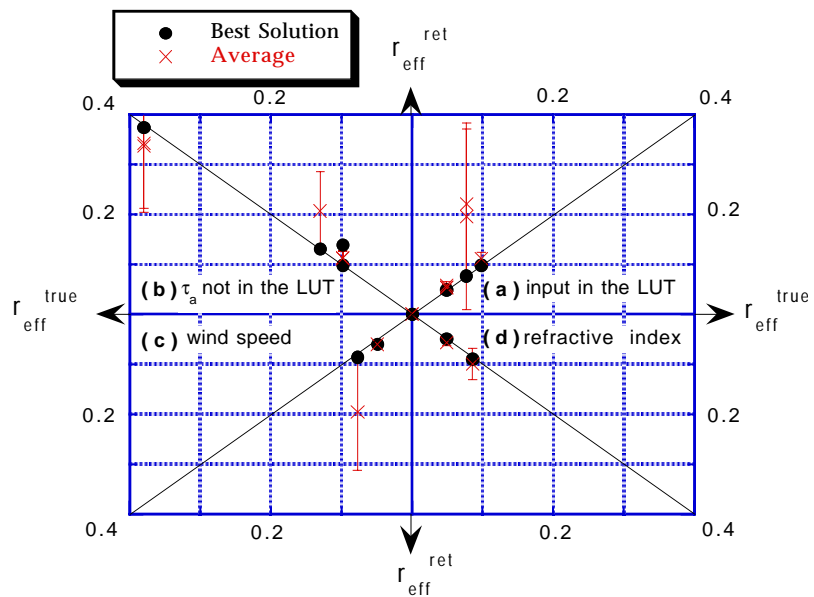• Effective radius r_{eff}

The results of the effective radius r_{eff} are reported in Figs. 3-a and b. Because of the plotting scale, Fig. 3-b shows an enhancement of Fig. 3-a, corresponding roughly to the accumulation mode with r_{eff} smaller than 0.40 μm. For the accumulation mode, (see Fig. 3-b), the 'best' effective radiuses (black dots) are well retrieved for single or double mode, while the 'average' solutions (crosses) can be far different from the true value, especially for double mode cases. Again the standard deviation is a good indicator of the quality of the retrievals. For larger particles (see Fig. 3-a), the retrieval is very well performed for (a) and (b) conditions, and to a less extent for (c). In (d), large errors result for both 'best' and 'average' solutions if uncertainty in the refractive index is considered. It is because the sensitivity of the spectral dependence is very weak for large particles and small uncertainty in the aerosol properties could have significant impact. Although the exact characteristics of the coarse mode are difficult to assess, it is important to notice that the algorithm is able to detect the presence of such large particles.

Figure 3-a. Same as in Fig. 1 but for the effective radius. Error bars correspond to the standard deviation of the 'average' solution.

Figure 3-b. Same as in Fig. 3-a but for effective radius smaller than 0.40μm.

• <u>Asymmetry parameter g</u>

The asymmetry parameter is again well related to the radiative properties. Therefore the algorithm is very efficient to retrieve it. From Fig. 4, over the large range of simulated values from 0.367 to 0.805, the 'best' and 'average' solutions return almost perfect results. Small discrepancies occur only for different wind speed conditions and when particles are small, as already noted in Tables 5-a and b. The uncertainty in the surface conditions leads to choose the closest model with slightly different radiative properties. The standard deviations are found to be small in all the cases, which confirms that the problem is very well-conditioned for this parameter.
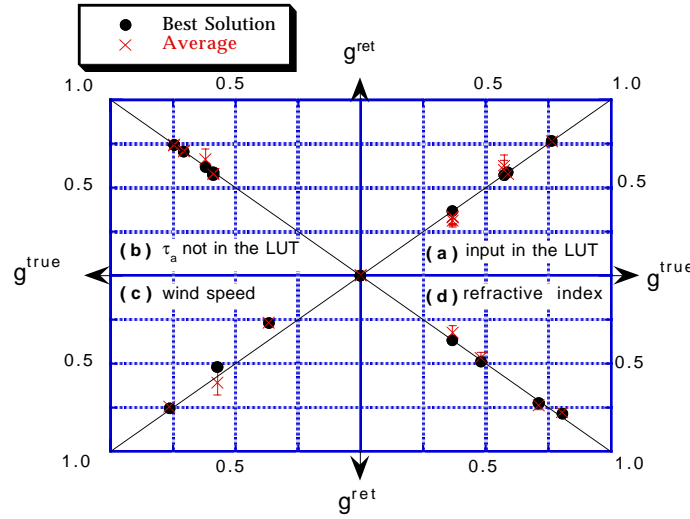
<u>Figure 4.</u> Same as in Fig. 1 but for the asymmetry factor g. Error bars corresponds to the standard deviation of the 'average' solution.

Results due to potential sources of error

In this section, we discuss additional potential issues like the sensor calibration, the contamination by glint or false estimate of the water-leaving radiance. To simulate these effects, we added the error separately to the measurements L^m_j for each channel (j) in the following way.

(a) calibration error

$L^m_j => L^m_j(1.-Rnd_j)$ where Rnd_j is random error scaled between ±0.01. It represents a random spectral calibration error of maximum of 1%.

(b) Glint error

$L^m_j => L^m_j + 0.01$, this considers that the glint effect may not be completely avoided or predicted, which adds a constant value to the reflectance in all channels.

(c) Type 1 surface error

$L^m_j => L^m_j + Rnd_j$, where Rnd_j is random error ranged between ±0.002. It represents, for instance, possible errors in the water leaving radiance.

(d) Type 2 surface error

$L^m_j = L^m_j + 0.005/\lambda_j$, where λ_j is the center wavelength (in μm) of channel j.

For doing so, the reflectance is increased by approximately 0.01 in 0.55 μm and 0.0025 in 2.13 μm channels, representing systematic errors in the spectral dependence of the reflectances, like uncertainties resulting from the foam spectral dependence.

In Figs. 5 to 8, (a), (b), (c), and (d) quarters represent accordingly the errors shown above. Note that the results are given for all cases (1 to 25).

• Optical thickness τ_a

For randomly distributed errors as shown in quarters (a) and (c) in Fig. 5 of calibration and type 1 surface errors, there is no systematic effect and the impact is almost negligible in most of the cases. Surface errors due to the glint or Type 2 surface errors (i.e., non-random errors) lead to an overestimate of the optical thickness. That's because additional surface contribution is translated into a larger atmospheric contribution, and in consequence results in a larger optical thickness. This effect is more important for small optical thickness, as expected.
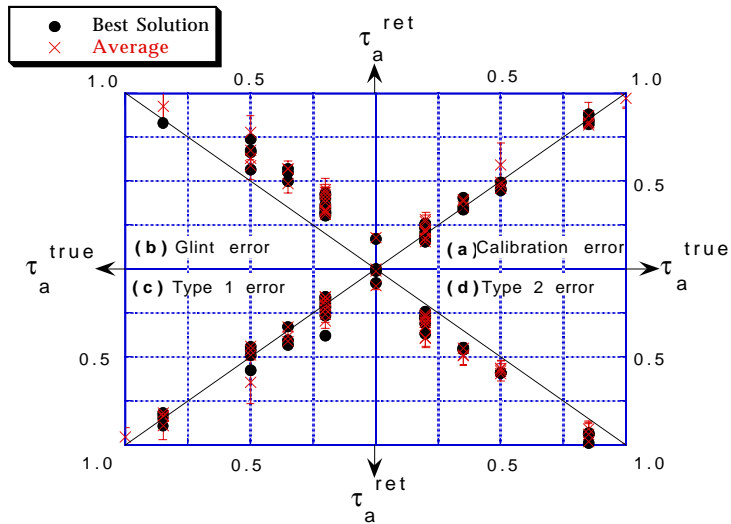
Figure 5. Scatter diagram of the optical thickness, the x-axis correspond to the input, the y-axis to the retrieved values. Each quarter is devoted to a specific source of errors. Quarter (a) corresponds to calibration errors. Quarter (b) corresponds to glint error. Quarter (c) corresponds to Type 1 surface error. Quarter (d) corresponds to Type 2 surface error. The black dots correspond to the 'best' model and the crosses to the 'average' solution (see the text). Errors bars correspond to the standard deviation of the 'average' solution.

• Ratio η

Figure 6 clearly shows that it is difficult to retrieve this parameter accurately in the presence of these errors. The dispersion is quite large for both 'best' and 'average' solutions, thus the retrieved values will have to be considered as an estimate. Let us note that the glint effect is the most destructive error; it may result in 100% error but there is no systematic bias. Better values of the ratio η can be retrieved far from the specular reflection. A solution that will be considered is to generate aerosol climatology from the MODIS data.
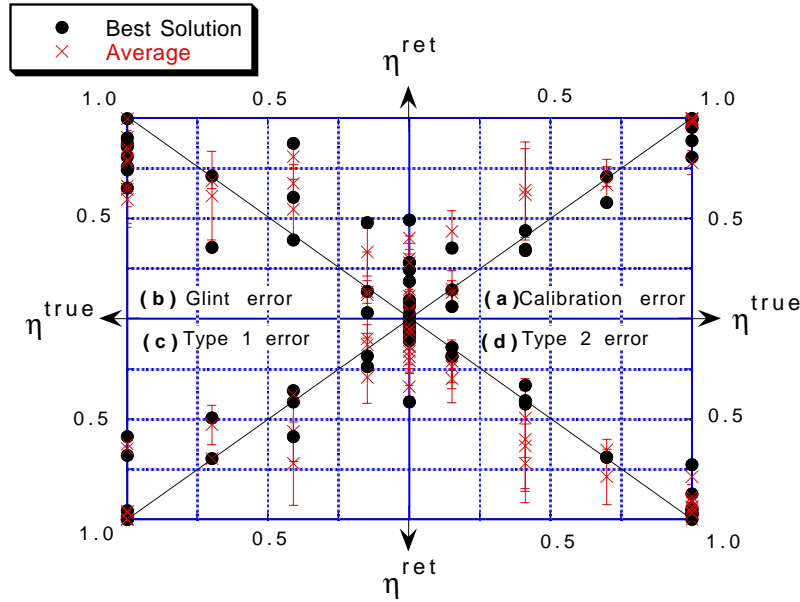
Figure 6. Same as in Fig. 5 but for the ratio η.

• Effective radius r_{eff}

For effective radiuses smaller that 0.2 μm, glint error can result in a significant impact to both 'best' and 'average' solutions (see Fig.7-b). Figure 7-b is again an enlargement of Fig. 7-a for better illustration of the results. For other types of errors, the best solutions (black dots) give the right answer while the average solutions (crosses) show large variability. In Fig. 7-a, for large effective radiuses, all the sources of errors cause an underestimate of the aerosol sizes. As mentioned earlier, the sensitivity to large particles is weak and there exists a threshold value of effective radius around 1.0 μm from which the retrieval is questionable.
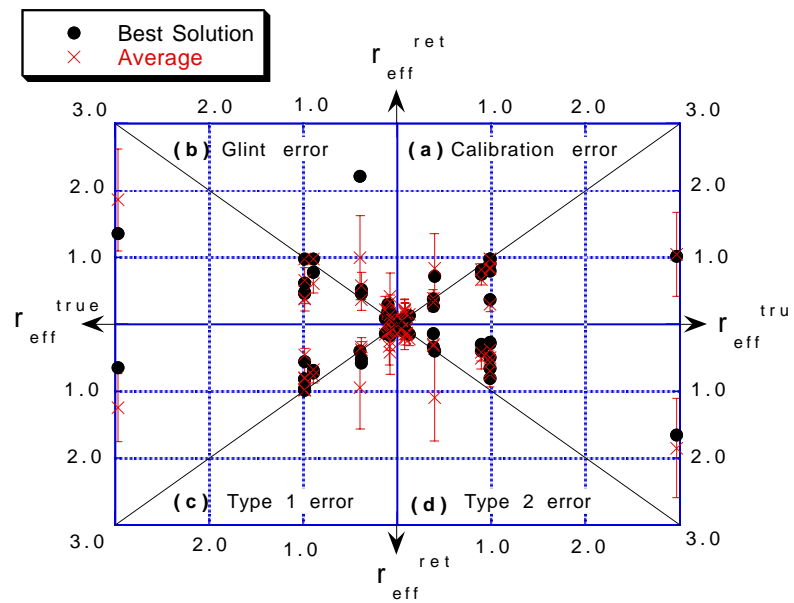
Figure 7-a. Same as in Fig. 5 but for the effective radius.
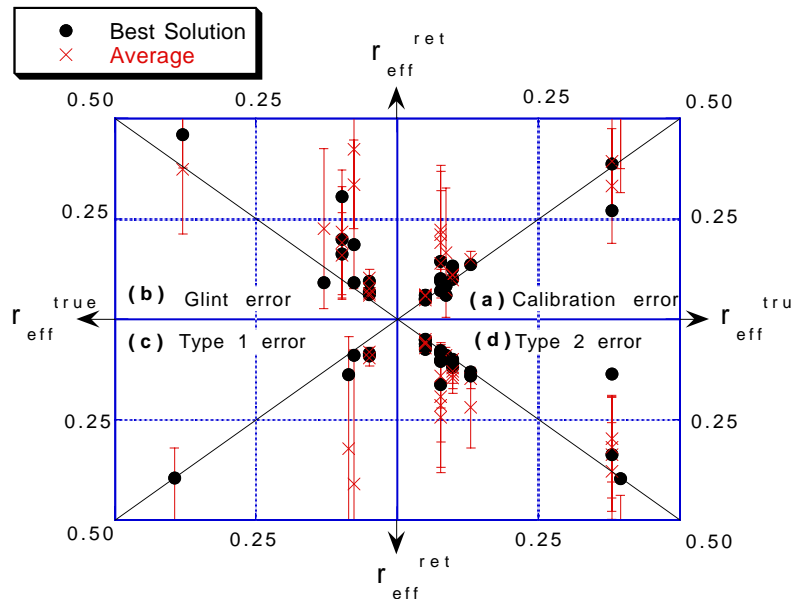
Figure 7-b. Same as in Fig. 7-a but for effective radius smaller than 0.40μm.

• Asymmetry parameter g.

The presence of these errors does not affect the conclusions made earlier for the asymmetry parameter g. In fact, the retrieval of the asymmetry parameter is still very reliable with all the errors introduced (see Fig. 8). Again, the glint error affects more severely the results than the other sources of errors but in an unbiased way.
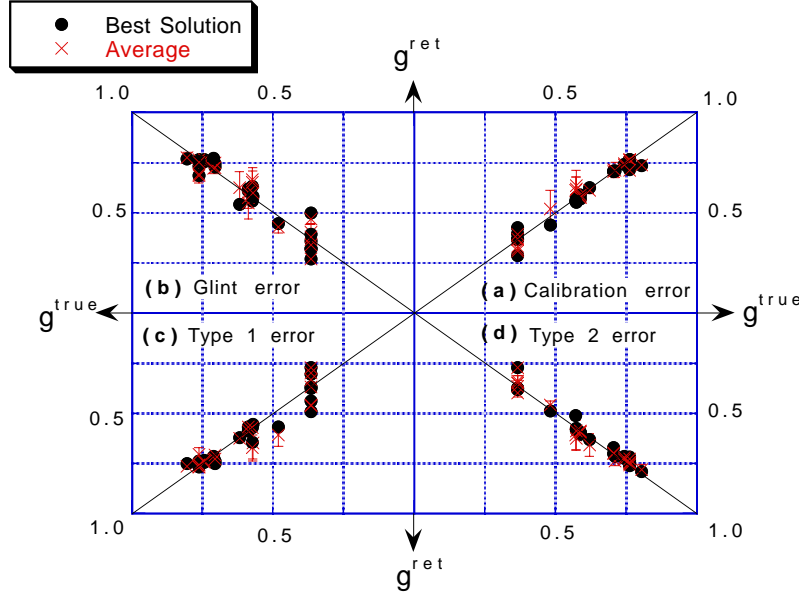
Figure 8. Same as in Fig. 5 but for the asymmetry factor g.

4. ALGORITHM DESCRIPTION - LAND

4.1 Strategy

First, lets review briefly the radiative transfer theory applied to the remote sensing of the aerosol over the land. The remote sensing of aerosol over the land stems from the relationship between the measured radiance at the top of the atmosphere ρ^* (given in apparent reflectance units - $\rho^*=\pi L/F_0\mu_o$, where L is the radiance at the top of the atmosphere, F_0 is the extraterrestrial solar flux and μ_o is the cosine of the solar zenith angle), and the surface bi-directional reflectance properties $\rho(\theta,\theta_O,\phi)$:

$$\rho^*(\theta,\theta_O,\phi) = \rho_a(\theta,\theta_O,\phi) + F_d(\theta_O)T(\theta)\rho(\theta,\theta_O,\phi)/(1-s\rho') \qquad \text{(Eq. 8)}$$

where θ is the view direction, θ_O is the solar zenith angle and ϕ is the azimuth of the scattered radiation from the solar beam. $\rho_a(\theta,\theta_O,\phi)$ is the path radiance, $F_d(\theta_O)$ is the normalized downward total flux for zero surface reflectance, equivalent to the total downward transmission. Its value is less than 1.0 due to aerosol and molecular absorption and backscattering of sunlight to space. $T(\theta)$ is the upward total transmission into the direction of the satellite field of view, s the atmospheric backscattering ratio and ρ' the surface reflectance averaged on the view and illumination angles.

In the single scattering approximation, the path radiance is proportional to the aerosol optical thickness, τ_a, the aerosol scattering phase function, $P_a(\theta,\theta_O,\phi)$, and single scattering albedo, ω_o:

$$\rho_a(\theta,\theta_O,\phi) = \rho_m(\theta,\theta_O,\phi) + \omega_o\tau_a P_a(\theta,\theta_O,\phi)/(4\mu\mu_o) \qquad \text{(Eq. 9)}$$

where $\rho_m(\theta,\theta_O,\phi)$ is the path radiance due to molecular scattering, and μ and μ_o are cosines of the view and illumination directions, respectively. The functions F_d, T, and s in Eq. 8 are also dependent on ω_o, τ_a, and P_a, though for small surface reflectance they are less important. However, in order to derive the aerosol optical thickness from the measured radiance, an aerosol model that provides values of ω_o and P_a for specific conditions is required.

The contribution of $\rho*$ from the path radiance is larger for shorter wavelengths, and for low values of the surface reflectance (e.g., $\rho \leq 0.06$ - see Fig. 9). Therefore, the errors in deriving the aerosol optical thickness are smaller for these conditions. The bi-directional reflectance properties of ρ are approximated here by the direct value of the reflectance for the illumination and viewing directions. The error from this approximation is small for dark surfaces to derive the aerosol path radiance and optical thickness (Lee and Kaufman, 1986).

Errors due to uncertainty in the aerosol absorption, given by the single scattering albedo, ω_o, are also smaller for low surface reflectance. Independent of the value of the surface reflectance, the derivation of the optical thickness from the path radiance is also affected by the uncertainty in the scattering phase function, which will be discussed in detail later in sectin 4.2. Many land covers (such as vegetation and some soils) are dark in the red (0.60-0.68 μm) and blue (0.4-0.48 μm) wavelengths. Therefore, it is appropriate to use the darkest pixels in the image to estimate the aerosol optical thickness (or loading) and its effect on remote sensing at these wavelengths. But in order to use Eq. 1 to estimate accurately the path radiance (ρ_a) and the optical thickness, the surface reflectance of these dark pixels have to be estimated within a small uncertainty of $\Delta\rho = \pm0.005$ to ±0.01.
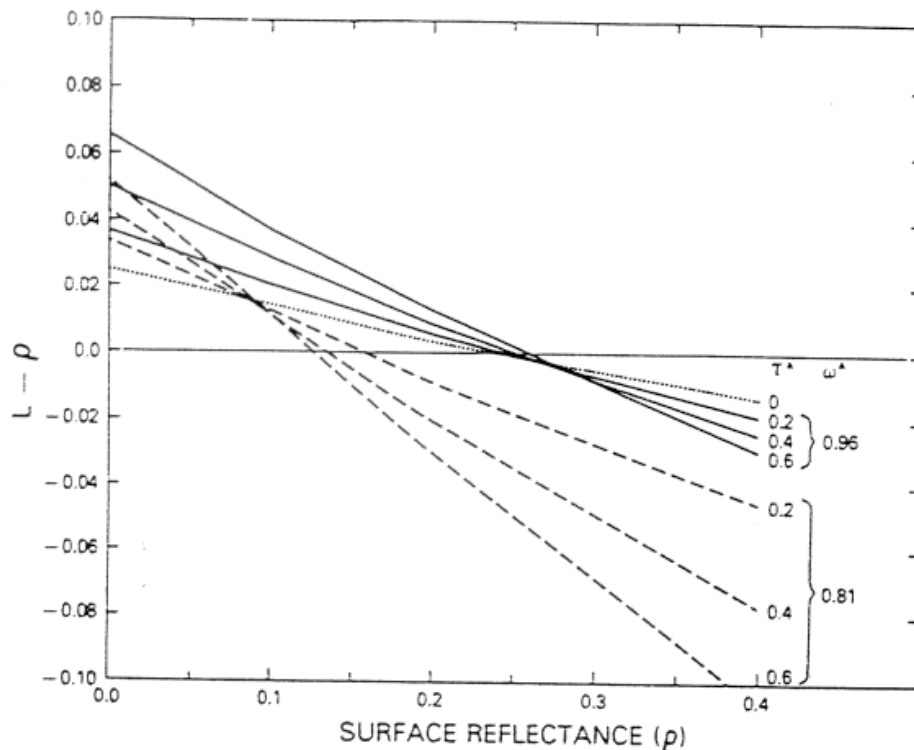
Figure. 9. The radiance, L, at the top of the earth-atmosphere system (in reflectance units) minus the surface reflectance, ρ, for nadir observation as a function of the surface reflectance. The total aerosol optical thickness τ_a and the single scattering albedo ω_0 are indicated for each line. The solar zenith angel is 40°, the wavelength is 0.61 μm. Power law size distribution was used with $\nu=3$. Note that the atmospheric effect is zero for an empty atmosphere, (L - ρ = 0) and the aerosol effect is zero for the dotted line (pure molecular scattering). For surface reflectance under a given critical value (ρ_c) the aerosol effect is positive ($\rho_c=0.25$ for $\omega_0=0.96$) and above this value the effect is negative. (after Fraser and Kaufman, 1985).

The strategy for remote sensing of aerosol over the land from EOS-MODIS is based on the following physical principles:

• Except for dust, the aerosol effect on the radiance measured from space, decreases with wavelength as λ^{-1} to λ^{-2} (Kaufman, 1993). Therefore the effect is much smaller in the mid-IR than in the visible.

• The radiative effect of aerosol includes backscattering and absorption of the direct sunlight and sunlight reflected from the surface. For dark surfaces, the scattering effect dominates while for brighter surfaces the effect is mixed. Therefore, the aerosol radiative effect is strongest for low surface reflectance. The remote sensing of

aerosol using dark targets can be best done for surface reflectance $\rho \leq 0.06$. In the following, we will describe a method to find the surface cover that has this low reflectance in selected wavelengths.

• The surface reflectance across the solar spectrum is correlated to some extent. Soils usually have an increasing reflectance as a function of the wavelength with correlation between the reflectances slowly decreasing with an increase of the wavelength span. Parallel processes affect the reflectance in the 0.47 and 0.66 μm channels and in the 2.1 and 3.8 μm channels. The presence of vegetation decreases the reflectivity in the visible channels due to chlorophyll absorption and in the mid-IR channels due to absorption by liquid water associated with the plant. Wet soil has a lower reflectance in the visible channels due to light trapping, and in the 2.1 and 3.8 μm channels due to the liquid water absorption. Moreover, surface roughness, shadows and inclinations decrease the reflectance across the whole solar spectrum (Kaufman and Remer, 1994).

Based on these principles, the basic approach for an operational and unsupervised aerosol remote sensing algorithm is described as follows:

• Determination of the presence of the dark pixels in the blue (0.47 μm) and red (0.66 μm) channels using their remotely sensed reflectance in the mid- IR channels (2.1 and 3.8 μm).

• Estimation of the surface reflectance of the dark pixels in the red and blue channels using the measurements in the mid-IR.

• Determination of the aerosol type using information on the global aerosol distribution (Husar et al., 1996; d'Almeida et al., 1991) and the ratio between the aerosol path radiance in the red and blue channels.

• Selection of the appropriate dynamical aerosol model (Remer et al., 1996a) that describes the aerosol size distribution, refractive index, single scattering albedo and effect of nonsphericity on the phase function. The models are derived from analysis of ground based remote sensing of the ambient column aerosol size distribution, and in situ measurements.

• Inversion of the measured radiance at satellite level into the aerosol optical thickness, volume (or mass) concentration and spectral radiative forcing using radiative transfer look-up tables computed for the dynamical aerosol models (e.g., Fraser et al., 1992).

In the following, we shall describe this approach, and its physical basis.

4.2 The Use of Dark Targets

First application of dark targets in an aerosol retrieval algorithm (Kaufman and Sendra, 1988; hereinafter referred to as KS88) was based on the detection of green

forests as dark pixels using the vegetation index (NDVI) and the near IR reflectance. Dark vegetation was determined by high NDVI and low reflectance in the near IR. For these pixels, the reflectance in the red channel is assumed as $\rho=0.02\pm0.01$ and used to derive the aerosol optical thickness. Application of this technique to Landsat MSS data over the mid-Atlantic region of the US showed a very good agreement against sunphotometer measurements (KS88). In order to derive the optical thickness from the path radiance, the aerosol size distribution, single scattering albedo and refractive index have to be assumed. Spherical and homogeneous aerosol particles are also assumed in order to use the Mie theory in the calculations, unless non-sphericity is identified (Kahn et al., 1996) and modeled (Mishchenko and Travis, 1994; Nakajima et al., 1989). Sensitivity studies showed that in a general case these assumptions can generate substantial errors in the derived aerosol optical thickness (~30%). To reduce the errors, a good model of the aerosol properties based on measurements is required. In regions where the model is most applicable, we can expect the remote sensing procedure to be more accurate. This was the case in the application of the method by KS88 to the mid-Atlantic region where the aerosol model was better known. KS88 further applied the derived aerosol optical thickness for atmospheric corrections of remote sensing of the surface reflectance. They noticed that since the same assumptions are used in the derivation of the aerosol optical thickness from the path radiance and in the process of atmospheric correction, a large part of the errors in the aerosol model were canceled out. This reduction in errors may occur also in the determination of the aerosol direct radiative forcing, which is closely linked to the path radiance used to derive the optical thickness. These topics will be discussed later in section 4.6.

The determination of dark pixels using the vegetation index is not well suited for global applications, since the vegetation index itself is affected by the aerosol, a feedback circle that causes the method to be applied only to images for which it is known *a priori* that dense vegetation pixels are present in the image. An alternative technique is suggested to locate the dark pixels using longer wavelengths (2.1 or 3.8μm) that are less sensitive to aerosol scattering (since these wavelengths are much longer than the size of most aerosol particles) but are still sensitive to surface characteristics. Such wavelengths has been used to find dark pixels in the visible channels (Holben et al, 1992).

Figure 10 demonstrates the spectral properties of vegetation and the effect of smoke aerosol on the apparent reflectance. In this figure, spectral radiance from the AVIRIS aircraft spectral imager over dry grassland in California are plotted. The solid line is the spectrum of surface reflectance for a clean atmosphere. The dashed lines are for observations of a nearby surface through thin smoke from a smoldering section of a wild fire. The smoke has a large effect in the visible part of the spectrum, decreasing in magnitude with wavelength from the blue to the red region. In the near IR, the aerosol effect is smaller than the variations in the surface reflectance between the smoke free area and the area affected by smoke. Therefore, the smoke effect is not observable in the mid-IR (2.2 μm) due to the large ratio of wavelength to the size of particles.
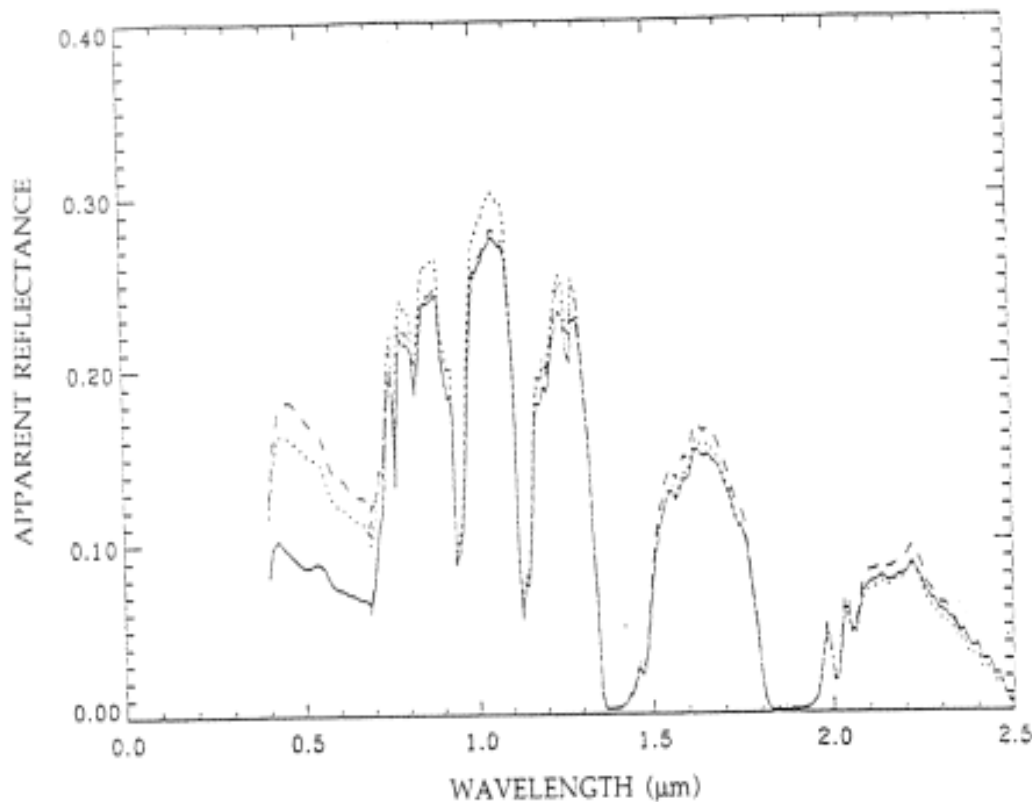
Figure 10. The spectral radiance measured from the AVIRIS aircraft spectral imager over dry grassland in Stockton, northern California, acquired Aug. 20, 1992, and plotted in reflectance units (Gao et al., 1993). The solid line is for the spectral surface reflectance in the presence of a clean atmosphere while the dashed and dotted lines are for observations of a nearby surface through thin smoke from a wildfire (more smoke for the dashed line spectrum). The smoke has a large effect in the visible part of the spectrum, decreasing with wavelength from the blue to the red region. The effect is smaller than variation in the surface high reflectance in the near IR, and is small in the mid-IR (2.2 μm) due to the large ratio of the wavelength of radiation to the size of particles.

Analysis of AVHRR images over Eastern US and over Brazil shows that the AVHRR 3.7 μm channel is not sensitive to the presence of pollution aerosol or smoke (Kaufman et al., 1990b; Kaufman and Remer, 1994) but is very sensitive to the presence of forest pixels and can be used for their determination. The apparent reflectance in the 3.7 μm AVHRR channel is well correlated with the reflectance at 0.64 μm (see Fig. 11), though the ratio between the surface reflectance at 3.7 μm and 0.64 μm changes from day to day. Note that to use the reflective part of the 3.7 μm channel it has to be corrected for thermal emission and for absorption by water vapor (Roger and Vermote,

1996). This prompted us to test if the MODIS nearby channel of 3.8 μm, located around 4.0 μm (not sensitive to water vapor absorption), is better for this application.

The MODIS 3.75 and 3.95 μm channels are expected to be shifted by 50 nm than originally planned. The 4.0 μm channel is sensitive to N_2 absorption, which is about as strong as the water absorption at 3.8 μm in a standard atmospheric model (vertical transmission of 90% due to H_2O at 3.8 μm and 88% due to N_2 at 4.0 μm). Although N_2 absorption does not vary substantially and is well known, its emission also depends on the temperature profile in the atmosphere. Sensitivity study shows that the uncertainty in the retrieved surface reflectance at 4.0 μm due to the error of vertical temperature profile is about 10%. Compared to 20% uncertainty obtained in the retrieved surface reflectance at 3.8 μm from a 10% error in total precipitable water vapor, the 4.0 μm channel is certainly better in this regrad. But the fraction of reflected sunlight at the 4.0 μm channel is only 60% of that at 3.8 μm for the same surface reflectance. Since the reflectance at 3.8 or 4.0 μm is computed after the correction for emission by both atmosphere and surface using MODIS 11 μm channel, the lower fraction of reflected light will enhance the errors in the application due to uncertainty in the surface emissivity at 11 μm. Uncertainty in emissivity at 11 μm of $\Delta\varepsilon^{\pm}0.02$, as found, corresponds to uncertainty in the surface reflectance of 25% at 3.8 μm (for $\rho_{3.8}$=0.025; Kaufman and Remer, 1994), and correspondingly 50% up to twice as large is found at 4.0 μm due to the smaller fraction of the reflective part. This compensates more than the error due to water vapor absorption at 3.8 μm as opposed to the vertical temperature profile at 4.0 μm. Therefore, it can be concluded that the 3.8 μm channel is better for this application.

As shown above, for surface reflectance of $\rho_{3.8} = 0.025$, correction for attenuation by water vapor absorption result in an error of $\Delta\rho_{3.8} = 0.005$ for an uncertainty of 10% in total precipitable water vapor. The uncertainty of emissivity at 11 μm of $\Delta\varepsilon = {}^{\pm}0.02$ also causes approximately 25% error in surface reflectance at 3.8 μm (Kaufman and Remer, 1994). Therefore, the variation in the relationships shown in Fig. 11 from day to day of AVHRR data may result from inaccuracy of the correction for emission and water vapor absorption. Nevertheless, several successful applications of this channel for remote sensing of smoke aerosol were reported (Holben et al., 1992; Vermote et al., 1996). The application to MODIS should be significantly better due to better instrument characterization and the availability of total precipitable water vapor information.

Figure 12 shows examples of the relationships between the surface reflectance at 2.1 μm and that at 0.47 μm and 0.64 μm, derived from Landsat TM and AVIRIS images over the mid-Atlantic US. Here, the reflectances were corrected for the atmospheric effects based on ground based measurements of the aerosol optical thickness. The images include forested area and crop land, as well as exposed soil, residential area and water. The data averaged for the specific surface types are shown in Fig. 13. For dark targets (reflectance at 2.1 μm <0.10), the uncertainties in the estimate of surface reflectance in the visible channels from the 2.1 μm channel reflectance are ±0.005 to

±0.01 for the red and blue channels respectively. This issue is currently under intensive study to find how can it be applied globally and in which conditions does it fail (e.g., snow or water).

4.3 Global Remote Sensing of Aerosol Over Land

The following procedures for global remote sensing of aerosol are emerging for the multispectral EOS-MODIS radiometer. The MODIS spectral channels used in the analysis of aerosol are the 250 m resolution 0.66 μm channel, the 500 m resolution 0.47 μm and 2.1 μm channels and the 1 km resolution 3.8 μm channels. The latter two channels are used for the determination of surface reflectance. The 11 μm window channel to correct for emission (for 3.8 μm channel) from the Earth surface is also required. Other gaseous absorption channels, such as near IR (~1 μm) water vapor channels for the correction of total precipitable water vapor and 9.6 μm channel for total ozone correction, need also to be included. Since the correction for water vapor and ozone absorption is straightforward, it therefore will not be addressed in this ATBD. Cloud mask which is crucial in determining cloud-free pixels will be shown in detail in the ATBD for cloud mask. The automatic procedures to derive global distribution of aerosol optical thickness, mass concentration and radiative forcing in cloud-free regions are shown as follows

Step 1. Selection of dark pixels and determination of their surface reflectance

The selection of the pixels in the MODIS image used to derive the aerosol optical thickness is based upon our experience with the 3.8 μm and 2.1 μm reflectances and their relationship to the reflectance in the visible channels. The technique prioritizes the criteria in order to minimize the residual error in the predicted surface reflectance, and consequently in the derived aerosol optical thickness. It may be biased by the broader experience with application of the 3.8 μm channel rather than the 2.1 μm channel for predicting the surface reflectance in the red and blue channels and in consequence for the remote sensing of aerosol (Holben et al., 1992; Kaufman and Remer, 1994; Vermote et al., 1996; Kaufman and Tanré, 1996; Kaufman et al., 1996; Kaufman and Fraser, 1996). We found that the highest accuracy in predicting the surface reflectance in the red and blue channels is for pixels that do not represent water and have a very low reflectance at 2.1 μm.

Once the reflectance is larger than 0.05, the uncertainty in the relationship between the reflectance at 2.1 and 0.66 or 0.47 μm makes the 3.8 μm channel more attractive, despite the need to correct for surface emission. If the surface is not dark enough in both 2.1 and 3.8 μm channels, the derivation of aerosol is still possible but with lower expected accuracy due to the high surface reflectance estimated (Kaufman et al., 1996).
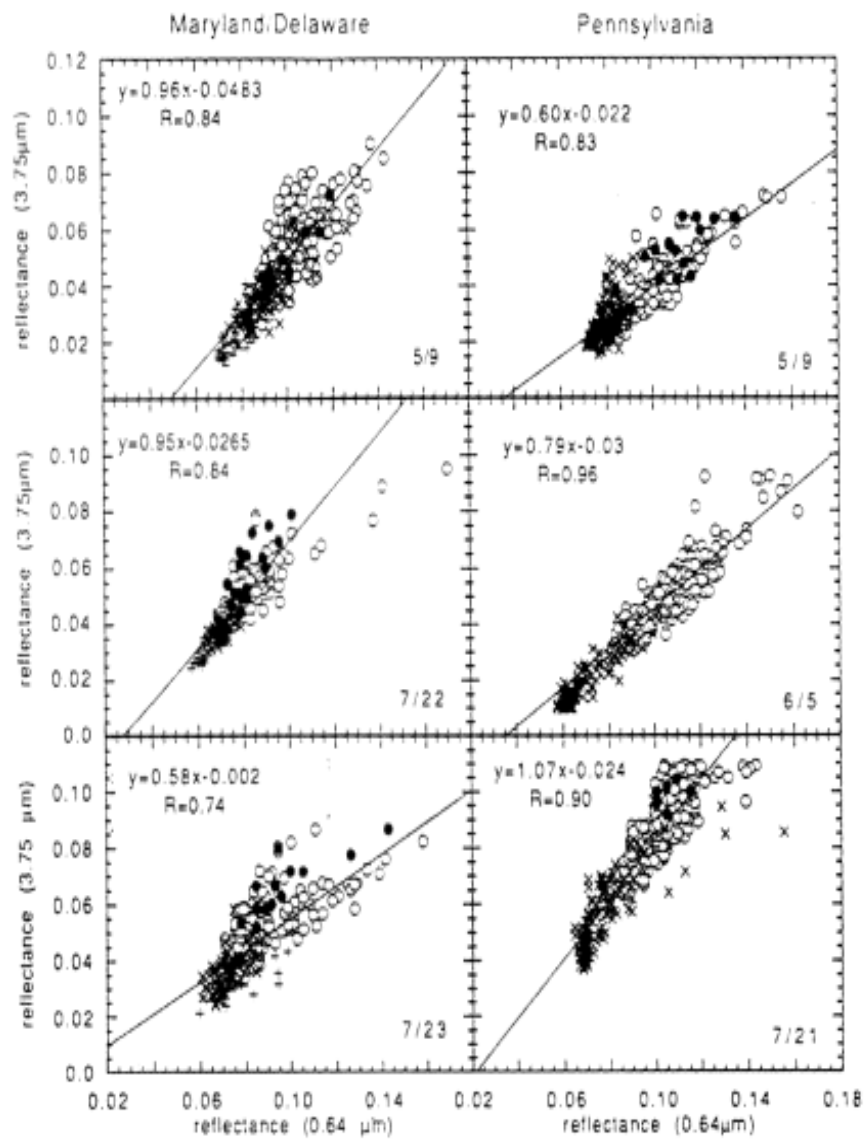
Figure 11. Scatter diagrams of the relationship between the apparent surface reflectance in the red (0.64 μm) and the mid IR (3.7 μm) AVHRR channels. (after Kaufman and Remer, 1994)
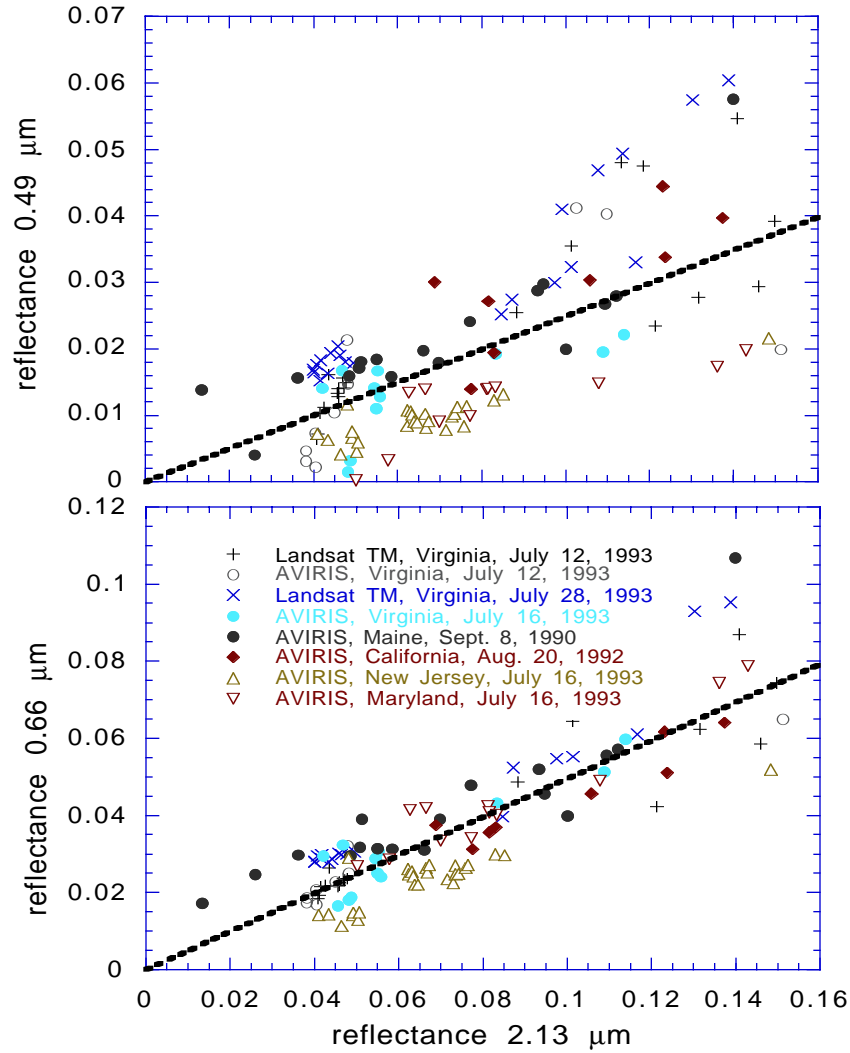
Figure 12. Scatter diagrams between the surface reflectance at 0.49 μm ($\rho_{0.49}$), 0.66 μm ($\rho_{0.66}$) and that at 2.2 μm ($\rho_{2.2}$). A different symbol is used for each of the Landsat TM or AVIRIS images (see notations in the bottom figure). The remotely sensed data were corrected for the atmospheric effect before display. The average relationships $\rho_{0.49}/\rho_{2.2}$=0.25 and $\rho_{0.66}/\rho_{2.2}$=0.5 are also plotted (Kaufman et al., in preparation).
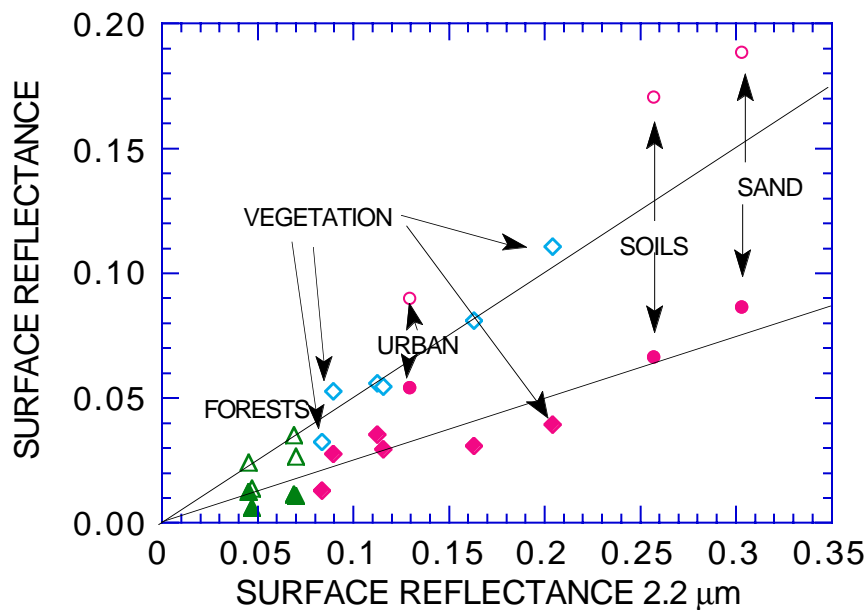
Figure 13. Scatter diagram between the surface reflectance at 0.49 μm (full symbols) and 0.66 μm (empty symbols) to that at 2.2 μm, for several surface types. The average relationships $\rho_{0.49}/\rho_{2.2}=0.25$ and $\rho_{0.66}/\rho_{2.2}=0.5$ are also plotted (solid lines).

For a grid box of 10 x 10 pixels of 1 km resolution at nadir, and correspondingly higher number of 500 m and 250 m resolution pixels, the number of the dark pixels $N_{\lambda i}$ that have an apparent mid-IR reflectance $\rho^*_{\lambda i}$ less than a threshold $(\rho^{th}_{\lambda i})$ is determined based on the following priority of criteria (the surface reflectance ρ^s_λ is indicated for each case):

first priority: $\quad N_{2.1}$ for $0.01 \leq \rho^*_{2.1} \leq 0.05 \quad (\rho^s_{0.47}=\rho^*_{2.1}/4, \rho^s_{0.66}=\rho^*_{2.1}/2)$

second priority: $N_{3.8}$ for $\rho^*_{3.8} \leq 0.025 \quad (\rho^s_{0.47}=0.01, \rho^s_{0.66}=0.02)$

third priority: $\quad N_{2.1}$ for $0.01 \leq \rho^*_{2.1} \leq 0.10 \quad (\rho^s_{0.47}=\rho^*_{2.1}/4, \rho^s_{0.66}=\rho^*_{2.1}/2)$

fourth priority: $\quad N_{2.1}$ for $0.01 \leq \rho^*_{2.1} \leq 0.15 \quad (\rho^s_{0.47}=\rho^*_{2.1}/4, \rho^s_{0.66}=\rho^*_{2.1}/2)$

The criteria are used only over land surfaces excluding water, clouds, ice and snow. The first criterion in this list that represents more than 5% of the pixels in the grid box is chosen to derive the aerosol optical thickness, though the results of the other criteria are also stored. The quality of the derivation is expected to decrease with the priority rank. The thresholds and surface reflectance determination are based on

Figs. 11-13. We do not use pixels with reflectance at 2.1 μm, $\rho^*_{2.1}$, larger than 0.15, since the relationship between the reflectance in the visible channels and the 2.1 μm channel is significantly more chaotic for $\rho^*_{2.1} > 0.15$ in some regions (Kaufman et al., 1996). The division into three segments of $\rho^*_{2.1}$ is based on the assumption, which is based on measurements of surface properties, that there is a higher probability of a larger absolute error associated with larger surface reflectance. Still, it is not clear how the 3.8 μm threshold relates to the 2.1 μm threshold. We do not have yet remote sensing data to compare the two. We choose the 2.1 μm channel to be the first priority simply because the 3.8 μm channel requires correction for surface emission and water vapor absorption and the lowest threshold of 2.1 μm channel can be the more accurate for the determination of surface reflectance .

Step 2. Preliminary derivation of the optical thickness

In the first stage, it is not clear which aerosol model should be used because of different aerosol types possibly detected in the image. Therefore the aerosol optical thickness is first derived in the red and blue channels from $\rho^*_{\lambda i}$ and $\rho^s_{\lambda i}$ using a continental model (Lenoble and Brogniez, 1984). The parameters are given in Table 7. Also tabulated in Table 7 are the parameters of industrial/urban and biomass burning models (Remer et al., 1996a, 1996b) and dust model (Shettle, 1984). Due to possibly a wrong choice of the scattering phase function and single scattering albedo, the derived aerosol optical thickness is expected to be less accurate. Therefore, a correction is performed, which will be discussed next in step 3. In the inversion process, the aerosol optical thickness is derived using a look-up table (generated from continental aerosol model) that relates a Lambertian surface reflectance to the measured radiance as a function of the optical thickness and the viewing and illumination geometry (e.g., Fraser et al., 1984, 1992; Kaufman et al., 1990). The values of $\rho^*_{\lambda i}$ and $\rho^s_{\lambda i}$ used in the retrieval of aerosol optical thickness in the grid of 10x10 km box are the average of 10-40 lowest percentile of the selected dark pixels, from which the standard deviation is also calculated.

Step 3. Determination of the aerosol model

The aerosol model is determined using the optical thickness derived from step 2 and the ratio of the aerosol single scattering path radiance $L_{p\lambda}$, $(L_{p\lambda}=\tau_\lambda P_\lambda \omega_\lambda)$ in the red and blue channels. Here, we use continental model to compute the single scattering radiance, which is used later to determine the aerosol model. This apparently contradicting application is based on the assumption that the aerosol model is only of a secondary importance in determining multiple scattering, in which the details of phase function are masked out. For small optical thicknesses $\tau_{red} < 0.15$, we do not expect the measured spectral radiance to be sensitive enough to determine the aerosol model:

Therefore, if: $\tau_{red} < 0.15$ then the continental model is used,

Table 7. Summary of the aerosol dynamic models. The aerosol parameters of continental model are from Lenoble and Brogniez (1984) and for dust model from Shettle (1984). The Parameters of the aerosol models of industrial/urban and smoke used in the remote sensing procedure are after Remer et al. (1996a&b), where the parameters are for a combination of lognormal size distributions given by the number distribution, or by the volume distribution:

$$\frac{dN}{d\ln r} = \frac{N_o}{\sigma\sqrt{2\pi}}\exp[-\frac{[\ln(r/r_g)]^2}{2\sigma^2}] \qquad \frac{dV}{d\ln r} = V_o\exp[-\frac{[\ln(r/r_v)]^2}{2\sigma^2}]$$

where N_O is the number of particles per cross section of atmospheric column (cm^{-2}), r_g the mean radius of the number distribution, σ the standard deviation of ln(r), and r_v the volume mean radius, $r_v = r_g \cdot \exp[3\sigma^2]$, V_O the column volume of the particles per cross section of the column (cm^3/cm^2), which is given by

$$V_o = \frac{1}{\sigma\sqrt{2\pi}}e^{-\frac{9}{2}\sigma^2}N_o\left(\frac{4\pi}{3}\right)r_v^3$$

Note that "†" for biomass burning aerosol we use same real and imaginary part of refractive index (i.e., 1.43-0.0035i) as for industrial aerosol but allow for external mixing of graphitic carbon. This results in greater absorption and smaller ω_0. For the dust model, an aerosol of scale height of 2 km was assumed to match the unit of V_0. The water soluble aerosol of continental model (*) is a wide mode encompassing both nuclei and accumulation modes.

Continental aerosol	r_g(μm)	r_V(μm)	σ	V_0(10^6 cm^3/cm^2)	ω_0 (670nm)
Water Soluble*	0.005	0.176	1.090	3.050	0.96
Dust Like	0.500	17.60	1.090	7.364	0.69
Soot	0.0118	0.050	0.693	0.105	0.16
Biomass burning	r_g(μm)	r_V(μm)	σ	V_0(10^6 cm^3/cm^2)	ω_0(670nm) †
Accumulation	0.061	0.130	0.500	-2.4+45τ	0.90
Stratospheric	0.380	0.510	0.310	0.984	0.98
Coarse	1.0-1.3τ	6.0-11.3τ+61τ^2	0.69+0.81τ	2.4-6.3τ+37τ^2	0.84
Industrial/urban aerosol	r_g(μm)	r_V(μm)	σ	V_0(10^6 cm^3/cm^2)	ω_0 (670nm)
Accumulation 1	0.036	0.106	0.60	-2.0+70τ-196τ^2+150τ^3	0.96
Accumulation 2	0.114	0.210	0.45	0.34-7.6τ+80τ^2-63τ^3	0.97
Stratospheric	0.430	0.550	0.29	0.73	0.98
Salt	0.990	1.300	0.30	-0.16+4.12τ	0.92
Coarse	0.670	9.500	0.94	1.92	0.88
Dust aerosol	r_g(μm)	r_V(μm)	σ	V_0(10^6 cm^3/cm^2)	ω_0 (670nm)
Dust Background					
1st mode	0.0010	0.0055	0.755	6.0x10^{-6}	0.015
2nd mode	0.0218	1.230	1.160	1.0	0.95
3rd mode	6.2400	21.50	0.638	0.6	0.62

Otherwise: If $L_{p-red}/L_{p-blue} > T_{h1}(\Theta)$ then the dust model should be used.

If $L_{p-red}/L_{p-blue} < T_{h2}(\Theta)$ then non-dust model (smoke or urban/ industrial aerosol determined based on location and season described below). Between the two thresholds $T_{h1}(\Theta)$ and $T_{h2}(\Theta)$, a linear interpolation of the models is used. Such interpolation will produce a model that includes accumulation mode due to smoke or industrial/urban pollution and a coarse mode from soil dust, which is in essence a type of continental model. The values of the threshold as a function of the scattering angle Θ are based on theoretical computations of the ratio between the two path radiances (see Fig. 14) and are given by:

for $40° \leq \Theta \leq 150°$ $T_{h1}(\Theta)=0.90$ and $T_{h2}(\Theta)=0.72$;

for $150° \leq \Theta < 168°$ $T_{h1}(\Theta)=0.9-0.01(\Theta -150)$ and $T_{h2}(\Theta)=0.72$;

for $\Theta \geq 168°$, it is not possible to distinguish between the aerosol types and the phase function is not well predictable due to its strong dependence on size and shape of the particles.

For non-dust, non-continental model cases, the separation between smoke aerosol and industrial/urban aerosol are performed based on geographic locations and seasons (see Fig. 15) (d'Almeida et al., 1991; Hao and Liu, 1994; Husar et al., 1996), which can be categorized in latitude and longitude zones as follows:

Industrial/Urban aerosol
North America and Europe: (100W-50E; 30N-70N).
South East Asia: (105E-150E: 15N-45N).
Central America and Africa (May-November): (100W-50E; Equator-30N).
South America and Africa (December-April): (100W-50E; 65S-Equator).

Smoke
Central America and Africa (December-April): (100W-50E; Equator-30N).
South America and Africa (May-November): (100W-50E; 65S-Equator).
The rest of the world.

It should be noted that this definition of zones of industrial/urban aerosol and smoke is experimental and preliminary. To be implemented into retrieval scheme, the cut into square boxes of latitude and longitude is necessary. However it may show some types of aerosols that do not exist locally; for example, the dominant industrial/urban aerosol in Saudi Arabia and some east parts of Africa. Because of the bright desert surface, our algorithm can't retrieve aerosol properties over those regions anyway with the present automatic procedures. Antarctic continent (> 65°S) and Arctic region (> 70°N) are considered to be free of aerosol contamination. To be more confident of the regions for different types of aerosols, it is currently being evaluated using the SCAR data base (see section 4.4) and any related informations, and certainly will be revaluated globally after MODIS launch.
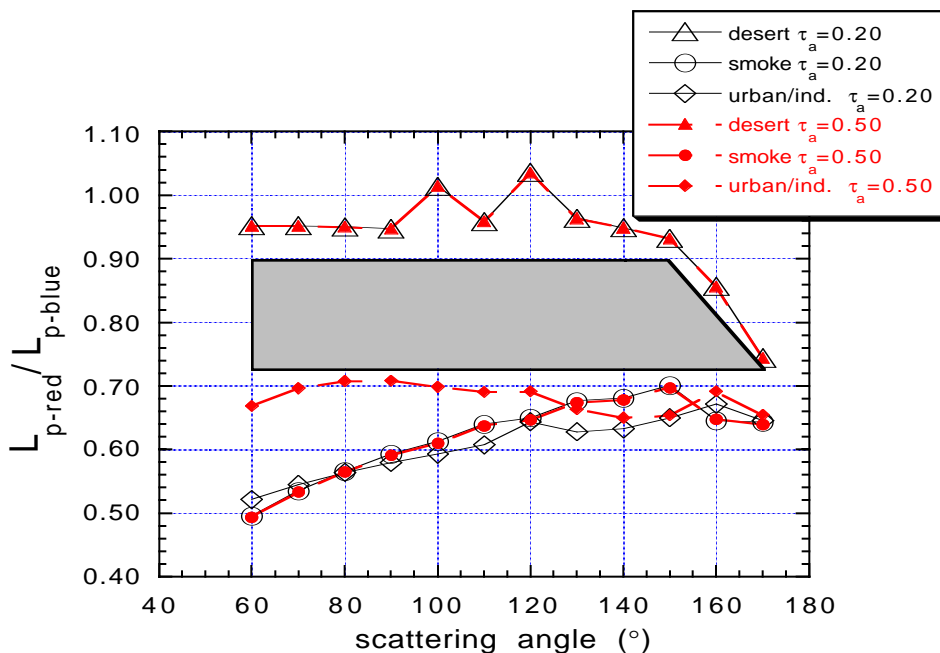
Figure 14. Ratio of the aerosol single scattering path radiance, L_p, in the red to the blue channel as a function of the scattering angle. The ratio is plotted for the dust, smoke and urban/industrial model for two aerosol optical thicknesses. For dust the background aerosol model of Shettle (1984) was used and for smoke from biomass burning and the urban/industrial aerosol the dynamic models (Remer et al., 1996a,b) were used. The difference between the ratio for dust and non-dust aerosol is used to distinguish between them. The gray zone is the separation zone between the dust and non-dust algorithms.
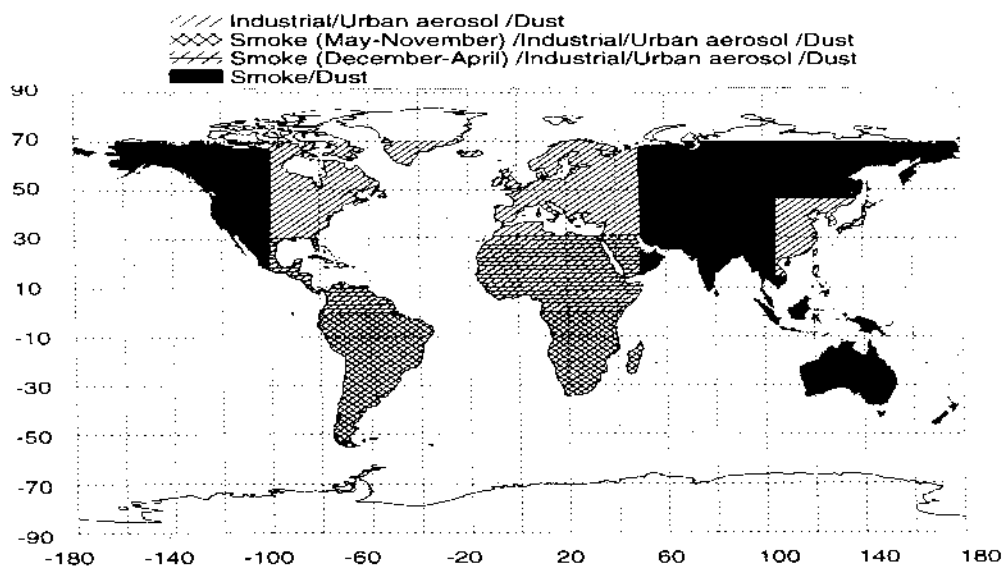
Figure 15. Map of the global distribution of assumed regions of smoke and urban/industrial aerosol based upon d'Almeida et al. (1991), Hao and Liu (1994) and Husar et al. (1996). Note that in this figure, we do not attempt to separate dust from smoke or industral/urban aerosol. Dust is distinguishable from smoke or industrial/urban aerosol in the algorithm based upon the spectral dependence of the path radiance.

Step 4. Reconfiguration of the optical thickness

Once the aerosol model is determined, the optical thicknesses τ_{red} and τ_{blue} can be corrected for the difference between the newly determined aerosol model and the previously used continental model. The correction is based on the aerosol single scattering radiance, $L_{p\lambda}$, derived from the MODIS measured radiances. This radiance (see Eq. 8) was expressed by the aerosol parameters from the continental model:

$$L_{p\lambda} = \tau_\lambda^{cont.} P_\lambda^{cont.} \omega_\lambda^{cont.} / (4\mu\mu_o) \qquad \text{(Eq. 9)}$$

The same single scattering path radiance can be now expressed by parameters describing the new model:

$$L_{p\lambda} = \tau_\lambda^{new} P_\lambda^{new} \omega_\lambda^{new} / (4\mu\mu_o) \qquad \text{(Eq. 10)}$$

As a result we get the transformation for the optical thickness from the value derived using the continental model, $\tau_\lambda^{cont.}$ and the new value τ_λ^{new}

$$\tau_\lambda^{new} = \tau_\lambda^{cont.} \frac{P_\lambda^{cont.} \omega_\lambda^{cont.}}{P_\lambda^{new} \omega_\lambda^{new}} \qquad \text{(Eq. 11)}$$

As in step 3, the assumption behind this transformation is also that the differences between the phase functions and single scattering albedos do not affect the multiple scattering but they do affect the single scattering radiance. For high optical thickness, where multiple scattering is more important, we may expect errors in the single scattering albedo to be more significant. The values of P_{new} and ω_{new} derived from the dynamic models will be discussed in the next section. Alternative solution is to generate LUT for each aerosol model (such as urban/industrial, biomass burning) and retrieve optical thickness based upon the LUT.

Step 5. Subgrid calculations

In some specific cases, e.g., close to the sources of smoke, the resolution of 10x10 km at nadir may be too crude to capture the strong spatial variability. If these sources are located in a region with surface cover that is dark in the blue and red spectral regions, then a finer resolution grid is justified and possible. In the previous steps, the aerosol optical thickness, τ_λ and std, σ_λ were derived in the red and blue channels for the nominal resolution of 10x10 km at nadir. If the ratio of $\sigma_\lambda/\tau_\lambda > 0.5$ in both blue and red channels, then the variability of the aerosol is considered to be significant. If the number of dark targets, in the 500m resolution is >30, then the grid box is divided into 4 smaller boxes of 5x5 pixels and the analysis is redone but for the average of 10 to 60 percentile, instead of 10 to 40. The retrieved optical thicknesses in the two channels for

each sub-box is also stored as an additional information in the data stream for the 10x10 km resolution grid.

4.4 The Aerosol models

At a global scale, aerosol climatology was summarized by d'Almeida et al. (1991) as an expansion of the work of Shettle and Fenn (1979). They show a compilation of a large amount of data and tabulate the dominant type of tropospheric aerosols as a function of the latitude, longitude and the season. From the physical aerosol properties of refractive index and size distributions, they compute the optical properties at the same spatial and temporal scales for extinction coefficient, single scattering albedo, asymmetry factor and phase function. Some studies were devoted to specific aerosols types: desert aerosols (d'Almeida, 1987; Shettle, 1984), maritime aerosols (Hoppel et al., 1990) or aerosols resulting from biomass burning in tropical regions (Crutzen and Andreae, 1990, Kaufman et al., 1992). The climatology is based on existing measurements, most of them taken at ground level. There is a danger that these measurements do not represent the whole atmospheric column or the properties of the ambient aerosol. Hegg et al. (1995) showed recently, using data derived from the Sulfate Cloud And Radiation experiment - Atlantic (SCAR-A), that the aerosol size distribution varies with altitude in the North-East United States. Optical measurements from ground based sun/sky radiometers (Kaufman et al., 1994; Holben et al., 1996) are used to supplement the climatology with ambient aerosol measurements integrated on the whole column (Kaufman and Holben, 1996; Remer et al., 1996a). These measurements are compared with in situ measurements of the size distribution and the aerosol chemistry measured from aircraft (Hegg et al., 1995; Hobbs et al., 1996; Remer et al., 1996b).

Spectral aerosol optical thickness can be obtained from sunphotometer measurements (Volz, 1954; Flowers et al., 1969; Peterson et al., 1981). Several local sunphotometer networks were established to detect different types of aerosols. Flowers et al. (1969) carried on a network over the United States from 1961 to 1966; d'Almeida et al (1983) performed a similar experiment over North and West Africa from 1980 to 1982 with 11 instruments; Holben et al. (1991) conducted similar effort in the Sahel from 1984 through 1986 using 15 monitoring stations. Extension of the measurements to include the aerosol size distribution and scattering phase function was also performed using inversion of solar almucantar measurements (Kaufman et al., 1994). Single scattering albedo can be estimated from the collection of particles on filters, preferably by aircraft sampling of the entire atmospheric boundary layer and measurements of their absorption (Radke et al., 1991). Alternatively, it can be determined from accurate measurements of the downward flux or radiance (King, 1979; Wang and Gordon, 1993).

A sunphotometer network, the Background Air Pollution Monitoring Network (BAPMoN), has been operated at a global and daily scales. It is managed by the World Meteorological Organization and could be used for correcting satellite images. However, a recent report (Forgan et al., 1994) showed the shortcomings of the BAPMoN measurements for poor calibration of the instruments and the lack of good

monitoring of the data quality. Measurements with an improved AErosol RObot NETwork (AERONET) of automatic sun/sky radiometers were conducted recently in the Amazon basin during intense biomass burning (Holben et al., 1996), in Africa during dust events and in the Eastern US in the presence of industrial and urban pollution (Kaufman and Holben, 1996). The instruments measure in addition to the solar direct flux (e.g., sunphotometry) also the sky and aureole radiance distribution. The retrieved aerosol properties are the optical thickness, the size distribution from 0.05 μm to 10 μm, the aerosol total loading and the scattering phase function (King et al., 1978; Nakajima et al., 1986; Kaufman et al., 1994; Holben et al., 1996). In order to maintain high data quality, the instruments transmit the data through satellite communication networks (GOES and METEOSAT) in real time to a center where the data are analyzed. There are plans to expand aerosol measurements using such networks, as part of the international research and monitoring activities and as part of the support and validation of analysis of remote sensing from future satellite systems (The Earth Observing System, EOS of NASA and POLDER/ADEOS mission of CNES/NASDA).

The aerosol models that result from the two analyzed AERONET deployments are shown in Fig. 16 for the smoke aerosol (top panel) and for aerosol resultant from industrial/ urban pollution (bottom panel). For the industrial/urban aerosol, the model is based on 160 sky measurements collected during the SCAR-A experiment, inverted into the aerosol volume size distribution, corrected for inversion problems (Remer et al., 1996b) and analyzed as a function of the optical thickness (Kaufman et al., 1996; Remer et al., 1996a). For the smoke aerosol, similar analysis is performed for smoke from Cerrado region in Brazil in 1993. In general, 4 main modes of aerosol can be distinguished in this data set:

- For particle radius r<0.3 μm - the aerosol accumulation mode, composed of particles formed from condensation of hot organic gases generated from fire or from oxidation of trace gases (e.g., sulfates, organic particles, nitrates) for the urban/industrial aerosol. The volume of this mode increases with the optical thickness. The average size of the particles is fixed for the biomass burning aerosol but increase with optical thickness for the urban/industrial aerosol. In this case, the increase in optical thickness is associated with more stagnant conditions with older (bigger particles) and higher humidity (more liquid water in the particle). The stagnant conditions also allow more time for cloud interactions that increase the particle size (Hoppel et al., 1990; Kaufman and Tanré, 1994).
- For particle radius 0.3 μm<r<0.8 μm, the troposphere has few particles and for the lower range of optical thickness the stratospheric aerosol volume distribution is seen (see also Kaufman et al., 1994; Shiobara et al., 1991).
- For particle radius 0.8 μm<r<2.5 μm, the maritime salt particle mode which is for the mid-Atlantic region only, with volume that also increases with the total aerosol optical thickness. No salt particles are observed in the middle of South America for the smoke aerosol.
- For particle radius r>2.5 μm, the coarse particle mode. For smoke aerosol these particles are generated in the fire as ash or soil particles suspended in the air by the strong convection. Thus, for smoke, the coarse mode is correlated with the

accumulation mode and the optical thickness. For the industrial/urban aerosol, the coarse mode has independent source with a short lifetime, and is not correlated with the other particle modes.
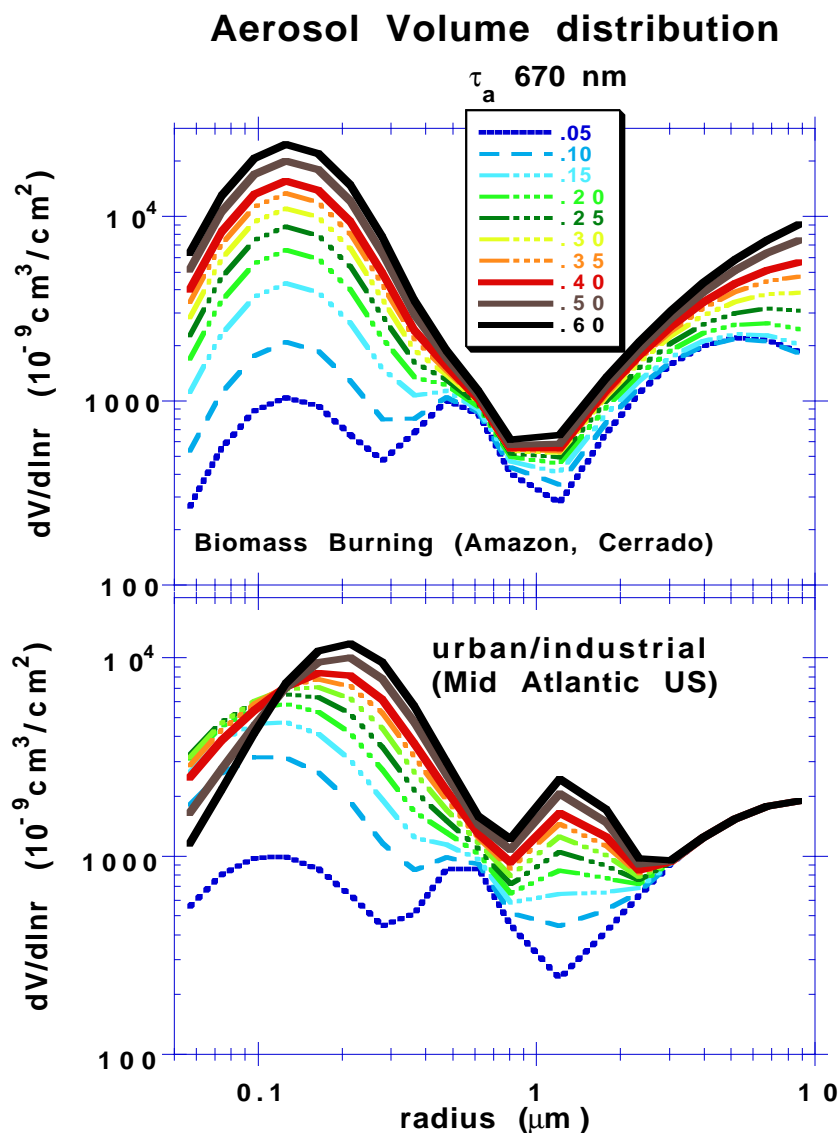

Aerosol Volume distribution

Figure 16. Aerosol models derived from AERONET two deployments, in the Amazon for the smoke aerosol (top panel) and in the Mid Atlantic region of the US, for an industrial/urban aerosol (bottom panel) in 1993. After Remer et al. (1996a). 4 main modes of aerosol can be distinguished: for particle radius r<0.3 μm - accumulation mode of mostly organic smoke particles or sulfates in the urban/industrial aerosol. For 0.3 μm<r<0.8 μm the troposphere has few particles

and the stratospheric aerosol is observed. For 0.8 μm<r<2.5 μm the maritime salt particle mode for the mid-Atlantic region. For 2.5 μm<r the coarse particle mode.

The single scattering phase functions of continental, desert dust, smoke and industrial/urban aerosol models are shown in Fig. 17. Note that the phase functions of industrial/urban and smoke models are strongly a function of optical thickness (Remer et al., 1996a,b). The continental model has phase function values which are intermediate between different aerosol models. The smaller smoke particles result in phase function values which are a factor of 2 larger than those of the industrial/urban aerosol in the backscattering angles. The dust phase function values are significantly larger than both smoke and sulfate aerosol models when scattering angles are >160° and are similar to sulfate model (τ=0.4) for scattering angles between 100° and 130°
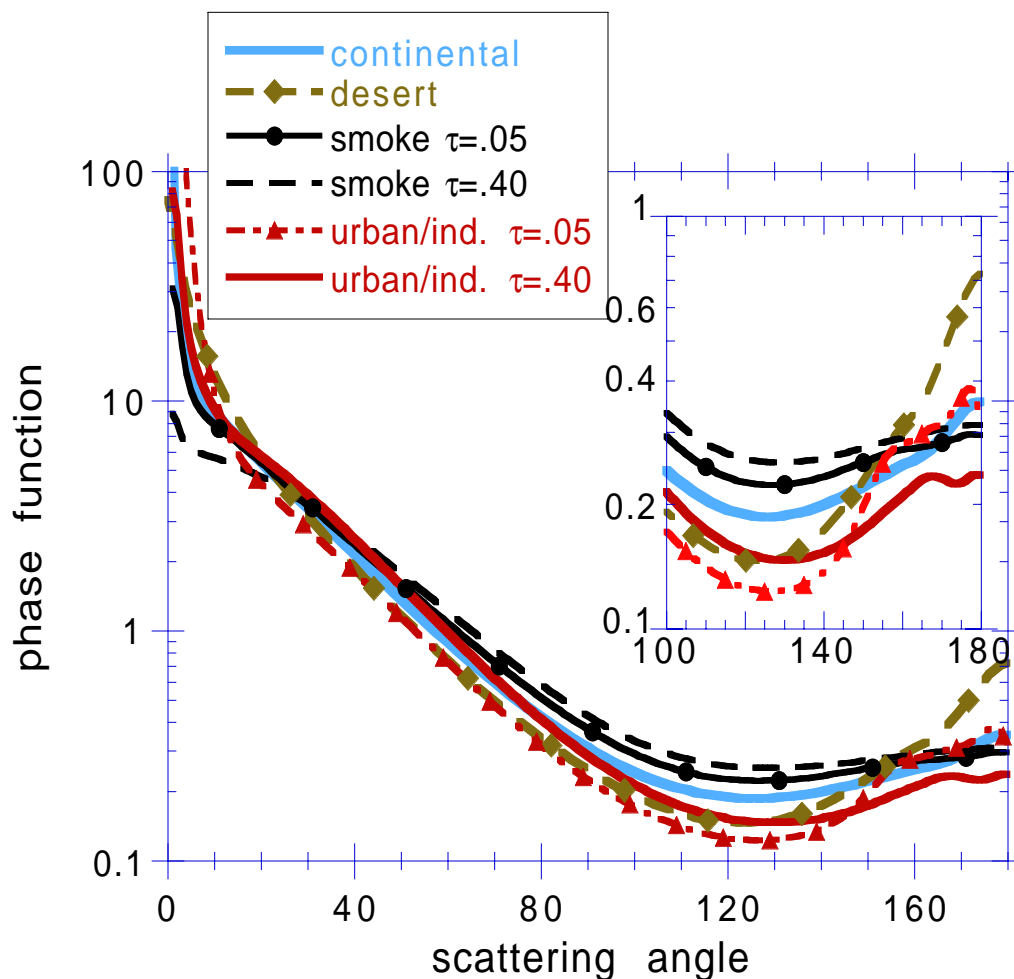
Figure 17. The scattering phase function for 3 aerosol models, continental (Lenoble and Brogniez, 1984), smoke aerosol from biomass burning (Kaufman and Holben. 1996; Remer et al.,

1996), and urban/industrial aerosol measured in the SCAR-A experiment (Remer et al., 1996). The latest two models are given for 2 aerosol optical thickness, excluding the effects of stratospheric aerosol.

4.5 Uncertainty

The main source of errors in the derived aerosol optical thickness are uncertainties in the surface reflectance and in the aerosol model (particle size, refractive index, single scattering albedo and sphericity). From theoretical considerations (Kaufman and Sendra, 1988) and empirical verifications (Fraser et al., 1984; King et al., 1992; Soufflet et al., 1996), the error is expected to be $\Delta\tau=\pm0.05$ to ±0.1 for small optical thicknesses and increase to 20-30% for high optical thicknesses. In some regions, the error may be larger due to unexpected surface properties, contamination by snow, ice or water, low single scattering albedo and large non-sphericity. These errors are based on control of the surface reflectance within $\Delta\rho=\pm0.005$ for the first two priorities in selecting dark targets, to ±0.01 for the following two, and on a choice of the right aerosol model that describes the range of the aerosol effective radius and single scattering albedo.

4.6 Columnar Aerosol mass, aerosol surface area and radiative forcing

The aerosol optical thickness describes the aerosol optical opacity for direct penetration of solar radiation. It is useful in radiative transfer models to calculate the aerosol direct radiative forcing, and for atmospheric corrections. It can also be inverted to the aerosol mass. The inversion of the measured radiance (or path radiance, after exclusion of surface contribution) to the aerosol optical thickness, the columnar aerosol mass concentration (we refer here to mass for a unit specific weight of the aerosol), particle surface area (important for chemical processes) and the radiative forcing, requires assumptions on the aerosol models and in particular the aerosol size distribution and refractive index. For large particles, it is also influenced by the particle non-sphericity. However, the errors associated with the derivations of the optical thickness from the detected radiance, and the derivation of the aerosol mass and radiative forcing from the optical thickness, are negatively correlated. Therefore the total error in the final product (e.g., radiative forcing) should be smaller than expected from the sum of the errors in each individual steps. Boucher and Anderson (1995) developed this approach in the evaluation of the aerosol radiative forcing of climate. Similar approach is being developed for remote sensing of aerosol and their forcing. The effect of the uncertainty in particle size on remote sensing may also depend on the scattering angle between the solar rays and the satellite observation (Koepke and Quenzel, 1979; Husar, private communication, 1996). Therefore, some scattering angles may be preferential for some applications. Figures 18-20 are used to explore these ideas. In these figures, the ratio of the aerosol single scattering path radiance to the aerosol optical thickness (Fig. 18), to the aerosol mass concentration and particle surface area (Fig. 19) and to the radiative forcing (Fig. 20) are plotted as a function of the aerosol effective radius for a log-normal distribution with a standard deviation (of the natural logarithm of the particle size) $\sigma=0.6$. The calculations are for 3 refractive indices (1.40,

1.45 and 1.50 with imaginary part of 0.0035) and selected scattering angles, that represent the optimum choice of the scattering angle.

For remote sensing of the accumulation mode aerosol (effective radius between 0.1 and 0.5), the optimum derivation of optical thickness is for scattering angles of 140° to 160° (depending on the possible range of the particle size), with an anticipated error due to uncertainties in the particle size and refractive index of ±20% to ±40% (Fig. 18). The remote sensing of the columnar mass concentration is expected to be more accurate for the accumulation mode (R<0.5 μm), and it is also best for scattering angles of 120° to 150° with uncertainties from particle size of ±10% to ±30%, and ±30% of the refractive index. (Fig. 19 shows the results for scattering angle of 150° as an example).
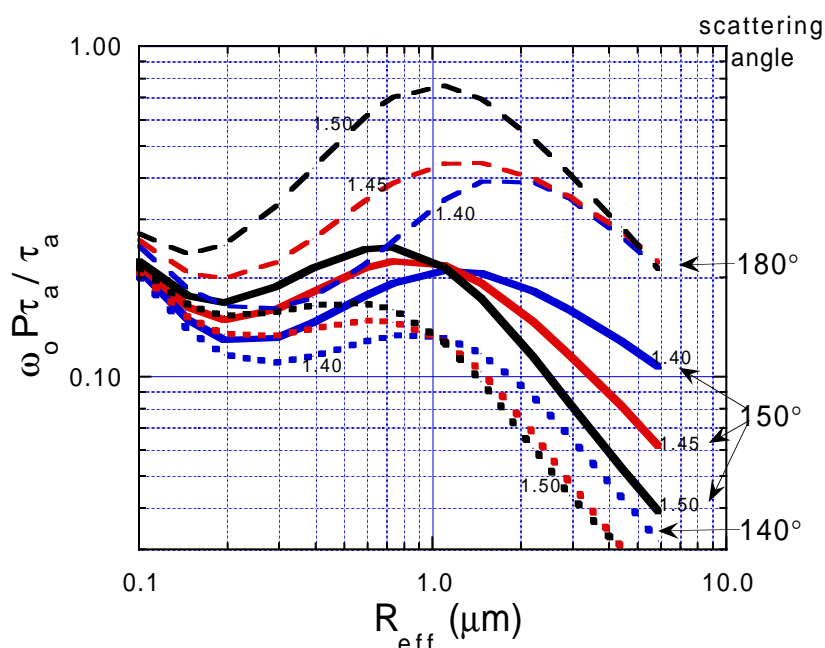

Figure 18. The effect of particle size on remote sensing of optical thickness. The ratio of the path radiance ($\omega P\tau$) to the optical thickness (τ) plotted as a function of the effective radius, for 3 scattering angles (indicated on the right side of the figure) and 3 refractive indices (1.40, 1.45 and 1.50, indicated for most of the graphs). For scattering angle of 150° the variation with R_{eff} is minimal between 0.1 and 1.5 μm (value 0.13-0.24), though for 140° it is more linear in a narrower radius range: 0.15-0.7 μm (value 0.11-0.16).

The particle surface area can be sensed for the coarse mode with an error of 30-50% depending on the refractive index, which is about equal to the error in the optical thickness. For scattering angle of 140° and for particle sizes between 0.1 and 1.0 μm radius, the error introduced in remote sensing of the radiative forcing is only ±20% (Fig. 20). This higher accuracy of the derived aerosol direct forcing from MODIS, than the optical thickness, is an important finding. It is a result of the similar physics in the radiance measured from space above dark surfaces and the reflection by aerosol of the solar irradiances. The derivation of the aerosol properties for a specific scattering angle will also result in a better precision, due to elimination of part of the variability in the

uncertainty of scattering phase function. The use of dynamic aerosol models (described earlier) is expected to reduce these errors furthermore, by limiting the effect of the uncertainty in the particle size.
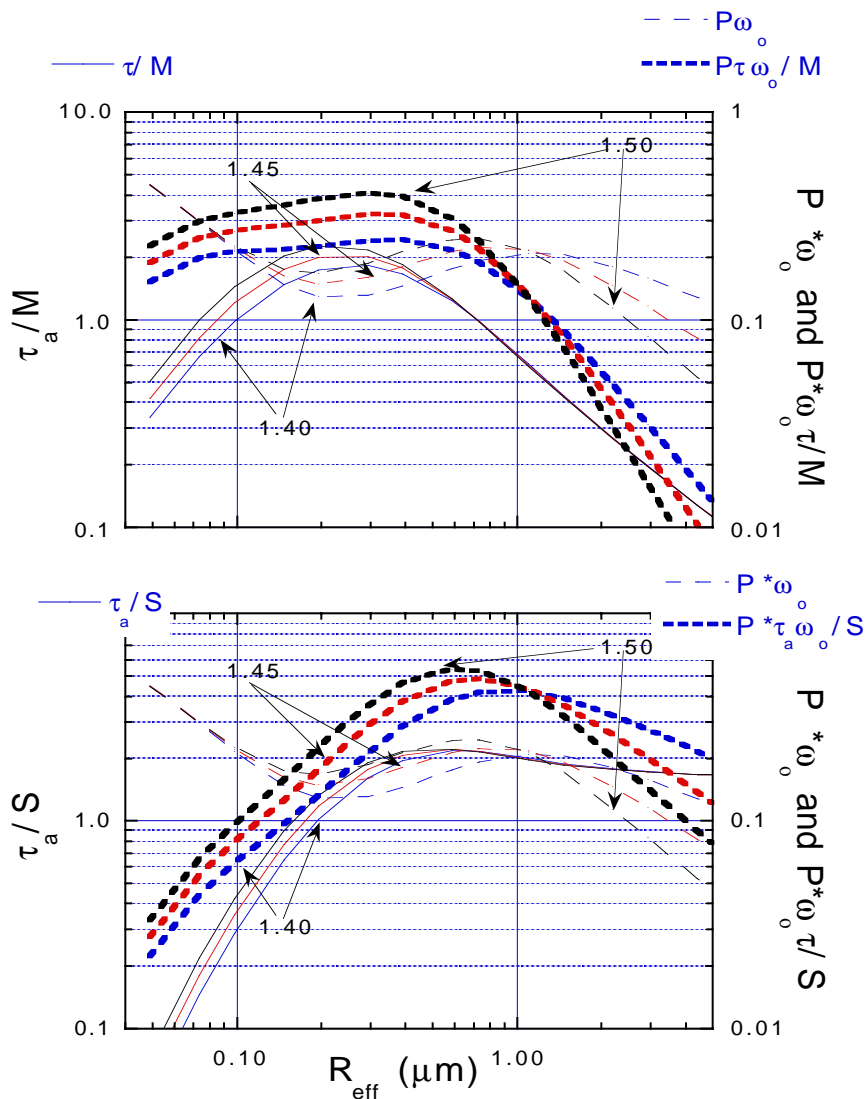

Figure 19. The effect of particle size on remote sensing of the aerosol mass. Aerosol mass sensitivity is given by: $L_{path}/M = P\omega_0\tau/M$. Results are shown for scattering angle of 150°, which was found to be optimum. Here this function as well as $P\omega_0$ and τ/M separately are plotted as a function of R_{eff}. The refractive index is given for most graphs. For refractive index of 1.40 the dependence on R_{eff} is small between R_{eff}=0.1 and 0.5 μm. For larger refractive index the dependence is significantly larger. And the ratio L_{path}/M depends strongly on the refractive index. Therefore conversion of MODIS τ to mass will depend on reasonable knowledge of the refractive index.
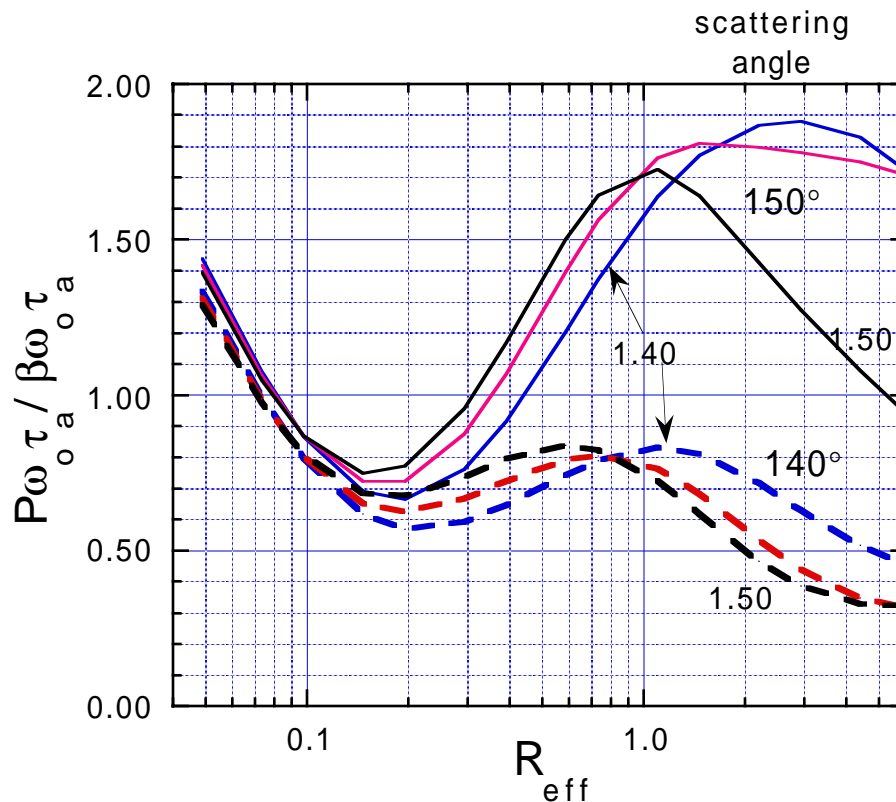
Figure 20. The effect of particle size on remote sensing of radiative forcing, given by the ratio of the path radiance to the average radiative flux. For scattering angle of 140° (dashed lines) the dependence on the particle size is smaller than for 150° (solid lines). For particle size between 0.1 and 1 μm the ratio between the aerosol path radiance and the radiative flux vary around 0.7±0.15 for scattering angle of 140°. Refractive index is shown for most graphs.

In order to use this error reduction associated with selecting specific viewing directions, we anticipate to group the aerosol products for a resolution of 0.5° (in equal angle and area) for periods of time of 8 days and a month, which is defined as level 3 products. Both arithmetic averages and scattering angle weighted averages are planned. This is in addition to a level 2 10x10 km resolution (at nadir) daily aerosol product. The details of the level 2 and level 3 products will be shown in section 7. Information on winds generated by the global circulation models, that are based on radiosonde measurements will be also stored and averaged, weighting by the aerosol concentration, in order to derive the aerosol fluxes (e.g., Fraser et al., 1984). Figure 21 shows the latitude coverage for which scattering angles of 150° can be derived, as a function of calendar month.
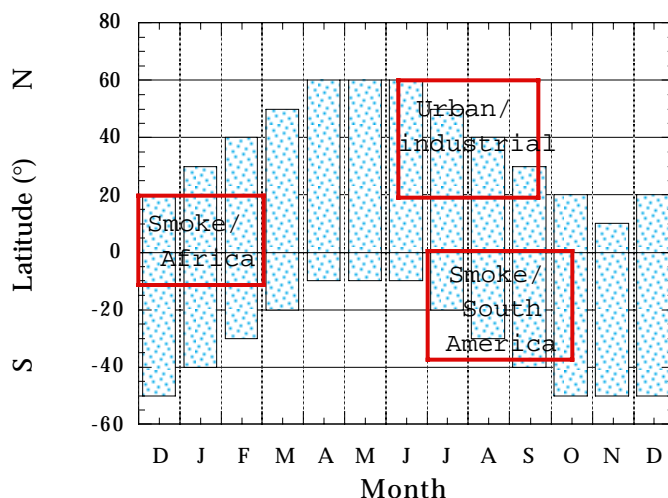
Figure 21. The range of latitude bands for which the scattering angle range reaches 150°, as a function of the month.

5. APPLICATION, VALIDATION AND QUALITY ASSURANCE

5.1 Ocean

The algorithm has been applied to Thematic Mapper (TM) data from Landsat 5 which has similar VIS, NIR and SWIR spectral bands to MODIS (except band at 1.24 μm). It is also applied to the MODIS Airborne Simulator (MAS) data for the best test of the algorithm. Three types of aerosols have been considered: (1) mineral dust coming from Africa, (2) industrial/urban aerosol plumes and (3) smoke plumes resulting from logging waste fires.

Dust over the Tropical Atlantic Ocean near the Senegal coast.

Two field campaigns have been conducted in M'Bour, 80 km south of Dakar, Sénégal in 1986 and 1987. Ground-based measurements, including spectral optical thickness, aureole and downward sky radiances, have been performed (Tanré et al., 1988b). Four TM image data that correspond to the time of the ground based measurements were acquired (Tanré et al., 1988a), one in 1986 on April 30th and three in 1987, on April 1st, 17th and May 3rd. Different dust loading conditions were observed with aerosol optical thickness at 550 nm varying between 0.55 and 2.40 (see Table 8-a). The larger values of the optical thickness were due to higher concentration of large dust particles (Tanré et al., 1988b; d'Almeida, 1987). The TM reflectances computed for 10 different locations, with a box size of 10x10 pixels of 1 km resolution, are reported in Table 8-b. The location were chosen several kilometers away from the coast to avoid adjacency effects as well as oceanic turbidity (see Fig. 22). The uniformity

of the aerosol layer on 04/30/86 is confirmed by the small standard deviation. Although the variability is larger for the other days but it still remains in an acceptable range. The values at 470 nm are also provided though they are not used in the inversion. As expected, the reflectances are increasing as a function of the optical thickness. Note the flatter spectral dependence observed on 04/17/87 is due to the presence of dust plume with the largest particles.

Table 8-a. Aerosol optical thickness measured at 550 nm in M'Bour during the field experiments in 1986 and 1987.

Days	Ground-based optical thickness (550 nm).
04/30/86	0.55
04/01/87	1.47
04/17/87	2.40
05/03/87	0.84

Table 8-b. Mean reflectances expressed in % and standard deviations in the thematic Mapper solar spectral bands over the Tropical Atlantic Ocean close to the Sénégal sea-shore; the average is performed over 10 oceanic targets whose the size is 10x10 pixels (300 m x 300 m).

TM Band	Mean Refl. and stand. dev. (04/30/86)	Mean Refl. and stand. dev. (04/01/87)	Mean Refl. and stand. dev. (04/17/87)	Mean Refl. and stand. dev. (05/03/87)
470nm	11.78±0.11	16.26±0.49	18.96±0.08	13.84±0.10
550nm	8.35±0.16	13.52±0.58	19.55±0.22	10.34±0.21
650nm	6.54±0.10	12.48±0.51	20.84±0.24	8.87±0.17
865nm	5.21±0.09	11.24±0.51	21.61±0.32	8.03±0.29
1600nm	2.69±0.07	6.86±0.32	16.67±0.32	4.10±0.14
2200nm	1.95±0.04	5.54±0.28	15.18±0.30	3.20±0.09

Results of the inversion are reported in Table 9-a for the 'best' model and in Table 9-b for the 'average' model. The 'average' values have been computed according to the method discussed earlier. In cases for which the ε_{min} value for the 'best' model is larger than 3%, the average is computed over the 5 best solutions with ε_{max} kept smaller than 10%. The optical thickness values retrieved from the 'best' model (Table 9-a) are in a remarkably good agreement with the ground-based measurements when values of ε_{min} are small (e.g., on 04/01/87). For the cases of 04/30/86 and 03/05/87, the results are also close to the ground measurements
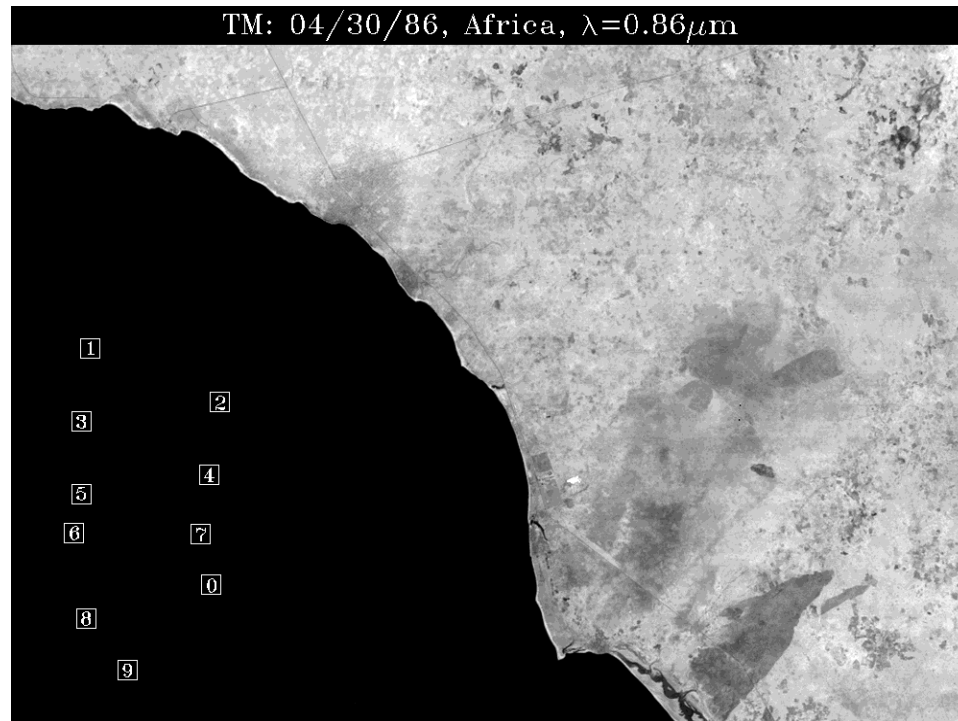
Figure 22. TM image on day 04/30/86 in Band 4 (865 nm) over the Tropical Atlantic Ocean, near the Sénégal coast, showing the locations of the 10 targets.

Table 9-a. Aerosols parameters retrieved from the 'best' aerosol model for the four TM images acquired over the Tropical Atlantic Ocean.

Days	$\tau^m(550nm)$	$\tau^r(550nm)$	r_{eff}	g	η	ε_{min} (%)
04/30/86	0.55	0.66	0.29	0.73	0.62	6.1
05/03/87	0.84	1.08	0.39	0.73	0.42	7.3
04/01/87	1.47	1.51	0.51	0.74	0.25	1.3
04/17/87	2.40	3.36	0.98	0.76	0.00	4.2

Table 9-b. Aerosols parameters retrieved from the 'average' aerosol model for the four TM images acquired over the Tropical Atlantic Ocean.

Days	$\tau^m(550nm)$	$\tau^r(550nm)$	r_{eff}	g	η	ε_{max} (%)
04/30/86	0.55	0.61±0.08	0.26±0.04	0.69±0.04	0.61±0.08	8.8
05/03/87	0.84	1.02±0.13	0.31±0.10	0.70±0.03	0.32±0.15	9.9
04/01/87	1.47	1.43±0.06	0.35±0.15	0.71±0.02	0.15±0.06	3.0
04/17/87	2.40	3.36±0.00	0.98±0.00	0.76±0.00	0.00±0.00	4.2

However, it is clear that since the LUT doesn't include the most suitable aerosol models for these days, fairly large values of ε_{min} are obtained The results for 04/17/87 show the largest discrepancy compared to the other days. That's because the present LUT doesn't include optical thickness greater than 2.0 and extrapolation of the optical thickness is performed. For other aerosol parameters, we don't have ground based measurements for validating the results but in general the behavior is as what is expected, i.e., particles are bigger for larger optical thickness and the largest for 4/17/87 with the dust plumes. The ratio between small and large modes and the asymmetry factor have the right tendency in terms of the optical thickness. Shettle (1984), for instance, suggested the values of 0.70 and 0.87 for asymmetry parameter for Background Desert and Desert Dust Storm models. These values are well compared with 0.69 and 0.76 retrieved for the clearest and haziest days from our retrievals. Note that the temporal evolution of the aerosols sizes retrieved from the TM images was confirmed by the aureole measurements performed during the same time. The results of the 'average' solution (see Table 9-b) confirm the results from the sensitivity study that when the aerosol optical thickness and asymmetry parameter display small standard deviation and at the same time the values of r_{eff} and η are more variable, they are less reliable. Again, optical thicknesses retrieved on 04/17/87 are not significant since the retrieved values are over the limits of the present LUT.

Sulfate aerosols over the Atlantic Ocean near the U. S. East coast.

The Sulfate Cloud and Radiation experiment - Atlantic (SCAR-A) was conducted in July 1993 in the Eastern United States Atlantic region. It was designed to measure the properties of urban and industrial pollution dominated by sulfate particles (Remer et al., 1996). The SCAR-A experiment involved a full integration of the operations of the AErosol RObotic NETwork (AERONET), a field network of sun-sky radiometers (Holben et al., 1996), an instrumental C-131A aircraft with in situ and radiometric measurements (Hegg et al., 1995) and the NASA ER-2 aircraft onboard the MODIS Airborne Simulator (MAS) and the Airborne Visible Infrared Imaging Spectrometer (AVIRIS). The measurements were conducted in both clear and hazy conditions, and in the presence and absence of clouds. During the period, measurements from AVHRR and TM instruments were also acquired.

The AERONET sunphotometers were set up along the Atlantic coast, with one at Wallops (N37°56', W75°28') and one at Hog Island (N37°25',W75°42'). Figure 23 shows the locations of the sunphotometers and the locations of seven oceanic zones selected for analysis. The TM data used has been adjusted according to the MODIS resolutions within a box size of 10 km x 10 km. Zones 1, 6, 3 and 7 are on a line parallel to the sea shore, 50 km off the coast. Zones 2 and 4 are also on a line parallel to the coast but a little closer, around 15-20 km from the coast. Zone 5 is within the Chesapeake Bay. The mean TM reflectances and standard deviations computed over the 7 zones are reported in Table 10-a for 07/12/93 and in Table 10-b for 07/28/93.
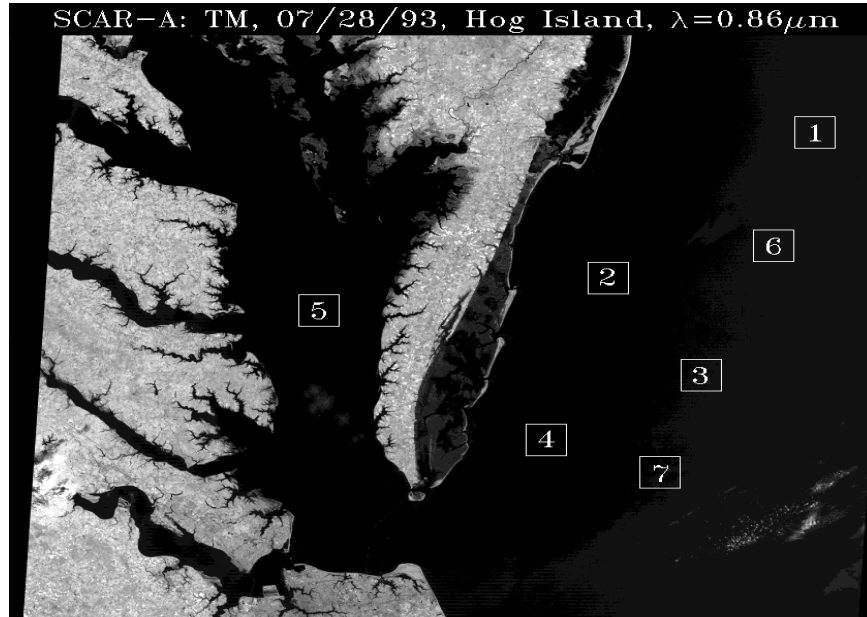
Figure 23. TM image on 07/28/93 in Band 4 (865 nm) over the Atlantic Ocean, near the United States Eastern seaboard, showing the locations of the sunphotometers and the locations of the seven selected zones.

The spectral reflectances for zones 2, 4 and 5 clearly show a rather strange behavior on both days. After subtracting the molecular components in each band, we plotted the reflectances, normalized at 865 nm, as a function of the wavelength in Fig. 24-a for 07/12/93 and in Fig. 24-b for 07/28/93. If the large values of the normalized reflectance obtained at 0.55 and 0.67 µm can be explained by a larger water turbidity expected near the coast, we have no explanation for the small values observed at 1.64 and 2.13 µm over these 3 zones for both days. It could be also due to instrumental problems, because of adjacent bright coast that the instrument may have difficulty recovering from the large values over the land and therefore resulting in an undershoot. Calibration is definitively an issue due to the slightly negative values derived (e.g., on 07/28/93), but it cannot be the only explanation. Good spatial uniformity of the aerosol layer on 07/12/93 should result in reflectances over zones 2 and 4 to be comparable to the reflectances over zones 1, 6, 3 and 7 at 1.64 and 2.13 µm.

Table 10-a. Mean reflectances expressed in % and standard deviations in the thematic Mapper solar spectral bands during the SCAR-A experiment on 07/12/93; the average is performed over boxes whose the size is 10 km x 10 km.

Bands	Zone1	Zone2	Zone3	Zone4	Zone5	Zone6	Zone7
550nm	7.87±0.13	7.16±0.13	6.99±0.13	7.01±0.16	7.74±0.17	7.43±0.14	6.64±0.14
650nm	6.29±0.12	5. 43±0.12	5.50±0.07	5.10±0.13	5.51±0.08	5.91±0.13	5.13±0.14
865nm	5.31±0.19	4.01±0.19	4.47±0.10	3.55±0.19	3.39±0.11	4.96±0.17	4.14±0.13
1600nm	3.01±0.11	1.52±0.13	2.33±0.08	1.21±0.18	0.91±0.08	2.76±0.07	2.16±0.07
2200nm	1.97±0.11	0.68±0.15	1.41±0.15	0.37±0.19	0.06±0.06	1.78±0.16	1.32±0.07

<u>Table 10-b.</u> Mean reflectances expressed in % and standard deviations in the thematic Mapper solar spectral bands during the SCAR-A experiment on 07/28/93; the average is performed over boxes whose the size is 10 km x 10 km. [1] Because of calibration, the reflectances over these targets were slightly negative and were put equal to 0.001

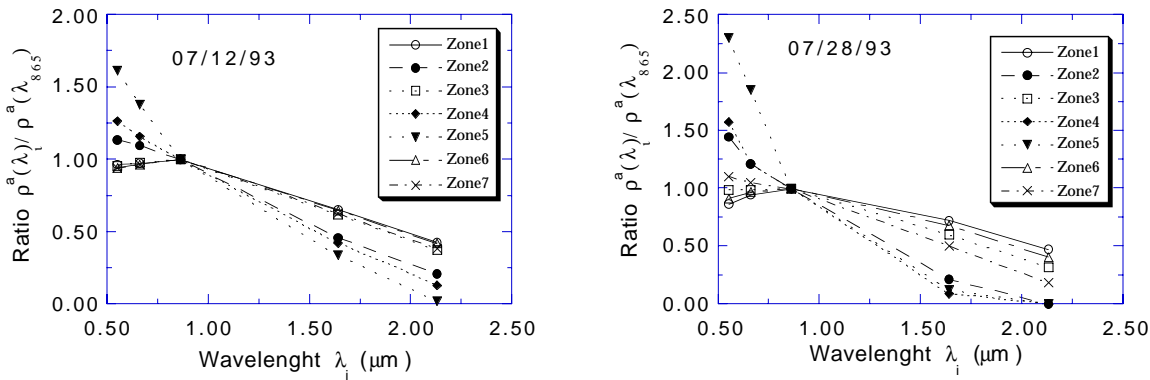| Bands	Zone1	Zone2	Zone3	Zone4	Zone5	Zone6	Zone7
550nm	5.66±0.06	4.76±0.11	5.62±0.17	4.80±0.05	5.45±0.13	5.63±0.11	5.72±0.18
650nm	4.26±0.10	2.94±0.22	4.02±0.14	2.88±0.14	3.45±0.05	4.16±0.12	4.01±0.16
865nm	3.31±0.16	1.64±0.26	2.94±0.18	1.59±0.19	1.59±0.09	3.14±0.17	2.80±0.20
1600nm	1.89±0.11	0.20±0.22	1.34±0.13	0.08±0.12	0.12±0.10	1.66±0.11	1.06±0.11
2200nm	1.25±0.13	0.001[1]	0.71±0.13	0.001[1]	0.001[1]	1.00±0.10	0.39±0.12

<u>Figure 24-a and b.</u> TM reflectances, normalized at 865nm, as a function of the wavelength for the 7 zones on 07/12/93 (a; left panel) and for 7/28/93 (b; right panel).

The retrieved aerosol parameters are reported in Table 11-a for the 'best' solution and in Table 11-b for the average over the 5 best solutions. Table 11-a reflects also the same problem regarding for zones 2, 4 and 5. On 07/28/93 for these zones we even cannot invert data, and on 07/12/93, very large values of ε_{min} proves that the results are not significant. Nevertheless, if we limit our analysis to zones 1, 6, 3 and 7, the ground-based measured and the algorithm retrieved optical thicknesses show a good comparison. It is even better for the 'average' solutions. Again, ε_{min} value is a good indicator of the quality of the inversion. The effective radiuses retrieved for both modes are quite stable for the 4 zones, ranging 0.11-0.18 for the small modes and 0.90-2.00 for the large modes (Table 11-b). In comparison, the measurements of AERONET instrumentation showed effective radius of the accumulation mode in the range 0.16-0.18 (or 0.11-0.16 in the present analysis) on July 12, and 0.12-0.13 (or 0.11-0.18 in the present analysis) on July 28, 1993. The urban/industrial aerosol dynamic model

(Remer et al., 1996a, 1996b) identifies accumulation mode particle sizes between 0.09 for very clear conditions to 0.19 μm in hazy conditions, as well as a maritime coarse mode particle at 1.2 μm.

On 07/12/93, in particular, the latitudinal gradient of η between the southern and northern zones is anti-correlated with the optical thickness for both the 'best' and the 'average' solutions, i.e., η=0.73 and τ=0.48 relative to η=0.47 and τ=0.62 (the 'best' solution); η=0.67 and τ=0.46 to η=0.29 to τ=0.53 (the 'average' solution). Although these results are in agreement with Remer et al. (1996a), the present accuracy of our retrieval is not sufficient for making a definitive statement.

The algorithm was further validated for this type of aerosol in this geographical region using similar data from the TARFOX experiment in 1996. Results are presented in Tanré et al. (1999).

Table 11-a. Aerosols parameters retrieved from the 'best' aerosol model for the two TM images acquired during the SCAR-A experiment.

Days	τ^m(550nm)(Wallops)	τ^m(550nm) (Hog Island)	τ^r(550nm)	r_{eff}	g	η	ε_{min} (%)
07/12/93	0.60±0.04	0.57±0.04	0.62 (Zone 1)	0.36	0.73	0.47	8.9
			0.57 (Zone 6)	0.34	0.73	0.50	10.0
			0.55 (Zone 3)	0.26	0.73	0.71	12.8
			0.48 (Zone 7)	0.26	0.72	0.73	12.9
			0.42 (Zone 2)	0.12	0.57	1.00	22.0
			0.33 (Zone 4)	0.12	0.57	1.00	31.6
			0.27 (Zone 5)	0.06	0.27	1.00	51.9
07/28/93	0.20±0.02	0.21±0.01	0.26 (Zone 1)	0.35	0.73	0.28	10.5
			0.30 (Zone 6)	0.21	0.72	0.89	13.8
			0.21 (Zone 3)	0.12	0.57	1.00	18.3
			0.18 (Zone 7)	0.12	0.57	1.00	29.0
			N/A (Zone 2)	/	/	/	/
			N/A (Zone 4)	/	/	/	/
			N/A (Zone 5)	/	/	/	/

Table 11-b. Aerosols parameters retrieved from 'average' solution (average of top 5 'best' aerosol model) for the two TM images acquired during the SCAR-A experiment.

	τ^r(550nm)	r^s_{eff}	r^l_{eff}	r_{eff}	η	ε_{min}
07/12/93						

	r^s_{eff}	r^l_{eff}	r_{eff}	g	τ	ε (%)
Zone 1	0.53±0.05	0.11±0.06	0.90±0.00	0.26±0.08	0.24±0.15	10.0
Zone 6	0.52±0.08	0.13±0.05	0.92±0.05	0.28±0.08	0.36±0.19	12.0
Zone 3	0.52±0.10	0.16±0.05	1.04±0.26	0.23±0.03	0.66±0.21	15.0
Zone 7	0.46±0.09	0.16±0.05	1.04±0.26	0.23±0.03	0.67±0.22	15.0
07/28/93						
Zone 1	0.22±0.02	0.11±0.06	0.90±0.00	0.32±0.05	0.21±0.18	11.0
Zone 6	0.30±0.05	0.18±0.04	1.46±0.09	0.20±0.01	0.89±0.17	14.0
Zone 3	0.21±0.00	0.12±0.06	2.28±1.74	0.12±0.00	1.00±0.00	18.0
Zone 7	0.18±0.00	0.12±0.00	2.28±1.74	0.12±0.00	1.00±0.00	29.0

Smoke over Pacific Ocean near the U. S. West coast.

The Smoke Cloud and Radiation experiment - California (SCAR-C) was conducted in September, 1994 in the Pacific Northwest. It was designed to measure the entire process of biomass burning, including ground-based estimates of fuel consumption, airborne sampling of the smoke aerosol and trace gases, and airborne and spaceborne remote sensing of fires and smoke (Kaufman et al., 1996). Remote sensing images of fires and smoke were taken by MAS and AVIRIS flown on ER-2 aircraft. We analyze the MAS data for the Quinault prescribed fire in Washington state using the observations performed from the ER-2 at 20:30:54 GMT. The fire was lit very close to the sea shore, with wind transporting the smoke over the ocean. The fuel of this prescribed fire consisted of old-growth large western red cedar debris left over logging (Hobbs et al., 1996).

Results are reported in Table 12 as a function of the distance from the fire. Note that for the prevailing wind of 7 m/s, smoke measured 25 km off shore represent smoke that is one hour old, emitted from the fire one hour earlier than the smoke observed close to the fire. The smoke plume shown in Fig. 25 is narrow and non-homogeneous. Therefore application of the present algorithm may be limited by the assumption of a plane parallel atmosphere used in the generation of the look-up tables. Limitations in the calibration accuracy prohibited us to use the 1.64 and 2.13 μm channels. In these channels, the smoke is very transparent with a very weak backscattered signal. Therefore, small calibration errors could induce even negative values of the upward radiance in these channels.

Table 12. Aerosols parameters retrieved from the 5 'best' aerosol model for the MAS data acquired during the SCAR-C experiment.

Dist. (km)	r^s_{eff}	r^l_{eff}	r_{eff}	g	τ	η	ε (%)

5	0.06±0.00	2.48±1.68	0.082±0.028	0.34	2.59±0.14	0.86±0.02	1.0
8	0.06±0.00	2.48±1.68	0.067±0.011	0.30	2.12±0.04	0.95±0.01	1.2
16	0.06±0.00	2.48±1.68	0.060±0.000	0.27	1.55±0.00	1.00±0.00	3.2
20	0.06±0.00	2.48±1.68	0.060±0.000	0.27	1.07±0.00	1.00±0.00	5.4
28	0.06±0.00	2.48±1.68	0.060±0.000	0.27	1.10±0.00	1.00±0.00	7.0
36	0.06±0.00	2.48±1.68	0.060±0.000	0.27	1.05±0.00	1.00±0.00	9.8
44	0.06±0.00	2.48±1.68	0.060±0.000	0.27	1.34±0.00	1.00±0.00	3.5
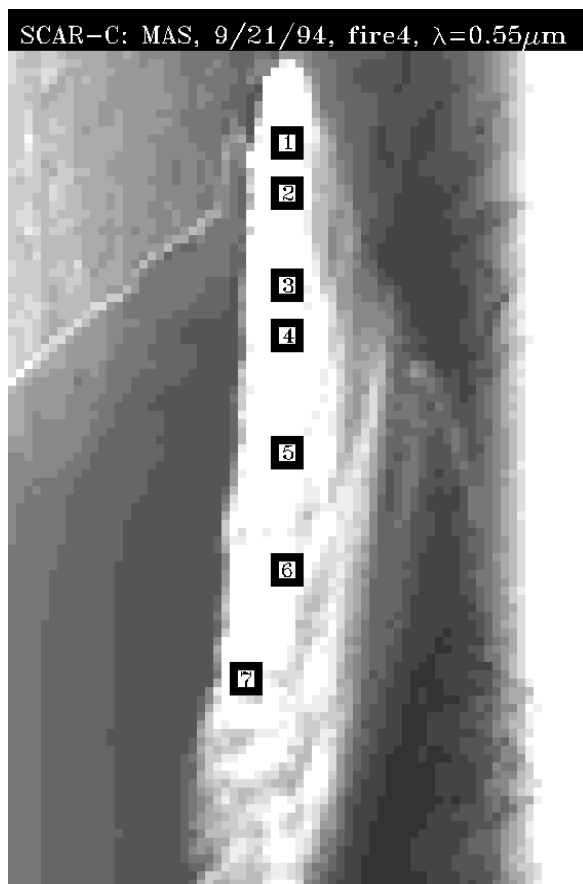
Figure 25. MAS image on 09/21/94 at 550 nm over the Pacific Ocean near the United States western seaboard showing the locations of the seven zones within the smoke plume.

The results show a very stable small particle mode with r_{eff}=0.06 μm, and a coarse particle mode with r_{eff}=2.5 μm, that disappeared 16 km (or 40 minutes) from the shore. Measurements of the particle size distributions from collections on nucleopore filters show that the accumulation mode particle size distribution vary from 0.06 μm in radius for flaming conditions close to the fire to 0.14 μm for a mixed 2 hours old smoke (Martins et al., 1996). Large coarse particles were also observed in flaming conditions close to the fire. Hobbs et al (1996) analyzed the in situ measurements of the size distribution of aerosol particles in these prescribed fires.

From his measurements we can deduce that the particle size decreased from r_{eff}=0.12 μm in the flaming stage to 0.10 μm in the smoldering stage. He also found the particle size to increase from r_{eff}=0.11 μm for fresh flaming aerosol to 0.17 for two hours later. These particle sizes are somewhat larger than the size derived from the remote sensing data, but direct validation of the particle size in the whole vertical column is not available. The finite horizontal dimensions of the smoke plume are expected to affect the longer wavelengths more than the shorter wavelengths due to the spectral variability of the smoke opacity. This may result in artificially smaller particles. In summary, the remote sensing data depicted correctly the reduction in the particle size from the urban/industrial haze aerosol to the smoke aerosol. This reduction is consistent with the dynamic aerosol models for both conditions with r_{eff}=0.19 μm for the urban/industrial haze aerosol in the mid-Atlantic region of the US and 0.11 μm for mixed smoke aerosol in South America (Remer et al., 1996b).

Figure 26 summaries the comparisons of the optical thicknesses derived from TM data and the sumphotometer measurements for west African coast and for US eastern seaboard. For both dust and sulfate aerosols, the results show very good agreement with ground-based sunphotometer observations of the optical thickness ranging from 0.2 to 1.5.
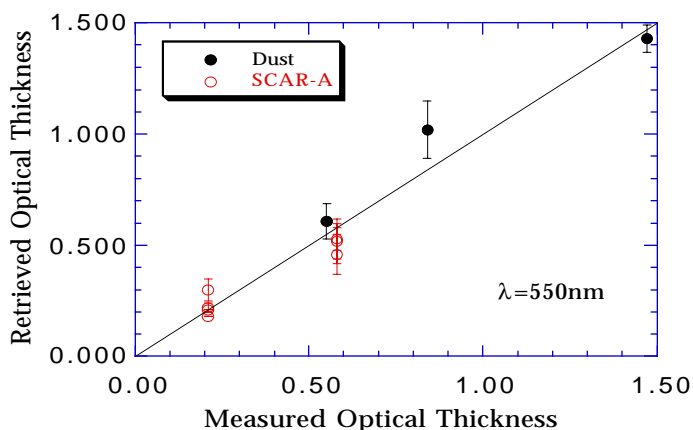

Figure 26. Comparison between the aerosol optical thickness measured at the ground level and the aerosol optical thickness retrieved from TM data for the African and SCAR-A experiments.

5.2 Land

After the launch of MODIS on EOS AM-1 satellite, a continued validation and modification of the algorithms is planned using continuous measurements from the AERONET ground network of sunphotometers/sky radiometers, and in situ

measurements. We expect to have more than 50 instruments operational world wide. They will be located in regions with key aerosol types, or in regions where the aerosol type is expected to vary. This includes islands where ground based in situ aerosol chemical, physical and optical properties are measured (e.g., Prospero and Nees, 1986). The MODIS derived aerosol optical thickness and type will be compared with those measured in these stations. Consistency checks will be performed observing the possible dependence of the optical thickness on the view direction. In addition, the results will be compared with optical thickness generated by other instruments, such as MISR multi-angle instrument also on EOS AM-1 platform and POLDER on ADEOS scheduled to launch in August of 1996. Both POLDER, flown before MODIS, and MISR, flown simultaneously with MODIS, will be differently sensitive to aerosol. POLDER will be sensitive to aerosol polarization, and both sensors will be sensitive to the aerosol angular optical properties. In particular, the MISR multi-angle radiance measurements are planned to be used to estimate the aerosol nonsphericity (Kahn et al., 1996). This information can be used to update the dust aerosol scattering phase function applied to specific geographic locations (e.g., Saharan dust, Gobi desert dust), and used during the time for which the MODIS data are analyzed.

In the last 3 years, an extensive data set was collected during and around the SCAR field experiments. In addition to the SCAR-A experiment that was conducted in the mid-Atlantic region of the United States in 1993 for measuring aerosols dominated by industrial/urban pollution, two additional SCAR experiments were conducted to measure smoke aerosol. The SCAR-C in 1994 in the northwest US for prescribed and wild fires in mid-latitudes and the SCAR-B experiment in Brazil for deforestation and Cerrado fires in the tropics in 1995. The SCAR-B data includes remote sensing measurements from the MODIS airborne simulator (MAS) and AVIRIS spectral imager operated onboard ER-2 aircraft flying at 20 km altitude. In situ aerosol measurements were taken by the instrumented C-131A aircraft of the University of Washington (e.g. Hobbs et al., 1996; Martins, et al., 1996). These data sets and the AERONET measurements are presently being used for extensive validation of the approach.

Application of the remote sensing approach using the MODIS 2.1 μm channel to detect the dark pixels and determine their reflectance is shown in Figs. 27 and 28. In Fig. 27 the aerosol optical thickness is derived from 6 Landsat TM and AVIRIS airborne images collected during the SCAR-A experiment and compared to aerosol optical thickness measured from the ground by the sunphotometer AERONET network. An example of a Landsat image and its analysis is shown in false color, representing the apparent reflectance of the earth-atmosphere system (top panels) and the derived optical thicknesses in the red and blue channels (lower panels) in Fig. 27. It shows an elevated aerosol level, accompanied by moisture and clouds in the upper right and lower part of the image. Higher apparent reflectance and corresponding higher optical thickness are derived. The images were averaged before analysis of the optical thickness to the MODIS resolution. Both the aerosol results initially analyzed using continental model and in the final analysis using appropriate dynamical model are shown in Fig. 27.
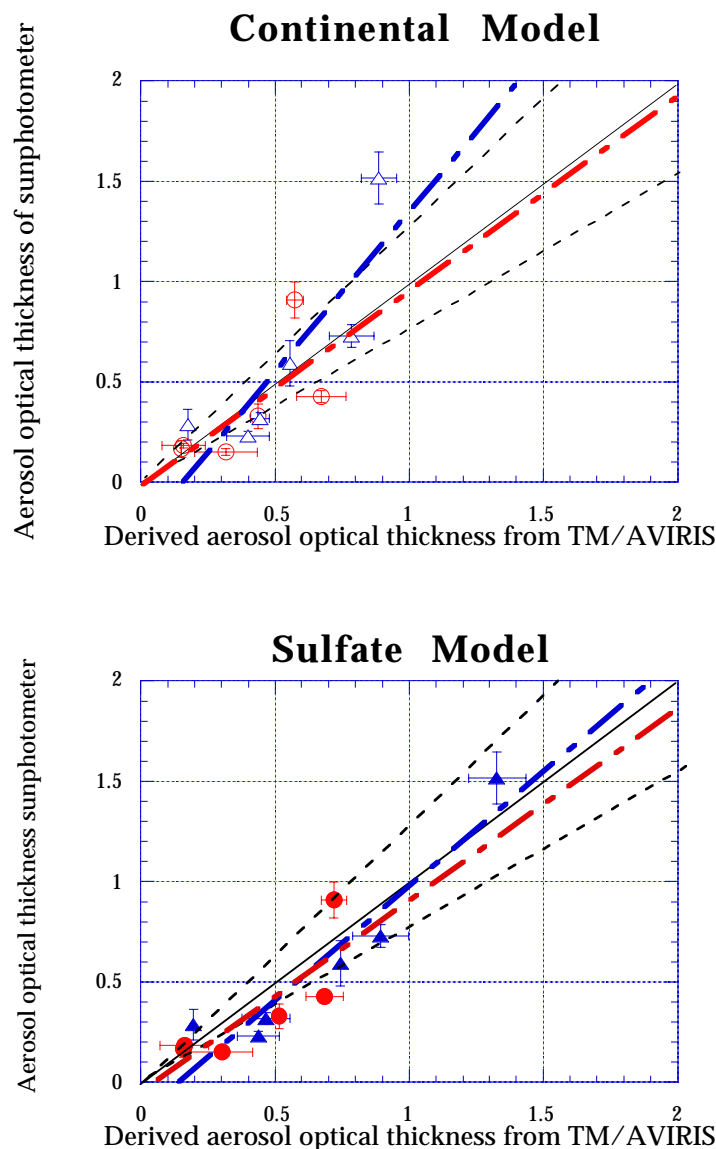
Continental Model

Sulfate Model

Figure 27. Comparison between aerosol optical thickness derived from Landsat TM and AVIRIS data collected during the SCAR-A experiment and aerosol optical thickness measured from the ground by the sunphotometer AERONET network. The Landsat and AVIRIS data were averaged before analysis to the MODIS resolution. Analysis using a continental model and in the final analysis using the appropriate dynamical model are shown. Note that the standard deviations depicted are the temporal variability of the sunphotometer data around the Landsat or ER-2 overpasses (abscissa) and the spatial variability of the optical thickness derived from the TM or AVIRIS data around the sites of sunphotometer (ordinate). The red and blue symbols represent red and blue channels used to retrieve aerosol optical thickness. Different symbols represent different measurements or locations; for example, trangle: TM New Jersey (July 12, 1993); square: TM Hog Island, Virginia (July 28, 1993); left triangle: AVIRIS Hampton Roads, Virginia (July 14, 1993). The solid red and blue lines are the least-squares fit to the data at red and blue wavelength respectively. The dashed lines are the range of the expected accuracy (bias of ±0.05 and an uncertainty in the slope of ±0.2).
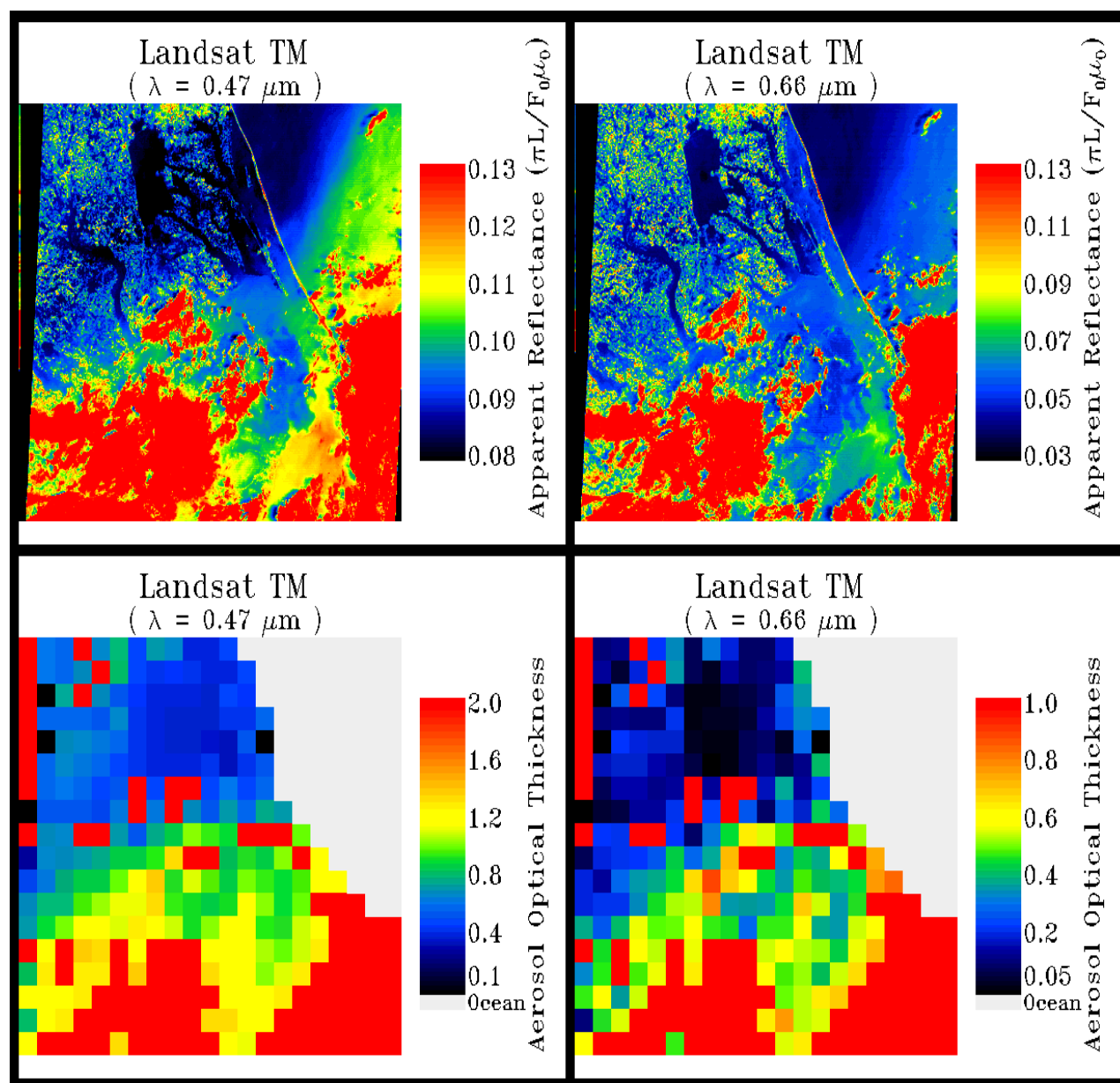
Figure 28. False color Landsat TM image over the North Carolina - Virginia region (July 12, 1993). The apparent reflectance of TM 0.47 μm channel (left) and the 0.66 μm channel (right) are shown in upper panels. The lower panels are the corresponding aerosol optical thickness in the blue and red channels, derived by the MODIS algorithm for the reduced resolution of Landsat image.

In Figure 28, only the final corrected optical thicknesses are shown. The resolution of the optical thickness is a 10x10 km grid box produced by the MODIS aerosol algorithm. Figure 27 shows clearly that the correction of the model is a significant improvement to the optical thickness, especially for high optical thickness. Note that the standard deviations depicted in Fig. 27 are the temporal variability of the sunphotometer data around the Landsat or ER-2 overpasses (abscissa) and the spatial variability of the optical thickness derived from the TM or AVIRIS data around the sites of sunphotometer (ordinate). It includeds results only from criteria 1 and 3 in selecting the dark pixels (3.8 μm channel is not available from TM data). The derived optical thickness using the dynamic aerosol models is within the expected range of uncertainties ($\Delta\tau_a=\pm0.05\pm0.2\tau_a$). An example of the aerosol optical thickness retrieved in the red versus that in the blue channel (after correction) illustrates a good agreement of spatial variation of the results within TM image and temporal variation of sunphotometer observations in New Jersey (see Fig. 29). Lower priority (i.e., wider range of the surface reflectance >0.1) results in much scattered and larger variation. Similar features were also found in the TM images of North Carolina - Virginia regions, indicating small sulfate aerosols with strong spectral dependence (optical thickness ratio of red versus blue=1:2). Between the temporal variation (sunphotometer observations) and spatial variation (TM images), the ratios are closely correlated, leading to a stable aerosol source and a persistent transport mechanism during the summer time of stagnant and humid conditions. However, the ratios used in determining the surface reflectance in the red and blue channels from mid-IR channel was derived mainly using data from SCAR-A experiment. Also, the dynamical aerosol model for industrial/urban aerosol was derived from the SCAR-A measurements. Therefore, the validation of the results (shown in Figs. 27 and 29) was derived in the most favorable conditions

Two independent cases are studied using the same algorithm as used in the most favorable conditions discussed above. The two cases are Landsat TM images near Madison, Wisconsin of June 6, 1995 and Sevilleta, New Mexico of March 17, 1995, one for the urban/industrial aerosol and one for the dust. The results shown in Fig. 30 displays the ratio of mean (including standard deviation) of aerosol optical thickness between the red and the blue channels derived from TM images, and those from the sunphotometer measurements. The mean and standard deviation of TM data are calculated around the sunphotometer sites. The mean and standard deviation of sunphotometer optical thickness are calculated within ±30 minutes from the satellite overpass time. The correction based upon the single scattering approximation and the aerosol type differential criterion are found to be valid for the independent conditions as well. The ratio of optical thickness between red and blue channels of these two cases shows clearly the differences between sulfate and dust, which can be used to distinguish between them.

An application of the MODIS remote sensing technique to South Atlantic region in Brazil and its validation is shown by Vermote et al. (1996). They derived the aerosol
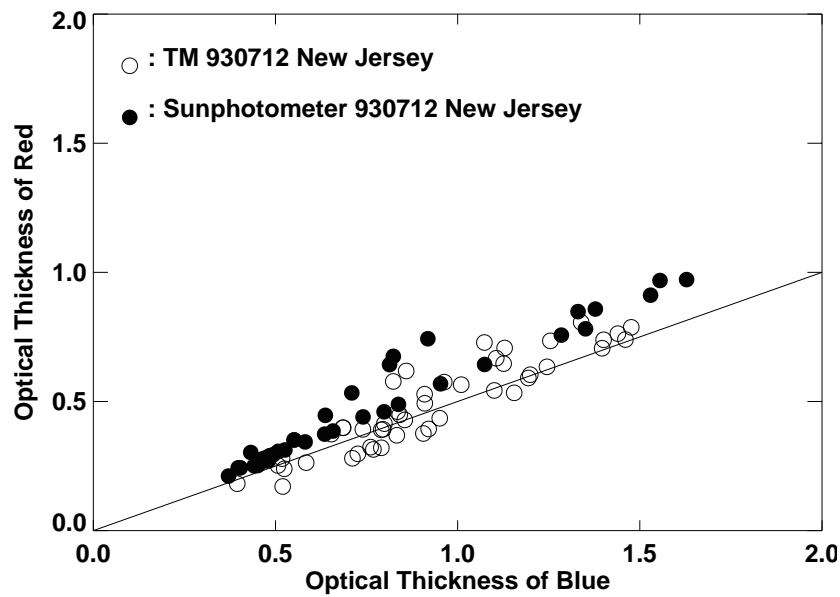
Figure 29. Ratio of aerosol optical thickness retrieved in red versus those retrieved in the blue channels of TM image in New Jersey area (July 12, 1993) and those from sunphotometer observations.
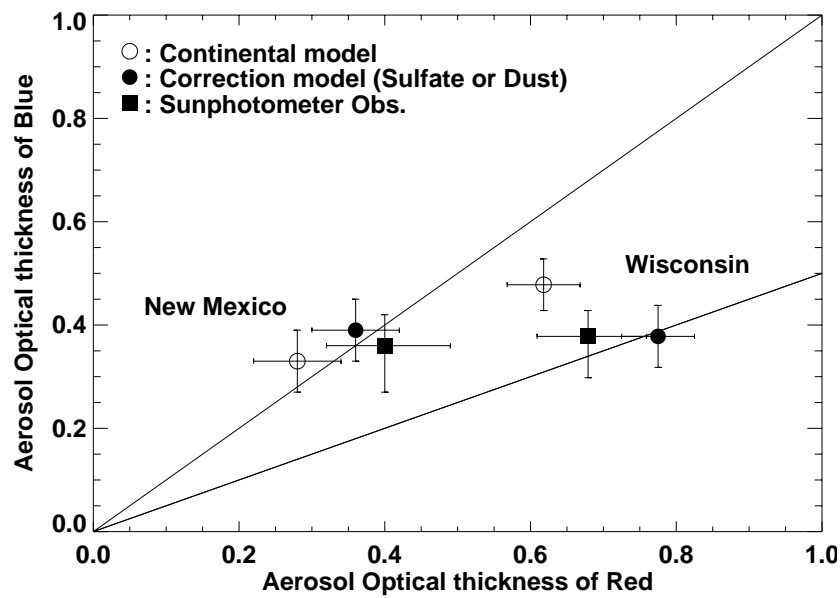

Figure 30. Comparison of mean and standard deviation of aerosol optical thickness retrieved from TM images of Madison Wisconsin (June 6, 1995) and Sevilleta, New Mexico (March 17, 1995) and those obtained from sunphotometer observations.

optical thickness from the AVHRR data using dark targets identified by 3.7 µm channel, and a smoke aerosol model. These results compared against the AERONET measurements of the optical thickness are shown in Fig. 31. One can see that high correlation (correlation coefficient r = 0.933) between the remotely sensed aerosol optical thickness and the ground based measurements is achieved with most values within the expected accuracy (i.e., $\pm 0.05 \pm 0.2\tau$).
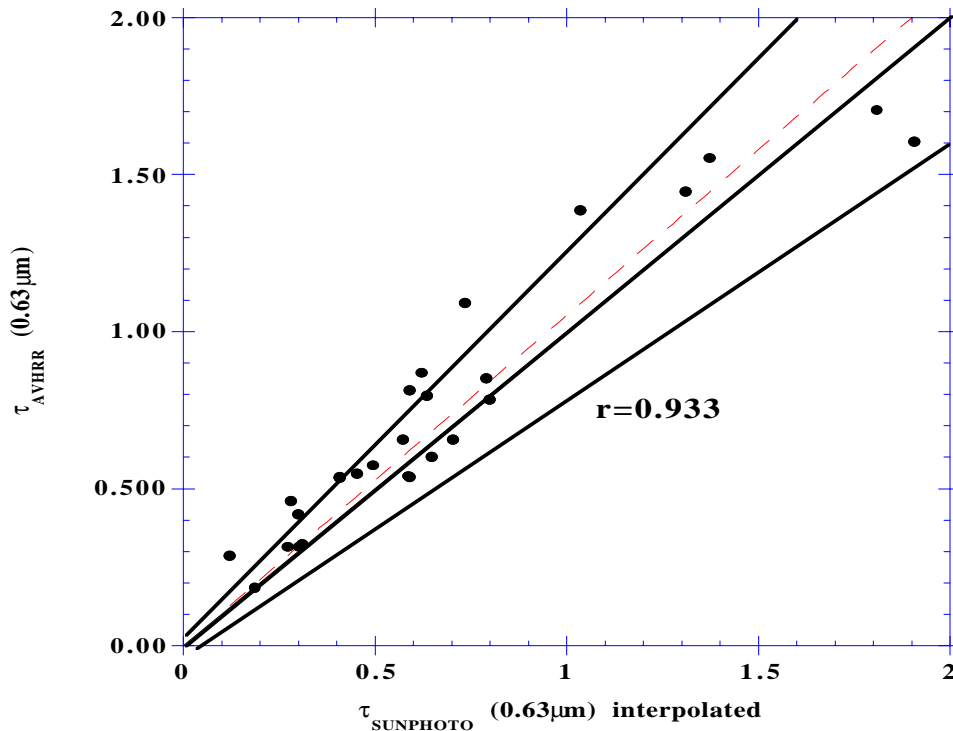

Figure 31. Comparison of retrieved optical depth using AVHRR data and the dark target approach and measured optical depth from the AERONET sun photometer network over Brazil in 1993 (Vermote et al., 1996). The dashed line is the least square fit to the scatter diagram. The solid lines show the range of the expected accuracy of the algorithm. Most points are within the range of expected accuracy. Smoke aerosol model was used in the remote sensing procedure.

5.3 Ocean and Land

Shown in Fig. 32 is an example of combined results of aerosol optical thickness of ocean and land for North Carolina - Virginia case at 0.55 µm. For land, aerosol optical thickness at 0.55 µm is interpolated (in logarithm scale) between 0.47 and 0.66 µm, and for ocean the optical thickness is derived from the aerosol ocean algorithm. The apparent reflectance (upper panel) is shown only for reference over land. Aerosol

optical thickness at 0.55 µm is one of the common products of both ocean and land (see Table 13 for a complete list of level 2 products).

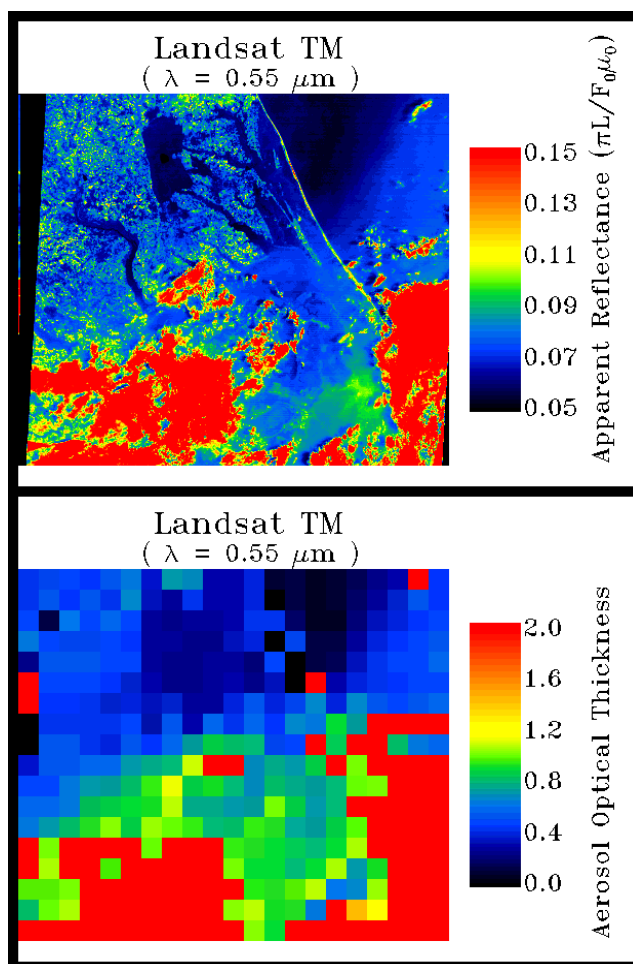
Figure 32. False color Landsat TM image over the North Carolina - Virginia region (July 12, 1993). The apparent reflectance of TM 0.55 µm channel is shown in upper panel. The corresponding aerosol optical thickness derived over both ocean and land is shown in lower panel.

5.4 Future Plans for Validation

Before the launch of MODIS on EOS AM-1 platform, we plan to continue and validate the remote sensing of aerosol over the land and ocean using simulated MODIS data from MAS and other airborne instruments (such as AVIRIS), and the simultaneous measurements of the spectral optical thickness from the AERONET sunphotometry, and in situ measurements of the aerosol size distribution from the C-131A aircraft. Such data over the Amazon basin was acquired in the SCAR-B experiment (1995) and was not analyzed yet. Data are also being acquired over the Atlantic ocean and land in the Tropospheric Aerosol Radiative Forcing Observational Experiment (TARFOX) in July, 1996. It includes ground-based sunphotometer

measurements, shadow-band radiometer measurements and aircraft remote-sensing and in situ measurements involving ER-2 (NASA), C-130 (UK), C-131A (University of Washington) and CIRPAS Pelican (Naval Postgraduate School). Over the ocean, the sunphotometer measurements were also taken on the cruise ship. The primary purpose of TARFOX is to measure aerosol over the ocean, in addition to the SCAR measurements mainly focused on the land.

After the launch of MODIS, we plan to have a continuous monitoring of the aerosol products from MODIS over the AERONET global network (and a similar network planed by T. Nakajima), and through the intercomparisons with other instrument also aboard EOS AM-1, such as MISR, and POLDER on ADEOS satellite. We also plan to monitor the consistency between the land and ocean aerosol products especially in the coastal regions. Two new field programs specific for MODIS validation campaign are planned in August 1999 and in September 2000 for US east coast Mid-Atlantic sulfate aerosol and smoke and fire in US northwest region, respectively. Details can be found in the MODIS science data validation plan for atmosphere in WWW (http://spso.gsfc.nasa.gov/spso_homepage.html).

5.5. Quality Assurance

The aerosol products over the land and ocean will be accompanied with a quality control parameter that will monitor the inversion process. The quality assurance (QA) flag of MODIS aerosol products over land and ocean directly reflects, in a scientific sense, the quality of aerosol parameters retrieved by the algorithms. For aerosol over the land, due to dark target approach, the surface reflectance at 2.1 μm less than 0.05 is considered to be the best for the retrieved aerosol optical thickness since the uncertainty of surface reflectance is the smallest. The quality then decreases for an increase of the surface reflectance. Other elements such as the number of cloud-free pixels in the grid of 10x10 km box and standard deviation calculated using the percentiles are also considered to be part of the quality assurance. The QA flag will be stored on the base of 10x10 km grid which is the resolution of the aerosol optical thickness retrieved in level 2.

Over the ocean, the aerosol parameters derived are grouped in an order of the (least-squares) errors of the radiance (calculated versus measured) in six spectral bands used for all combinations of small and large aerosol modes. Smaller error means better results. The "best" solution corresponds to the smallest error and the "average" solution is the average of the retrieved results with errors less than 3%. Glint contaminated pixels will also affect the quality of the results. Therefore, we shall include the assessment of possible glint contamination in the quality assurance flag for the remote sensing of aerosol over the ocean. In the aerosol ocean algorithm, we also plan to perform the rejection of 25-33%of the brightest and darkest pixels at 865 n m within the 10x10 km box for cloud screening and the exclusion of low reflectance pixels of small signal to noise ratio to maintain the quality of the results.

The equation depicted below shows as an example conceptually how the quality assurance flag is going to be calculated for aerosol product over the land. The quality flag is designed to be a function which is proportional to the number of cloud-free pixels detected, inversely proportional to the rank of the criterion of finding the dark pixels and inversely proportional to the standard deviation versus the mean of aerosol optical thickness calculated. The larger the number the better the quality. The value of QA flag is designed to vary in the range of 0 and 1. The details such as the exponents of α and β are yet not determined.

$$\text{QA} = \left(\frac{N}{N_o}\right)^{\alpha} \left(\frac{1}{P}\right)^{0.5} \left(1 - \frac{\rho_{sd}}{\sqrt{n}\,\rho_{mean}}\right)^{\beta}$$

where N is the number of cloud and water free pixels, N_o the maximum number of pixels in 10x10 km (or 5x5 km) grid box, P the priority used in finding dark pixels in mid-IR channels, ρ_{sd} the standard deviation and ρ_{mean} the mean of apparent reflectance between the designed percentile (i.e., 10 to 40 for normal grid of 10x10 km and 10 to 60 for sub-grid of 5x5 km cases) with n number of points. We anticipate to do similarly for the ocean aerosol products.

6. PROGRAMING CONSIDERATION, INPUT DATA, AND OUTPUT PRODUCTS

6.1 Programming Consideration

The algorithms of aerosol over land and ocean are both using the look-up tables for the retrieval of the aerosol parameters. It is a straightforward approach, therefore the numerical instability is not expected to occur. Also, single precision arrays are sufficiently accurate in the process of input and output, as well as in the numerical operations. In the derivation of aerosol parameters from the look-up tables, no extrapolation is permitted to ensure reasonable physical meaning. The linear interpolation on the look-up table tabulated values shows only 2-3% errors, which is smaller than other uncertainties such as the uncertainty in the surface reflectance (5-20%), the uncertainty in the aerosol model (10-20%) (for aerosol over the land), and the errors due to the glint, the wind speed and the water leaving radiance estimation (for aerosol over the ocean). When no aerosol is retrieved, fill data is written instead to the output. The algorithms are also capable to handle the missing data as well as the bad detectors from level 1B data.

6.2 Input Data

In addition to the MODIS spectral reflectance measurements described for use in retrieving aerosol parameters, other information such as cloud mask, cirrus cloud index, and total water vapor content are also needed in the aerosol retrieval. Although

all MODIS spectral channels used in retrieving aerosol are in atmospheric windows, small absorption due to atmospheric gases still exists and affects the retrieved aerosol parameters. An example is the water vapor absorption at 2.1 μm which determines the surface reflectance for the red and blue channels. Without the correction of water vapor absorption, the surface reflectance at 2.1 μm will be underestimated, and consequently the aerosol optical thickness will be overestimated. The water vapor content obtained from two MODIS channels, one at solar and one at infrared spectral region, should be sufficient to provide the needed information. Cloud mask determination combines both MODIS shortwave and longwave channels of total of 13 channels. The process is quite complicated. One difficulty is to identify the clouds at various altitudes and the association with cloud thickness which can be semi-transparent or completely dark. If the cloud mask data is inefficient, the retrieval of aerosol optical parameters will be affected significantly. Additional cloud screening in regard to the neighboring pixels is also planned to include in the algorithm (see Appendix 2). This will be done after the cloud mask being applied. Because high cirrus cloud can be highly transparent, its contamination also affects the retrieval of aerosol. We plan to subtract the cirrus effect based upon its signature at 1.37 μm.

There is also a feedback circle between aerosol and water vapor. To determine the water vapor content, a certain aerosol optical thickness needs to be assumed. However, the water vapor content is also needed in the aerosol retrieval. One simple way of solving this is to iterate based upon the relationship between water vapor and aerosol estimated by the model until the convergence is reached. The final solution of aerosol amounts will be used to retrieve the water vapor content. Stratospheric aerosol effect will also be assessed for the occurrence of any major volcanic eruption. One example of stratospheric aerosol mode has already been shown in biomass burning measured in Amazon region in 1993 (Fig. 16) after the Mt. Pinatubo eruption.

Especially for aerosol over the ocean, wind speeds and chlorophyll contents are important to determine the reflectance over the ocean. The wind speed is closely correlated with the foam formation and its coverage over the ocean, and the chlorophyll contents will change the ocean reflectance through the water leaving radiance. As described before, the wind speed input to the algorithm will be obtained from assimilated data from DAO (Data Assimilated Office in NASA Goddard Space Flight Center) and the chlorophyll content will be from other MODIS channels that are used to derive this information.

6.3 Level 2 and 3 Products

There will be one single HDF file for Land and Ocean L2 product output file. First 9 parameters are common to both Land and Ocean, next 15 are for Land and 30 for Ocean only. In all there are 54 variables

Land and Ocean:(9)

1. Longitude
2. Latitude
3. Scan-start-time
4. Solar zenith
5. Solar-Azimuth
6. Sensor zenith
7. Sensor Azimuth
8. Cloud mask-QAcarried tram Mod35.Quality Assurance flags
9. Optical thickness of land and ocean at 0.55um

Land(15)
1. Aerosol-Type:
2. Scattering Angle:
3. Optical thickness for continental model at wavelengths of .470 um and .659 um:
4. Optical thickness for desired/corrected model at wavelengths of 0.470, 0.550 and 0.659 um.:
5. Estimated uncertainty of optical thickness at 0.47 and 0.66 micro:
6. Mass concentration:
7. Angstrom exponent for 0.47 and 0.67 um:
8. Normalized at 0.47 and 0.66 um:
9. Normalized transmitted flux at 0.47 and 0.66 um:
10. Cloud fraction in percentage:
11. Dust aerosol weighting factor:
12. Number of pixels with desired percentile:
13. Mean reflectance at five bands of 0.47, 0.659, 0.865, 2.130 and 3.75 um:
14, Standard deviation of reflectance at five bands of 0.47, 0.659, 0.865, 2.130 and 3.75 um:
15. Quality Assurance run time QA flags:.

Ocean(30)
1. Solution number small indicating index of small particles used in Solution from LUT:
2. Solution number large indicating index of large particles used in solution from LUT:
3. Scattering angle
4. Aerosol optical thickness: best solution (defined in documentation) for 7 wavelengths 0.47, 0.659, 0.865,,1.64 and 2.13 um with mixed modes:
5. Aerosol optical depth: _average_ solution for 7 bands with mixed modes:
6. Aerosol optical depth: _best_ solution for 7 bands with small particles:
7. Aerosol optical depth: _average_ solution for 7 bands with small particles:
8. Aerosol optical depth: _best_ solution for 7 bands with large particles
9. Aerosol optical depth: _average_ solution for 7 bands with large particles:
10. Mass concentration:

11. Effective radius at 0.55 um of both best and average solution:
12. CCN, column number of CCN at 0.55um at both best and average solutions:
13. Asymmetry factor for 7 bands for best solution:
14. Asymmetry factor for 7 bands for average solution:
15. Back scattering ratio at 7 bands for best solution:
16. Back scattering ratio at 7 bands for average solution:
17. Angstrom exponent for 0.55 and 0.865 um:
18. Angstrom exponent for 0.865 and 2.13 um:
19. Normalized reflected flux at 7 bands for best solution:
20. Normalized reflected flux at 7 bands for average solution:
21. Normalized Transmitted flux at 7 bands for best solution:
22. Normalized Transmitted flux at 7 bands for average solution:
23. Least square error, smallest residual error between two modes:
24. Small mode weighting factor derived between small and large mode combination:
25. Ratio:
26. Cloud fraction in percentage:
27. Number of total pixels used for 0.55um for retrieval:
28. Mean reflectance at 7 bands:
29. Standard deviation of reflectance's at 7 bands:
30. Quality flag: run time QA flags:

The level 3 products will be gridded into daily, 8-day and monthly averaged data based upon the level 2 data. Shown below are the level 3 products for aerosols, including a single aerosol product of POLDER 18 km gridded daily data, and 0.5° equal area gridded daily data and 0.5° equal angle and area gridded 8 days and monthly data compiled with water vapor and cloud products.

- POLDER 18 km grid daily data
- 0.5° equal area daily gridded data
- 0.5° equal area 8 days gridded data
- 0.5° equal area monthly gridded data
- 0.5° equal angle 8 days gridded data
- 0.5° equal angle monthly gridded data

Note that the 0.5° equal area gridded daily product is for use in 3-dimensional climate and chemistry modeling, and the POLDER 18 km gridded daily data is mainly used for atmospheric correction, which is more appropriate to be included as a product of MODIS land.

7. DISCUSSION AND CONCLUSIONS

7.1 Ocean

The present comparison of the field experiment data with the retrieved aerosol parameters is very encouraging. Testing the algorithm with actual data has left us with one problem in the present scheme. The uniformity of the aerosols layer within the box, aerosol content or aerosol type, can be a problem, even at the scale of 10x10 km. The testing procedure has also shown us that the choice of the width of the size distribution σ is not crucial as long as the right values of the effective radius are included.

Additional issues, although not discussed here, have also to be addressed in the future. When volcanic eruptions occur, like the most recent Pinatubo eruption in June 1991, they inject a large amount of aerosols within the stratosphere. Already a few weeks after an eruption, the stratospheric component can be larger than the tropospheric signal that we are analyzing and a correction has to be made. It could be done using external data like the data provided by SAGE sensor series or the 1.37 μm channel on MODIS for cirrus and stratospheric aerosols detection (Gao and Kaufman, 1995). The number of cloud-free pixels within the box is also an important question, what is the maximum percentage of cloud-cover we accept for making the inversion? A compromise has to be found for still performing good retrieval and for not applying too restrictive conditions.

The present study has confirmed the potential of MODIS for retrieving the aerosols parameters like the optical thickness and the asymmetry parameter, the domination of the accumulation or coarse mode, and to a lesser extend the exact ratio between the modes, and the size of the main mode. When the spectral measurements are very well fitted, i.e. when the right model is included in the LUT, then the optical thickness is very well retrieved. In this regard, ε_{min} values are a good indicator of the quality of the retrieval. The size of particles is also fairly well monitored as shown by the results obtained for the different aerosols types.

The quality of the inversion strongly depends on the quality of inputs used to build the LUT. Surface contribution is a major issue, the spectral reflectance of the foam has to be accurately determined, wind speed estimated from General Circulation Model, and water-leaving radiance should be preferably estimated from MODIS itself or at least from standard ocean color maps. Glint mask has to be efficient since glint uncertainty will results in very large errors. The AERONET sunphotometers network has to be maintained and extended for a better characterization of the aerosol particles.

The philosophy we adopted to build our algorithm has been shown quite adequate. After its validation, the aerosol information which will be derived from MODIS are very well adapted for studying the aerosol climatology, i.e. to monitor the sources, the transport and the sinks of specific aerosol types, the interaction of aerosol with water vapor and clouds (both monitored by MODIS) and finally their radiative forcing.

7.2 Land

After the launch of the MODIS sensors on the EOS system, daily or twice daily aerosol optical thicknesses will be operationally derived over the land (as well as over the ocean) and used to derive the aerosol columnar volume distribution and radiative forcing. Despite the difficulties to derive aerosol over the land, it is expected that using dark targets, identified by their reflectance in the mid-IR, the aerosol optical thickness, τ_a, can be sensed with an error estimated to be $\Delta\tau_a=0.05\pm0.2\tau_a$ over the moist parts of the continents, regions where a large part of the human activity takes place. Radiative forcing by aerosol is also stronger for low surface albedo (e.g. water and vegetation). Therefore we expect the algorithm to report aerosol loading and forcing in continental regions close to the main anthropogenic sources.

For efficient remote sensing of aerosol optical thickness over the land and for estimation of the volume concentration and radiative forcing several new remote sensing elements were developed and implemented: the use of mid-IR (2.1 μm and 3.7 μm) to identify surface pixels that are dark in the red and blue channels and to estimate their reflectance; the use of dynamic aerosol models to describe the aerosol size distribution and scattering phase function, (in these models the aerosol parameters depend on the optical thickness); and the use of weighted averages (rather than arithmetic averages) of aerosol climatology in order to derive the aerosol parameters for specific fixed scattering angles in order to minimize errors from uncertainty in the aerosol scattering phase function. The derivation of the optical thickness over the land will use a continuous validation procedure, updating periodically the algorithm by using aerosol properties derived from the AERONET global measurements. Substantial experience and validation was gained with the AVHRR 3.7 μm channel for identification of dense dark vegetation as the dark targets. Comprehensive evaluation of the 2.1 μm technique is still in progress.

The daily or twice a day (after the launch of the second EOS system in 2000) aerosol information over land and oceans combined with continuous detailed aerosol remote sensing of aerosol from the ground by AERONET and in situ measurements, will be used to study aerosol climatology, to monitor the sources and sinks of specific aerosol types, to study the interaction of aerosol with water vapor and clouds (both monitored by MODIS) and their radiative forcing of climate. It will also be used for atmospheric corrections of remotely sensed surface reflectance over the land (Tanré et al., 1992, Running et al., 1994). We found that for scattering angles around 150° the errors in the derived parameters are smaller. The error in the derived volume of the accumulation mode is smaller than that of the optical thickness of that mode. Radiative forcing can be derived with errors of ±20% even with a large uncertainty in the particles size (0.1-3 μm). Detailed validation of the algorithm both before and after the EOS launch are planned to quantify the errors in different parts of the world and in order to continue and improve the algorithm.

Appendix 1

Optical properties

• (i) the asymmetry factor is defined by

$$g_\lambda = \int \mu \, P_\lambda(\mu) \, d\mu \qquad \text{(Eq. A-1)}$$

where $P_\lambda(\mu)$ is the aerosol phase function. The asymmetry factor of the total size distribution is obtained from

$$g_\lambda = \qquad \text{(Eq. A-2)}$$

where g^s_λ and g^l_λ are the asymmetry factors of each mode, $\omega^s_{0\lambda}$ and $\omega^l_{0\lambda}$ the single scattering albedo's and τ^s_λ and τ^l_λ the optical thicknesses.

• (ii) The backscattering ratio β_λ is defined by

$$\beta_\lambda = \int \mu^{-1} \, P_\lambda(\mu) \, d\mu \qquad \text{(Eq. A-3)}$$

The backscattering ratio of the total size distribution is then obtained from

$$\beta_\lambda = \qquad \text{(Eq. A-4)}$$

where β^s_λ and β^l_λ are the backscattering ratio of each mode

Physical properties

• (i) the moments M_k of order k are defined by

$$M_k = \int r^k \, n(r) \, dr \qquad \text{(Eq. A-5)}$$

which, for a log-normal distribution, gives

$$M_k = = r^k \exp\left\{ k^2 \ln^2(\sigma) \right\} \qquad \text{(Eq. A-6)}$$

It allows us to compute the effective radius r_{eff} and the effective variance of the size distribution which are respectively given by,

$$r_{eff} = \qquad \text{(Eq. A-7-a)}$$

$$\sigma_{eff} = \qquad \text{(Eq. A-7-b)}$$

• (ii) the number of particles per cm^3 of each mode, N^s and N^l, are given by the ratio between the optical thickness and the extinction coefficient computed for 1part. cm^{-3}.

• (iii) the number of Cloud Condensation Nuclei of the small mode, N_{CCN}, is defined by, $\quad N_{CCN} = N^s \int n^s(r) \, dr = N^s \, 0.5 \, (1 - erf(A)) \qquad$ (Eq. A-8)

where $r_0 = 0.03 \mu m$ and A=

Appendix 2

Cloud-free pixel selection in regard to neighboring pixels

The purpose is to select pixels that have at least X cloud-free neighboring pixels (X: the number of cloud-free neighboring pixels), and also to reject pixels on the edges of the scan except for X=0 (see below). In other words, cloud-free pixels are chosen based upon the surrounding pixels that are cloudy or not. For the central pixel (pixel 5 as shown below), for example, whether or not it is selected depends upon the given criterion of the pixels 1-9 within 500 m range, or the surrounding 24 pixels within 1.0 km range, or the surrounding 80 pixels within 2.0 km range. For some channels with finer resolution, more pixels will be used. Missing data, dead detectors, and reflectance value less than or equal to zero will be treated as cloudy pixels. As a result, larger number of cloud-free surrounding pixels reflect better quality of the aerosol parameters retrived.

1	2	3
4	5	6
7	8	9

- X=0; all pixels are considered whether the neighboring pixels are cloudy or not.
- X=4; neighboring pixels 2, 4, 6, 8 are cloud free.
- X=8; neighboring pixels 1 - 9 are cloud free (i.e., within 500 km range).
- X=24; neighboring pixels are cloud free within 1.0 km range.
- X=80; neighboring pixels are cloud free within 2.0 km range.

REFERENCES

Ahmad Z. and R.S. Fraser, An iterative radiative transfer code for ocean-atmosphere system, *J. Atmos. Sci.,* 39, 656-665, 1982.

d'Almeida, G.A., R. Jaenicke, P. Roggendorf and D. Richter, 1983. New Sunphotometer for network operation. *Appl. Opt. 22(23)*:3796-3801.

d'Almeida G. A., On the variability of desert aerosol radiative characteristics, *J. Geophys. Res.* 93, 3017–3026, 1987.

d'Almeida G.A., Koepke P. and E.P. Shettle, Atmospheric Aerosols, Global Climatology and Radiative Characteristics, Deepak Publishing, Hampton, Virginia, 1991.

Andreae, M.O., 1995: Climatic effects of changing atmospheric aerosol levels Ch 10 in *World Survey of Climatology . Vol 16: Future Climates of the World,* Ed. A. Henderson-Sellers, pp. 341-392, Elsevier, Amsterdam

Andreae, M.O., 1996: Raising dust in the greenhouse, Nature*, 380* ,389-390.

Andreae M.O. and W.R. Barnard, 1984, The marine chemistry of dimethylsulfide, Marine Chemistry, 14, 267-279.

Boucher, O. and T.L. Anderson, 1995: GCM assessment of the sensitivity of direct climate forcing by anthropogenic sulfate aerosols to aerosol size and chemistry, *J. Geophys. Res., 100,* 26117-26134.

Bowker, D.E., R.E. Davis, D.L. Myrick, K. Stacy and W.T. Jones, 1985: Spectral reflectances of natural targets for use in remote sensing studies, NASA Reference Publication 1139.

Carlson T.N., 1979: Atmospheric Turbidity in Saharan dust outbreaks as determined by analyses of satellite brightness data, Mon. Wea. Rev., 107, 322-335.

Chahine, M.T., 1972, A general relaxation method for inverse solution of the full radiative transfer equation, J. Atmos. Sci., 29, 741-747.

Charlson, R.J., J.E. Lovelock, M.O. Andreae and S.G. Warren, 1987, Oceanic phytoplankton, atmospheric sulphur, cloud albedo and climate, Nature, 326, 655-661.

Charlson, R.J., S.E. Schwartz, J.M. Hales, R.D. Cess, J.A. Coackley, Jr., J.E. Hansen and D.J. Hofman, 1992, Climate forcing of anthropogenic aerosols, Science, 255, 423-430.

Coakley, J.A., Jr., R. L. Bernstein and P. A. Durkee, 1987: Effect of ship stack effluents on cloud reflectance. *Science, 237,* 953-1084.

Coakley, J. R. D. Cess and F. B. Yurevich, 1983: The effect of tropospheric aerosol on the earth's radiation budget: a parametrization for climate models. *J. Atmos. Sci.,* 40, 116-138.

Coakley, J. A. Jr. and R.D. Cess, 1985, Response of the NCAR community climate model to the radiative forcing by the naturally occurring tropospheric aerosols, J. Atmos. Sci., 42, 1677-1692.

Cox, C. and W. Munk, Statistics of the sea surface derived from sun glitter, *J. Mar. Res.,* 13, 198-208, 1954.

Crutzen, P.J., 1983, Atmospheric interaction-Homogeneous gas reactions of C,N, and S containing compounds, pp 67-114, In B. Bolin and R.B. Cook (eds.), The major biogeochemical Cycles and their interactions, Wiley, New-York.

Crutzen, P.J. and Andreae, M.O., 1990: Biomass burning in the tropics: impact on atmospheric chemistry and biogeochemical cycles, *Science, 250,* 1669-1678.

Deschamps, P.Y, F.M. Bréon, M. Leroy, A. Podaire A. Bricaud, J.C. Buriez, and G. Sèze, The POLDER mission: Instrument Characteristics and Scientific Objectives, *IEEE Transactions on Geoscience and Remote Sensing,* 32, 598-615, 1994.

Deuzé J.L., F.M. Bréon, P.Y. Deschamps, C. Devaux, M. Herman, A. Podaire and J.L. Roujean, 1993: Analysis of the POLDER (Polarization and Directionality of Earth's Reflectances) Airborne Instrument, *Rem. Sens. Environ.*, 45, 137-154.

Diner D. J. et al., MISR: A Multiangle Imaging SpectroRadiometer for Geophysical and Climatological Research from EOS, *IEEE Trans. on Geos. and Rem. Sens.,* 27, 200-214, 1989.

Duce R.A., 1983, Biogeochemical Cycles and the Air-Sea Exchange of Aerosols, In B. Bolin and R.B. Cook (eds.), The major biogeochemical Cycles and their interactions, Wiley, New-York.

Dulac F., D. Tanré, Bergametti G, Buat-Menard P., Desbois M., Sutton D., Assessment of the african airborne dust mass over the western Mediterranean sea using Meteosat data, J. Geophys. Res., 97, 2489-2506, 1992.

Durkee P.A., Aerosol Characteristics with Dual Wavelength Radiance Measurements, in Preprints 2nd Conference on Satellite Meteorology, *Remote Sensing and Applications, Amer. Meteo. Soc., Boston,* 1985.

Durkee, P.A., D.R. Jensen, E.E. Hindman, and T.H. Vonder Haar, 1986: The relationship between marine aerosols and satellite detected radiance. *J. Geophys. Res.,* 91, 4063-4072.

Durkee, P.A., F. Pfeil, E. Frost, and R. Shema, 1991: Global analysis of aerosol particle characteristics. Atmos. Environ., 25a, 2457-2471.Fairall, C.W., Davidson K.L. and Schacher G.E., 1983, An analysis of the surface production of sea-salt aerosols, Tellus, 35B, 31-39.

Flowers, E.C., R.A. McCormick and K.R. Kurfis, 1969. Atmospheric turbidity over the United States, 1961-1966, *J. of Applied Meteor. 8 ,* 955-962.

Forgan B.W., E.N. Rusina, J.J. DeLuisi and BB Hicks, 1994, Measurements of Atmospheric Turbidity in BAPMoN and Looking Forward to GAW, WMO report.

Fraser R.S., Satellite measurement of mass of Saharan dust in the atmosphere, *Appl. Opt.*, 15, 2471-2479, 1976.

Fraser, R.S. and Y.J. Kaufman, 1985: 'The relative importance of aerosol scattering and absorption in remote sensing', *IEEE J. Geosc. Rem. Sens., GE-23*, 525-633.

Fraser R.S. ,Y.J. Kaufman and R.L. Mahoney, 1984 "Satellite measurements of aerosol mass and transport", Atmos. Environ., vol. 18, pp. 2577-2584.

Fraser R.S., R.A. Ferrare, Y.J. Kaufman and S. Mattoo, 1992: 'Algorithm for atmospheric corrections of aircraft and satellite imagery', *Int. J. Rem Sens.* 13, 541-557.

Fraser R.S., R.A. Ferrare, Y.J. Kaufman and S. Mattoo, 1992: 'Algorithm for atmospheric corrections of aircraft and satellite imagery', *Int. J. Rem Sens. 13,* 541-557.

Frouin R., M. Schwindling and P.Y. Deschamps, Spectral Reflectance of Sea Foam in the Visible and Near-Infrared: In-situ Measurements and Implications for Remote Sensing of Ocean Color and Aerosols, *J. Geophys. Res.*, in press, 1996.

Gao, B.C. and Y.J. Kaufman, Selection of the 1.375µm MODIS channel for remote sensing of Cirrus clouds and stratospheric aerosols from space, *J. Atmos. Sci.,* 52, 4231-4237, 1995.

Gordon, H.R., Diffuse reflectance of the ocean: the theory of its augmentation by chlorophyll *a* fluorescence at 685nm, *Appl. Opt.*, 18, 1161-1166, 1979.

Gordon, H. R. and D.J. Castano, 1989: 'Aerosol analysis with the CZCS: A simple method for including the multiple scattering effects', Appl. Opt., <u>28</u>, 1320-1326.

Gordon, H.R., Atmospheric correction of ocean color imagery in the EOS Era, *J. Geophys. Res.,*, this issue, 1996.

Griggs, M, Measurements of atmospheric aerosol optical thickness over water using ERTS-1 data, J. Air Pollut. Control Ass., 25, 622-626,.1975.

Griggs M., Satellite observations of atmospheric aerosols during the EOMET cruise, J. Atmos. Sci., 36, 695-698, 1979.

Hansen J.E. and A.A. Lacis, 1990, Sun and dust versus greenhouse gases: an assessment of their relative roles in global climate change, Nature, 346, 713-719.

Hansen, J. E. and L. D. Travis, 1974: Light scattering in planetary atmospheres. *Space Science Reviews*, **16**, 527-610.

Hao, W. M. and M. H. Liu, 1994, Spatial and temporal distribution of tropical biomass burning, Global Biogeochem. Cycles, 8, 495-503.

Heathershaw A. D., 1974, Bursting phenomena in the sea, Nature, 248, 394-395.

Hegg, D.A., 1990, Heterogeneous production of cloud condensation nuclei in the marine atmosphere, Geophys. Res. Lett. 17, 2165-2188

Hegg, D.A., Ferek, R.J. and Hobbs, P.V., 1993, J. Geophys. Res., <u>98</u>, 8841-8846.

Hegg, D.A. P.V. Hobbs, R.J. Ferek and A. P. Waggoner, Measurements of some aerosol properties relevant to radiative forcing on the east coast of the United States, *J. Appl. Meteor.*, 34, 2306-2315, 1995

Hidy, G.M., 1984, Aerosols: An Industrial and Environment Science, Academic Press Inc. (London) Ltd., 24/28 Oval Road, London NW1 7DX, pp774.

Hobbs, P.V. and J.D. Locatelli, 1970, Ice nucleus measurements at three sites in Western Washington, J. Atmos. Sci., 27, 90-100.

Hobbs, P.V., J.S. Reid, J.A. Herring, J.D. Nance, R.E. Weiss, J.L. Ross, D.A. Hegg, R.D. Ottmar and C. Louisse, 1996: Particle and trace gas measurements in the smoke from prescribed burns of forest products in the Pacific Northwest, Submitted to Global *Biomass Burning,*, The MIT press, Cambridge MA.

Holben B.N., Y.J Kaufman, A. Setzer, D. Tanré and D. Ward, Optical properties of aerosol emissions from biomass burning in the tropics - BASE-A, in *Global Biomass Burning: Atmospheric, Climate and Biospheric Implications*, edited by J. Levine, MIT press, Cambridge, Massachusetts, pp 403-411, 1991.

Holben B.N., T.F. Eck and R.S. Fraser, 1991: Temporal and spatial variability of aerosol optical depth in the Sahel region in relation to vegetation remote sensing, *Int. Rem. Sens.*, *12*, 1147-1163.

Holben B.N., T.F Eck, I. Slutsker, D. Tanré, J.P. Buis, A.Setzer, E. Vermote, J.A. Reagan, Y.J. Kaufman, T. Nakajima, F Lavenu and I. Jankowiak, Multi-Band Automatic

Sun and Sky Scanning Radiometer System for Measurements of Aerosols, *Rem. Sens. Environ.*, in press, 1996.

Holben B.N., Vermote E., Kaufman Y.J., Tanré D., Kalb V., Aerosols retrieval over land from AVHRR data- Application for atmospheric correction, IEEE Transactions on Geoscience and Remote Sensing, 30, 212-222, 1992.

Hoppel W. A., Fitzgerald J.W., Frick G.M., Larson R.E. and E.J. Mack, 1990: Aerosol size distribution and optical properties found in the marine boundary layer over the Atlantic ocean, J. Geophys. Res., 95,3659-3686.

Hidy, G.M., Aerosols: An Industrial and Environment Science, *Academic Press Inc. (London) Ltd.*, 24/28 Oval Road, London NW1 7DX, pp774, 1984.

Hoppel W. A., Fitzgeral J.W., Frick G.M., Larson R.E. and E.J. Mack, Aerosol size distribution and optical properties found in the marine boundary layer over the Atlantic ocean, J. Geophys. Res., 95,3659-3686, 1990.

Husar, R. B., L.L. Stowe and J. Prospero, 1996: Patterns of tropospheric aerosols over the oceans, *Bull. Amer. Meteor. Soc.* to be submitted.

IPCC, Intergovernmental Panel on Climate Change, 1995, Radiative Forcing of Climate Change, Cambridge University Press, New York.

Jaenicke R. and L. Schütz L., 1978, Comprehensive study of physical and chemical properties of the surface aerosols in the Cape Verde Islands region, J. Geophys. Res.., 83, 3585-3599.

Jankowiak I. and D. Tanré, 1992: Climatology of Saharan dust events observed from Meteosat imagery over Atlantic Ocean. Method and preliminary results, *J. Clim., 5,* 646-656.

Jones, A., D.L. Roberts and A. Slingo, 1994: A climate model study of indirect radiative forcing by anthropogenic sulphate aerosols, *Nature, 370,* 450-453.

Joseph, 1984, The sensitivity of a numerical model of the global atmosphere to the presence of desert aerosol, In Aerosols and their climatic effects, Eds. H.E. Gerber and A. Deepak, Hampton, Virginia, Deepak Publishing, 215-226.

Junge C.E. , 1963: <u>Air chemistry and radiochemistry</u>, Academic Press, New York, 382 pp.

Kahn, R., R. West, D. McDonald and B. Rheingans, 1996: Sensitivity of multi-angle remote sensing observations to aerosol sphericity, this issue.

Kaufman Y.J., 1993: 'Measurements of the aerosol optical thickness and the path radiance - implications on aerosol remote sensing and atmospheric corrections', J. Geophys. Res. <u>98</u>, 2677-2692.

Kaufman Y.J., 1995: Remote Sensing of the Direct and Indirect Aerosol Forcing, in *Aerosol Forcing of Climate*, Eds. Charlson and Heintzenberg, pp 298-332, Wiley, England.

Kaufman Y.J., and M.-D. Chou, 1993: 'Model simulations of the competing climatic effects of SO_2 and CO_2', *J. of Climate* **6,** 1241-1252.

Kaufman Y.J., R.S. Fraser, 1996, Effect of smoke on increase in cloud reflectivity - remote sensing over the Amazon forest and the Cerrado", submitted to JGR.

Kaufman Y.J., R.S. Fraser and R.A. Ferrare, 1990 "Satellite measurements of large-scale air pollution methods", J. Geoph. Res., vol. 95(D7), pp. 9895-9909.

Kaufman, Y.J. , R.S. Fraser and Mahoney, 1991, Fossil fuel and biomass burning effect on climate-Heating or cooling?, J. Clim., 4, 578-588.

Kaufman, Y. J. and B. N. Holben, 1996: Hemispherical Backscattering By Biomass Burning And Sulfate Particles Derived From Sky Measurements", accepted to special issue of *J. Geophys. Res.,-Atmospheres* on Carbonaceous Aerosol.

Kaufman, Y.J., A. Gitelson, A. Karnieli, E. Ganor, R.S. Fraser, T. Nakajima, S. Mattoo, B.N. Holben, 1994: 'Size Distribution and Phase Function of Aerosol Particles Retrieved from Sky Brightness Measurements', JGR-Atmospheres, in press.

Kaufman, Y.J. and T. Nakajima, 1993, Effect of Amazon Smoke on Cloud Microphysics and Albedo - Analysis from Satellite Imagery, J. Appl. Meteor., 32, 729-744.

Kaufman, Y. J. and L. Remer, 1994: 'Remote Sensing of Vegetation in the mid-IR: the 3.75 μm channels', *IEEE J. Geosc. and Rem. Sens. 32*, 672-683.

Kaufman Y.J. , L. A. Remer, R. D. Ottmar, D. E. Ward, R.-R. Li, R. Kleidman, R. S. Fraser, L. Flynn, D. McDougal and G. Shelton, Relationship between remotely sensed fire intensity and rate of emission of smoke: SCAR-C experiment, *Proceedings of the 'Chapman Conference on Biomass Burning and Global Change'*, March 13-17, 1995, Wiliamsburg, Virginia, USA, in press, 1996

Kaufman, Y. J. and C. Sendra, 1988: 'Algorithm for atmospheric corrections', Int. J. Rem. Sens., 9, 1357-1381.

Kaufman, Y.J., A. Setzer, D. Ward, D. Tanré, B.N. Holben, P. Menzel, M.C. Pereira and R. Rasmussen, 1992: Biomass Burning Airborne and Spaceborne Experiment in the Amazonas (BASE-A), *J. Geoph. Res, 97,* 14581-14599.

Kaufman, Y.J., A. Setzer, D. Ward, D. Tanré, B.N. Holben, P. Menzel, M.C. Pereira and R. Rasmussen, 1992: Biomass Burning Airborne and Spaceborne Experiment in the Amazonas (BASE-A), *J. Geoph. Res, 97,* 14581-14599.

Kaufman, Y. J., D. Tanré: 1994: Variations in cloud supersaturation and the aerosol indirect effect on climate, *Nature, 369*, 45-48, 1994.

Kaufman, Y. J., D. Tanré: 1996: Direct and Indirect Methods for Correcting the Aerosol Effect on Remote Sensing, *Rem. Sens. of Environ.*, 55, 65-79, 1996.

Kaufman, Y. J. , C. J. Tucker and I. Fung, 1990: Remote Sensing of Biomass Burning in the Tropics, *J. Geoph. Res.*, *95*, 9927-9939.

Kaufman, Y.J., A. Wald, L.A. Remer, B-.C. Gao, R.-R. Li and L. Flynn, 1996: Remote sensing of aerosol over the continents with the aid of a 2.2 μm channel", submitted to IEEE TGARS, April 1996

Kiehl, J.T., and B.P. Briegleb, 1993: 'The relative roles of sulfate aerosols and greenhouse gases in climate forcing', Science, 260, 311-314.

King, M. D., 1979: Determination of the ground albedo and the index of absorption of atmospheric particulates by remote sensing, Part II: Application, *J. Atmos. Sci. 36*, 1072–1083.

King, M.D., 1982, Sensitivity of constrained linear inversions to the selection of the Lagrange multiplier, J. Atmos. Sci., 39, 1356-1369.

King, M.D., D.M. Byrne, B.M. Herman and J.A. Reagan, 1978, Aerosol size distribution obtained by inversion of optical depth measurements, J. Atmos. Sci., 35, 2153-2167.

King, M.D., Kaufman Y., Menzel P., Tanré D., 1992, Remote sensing of Cloud, Aerosol and Water Vapor properties from the Moderate Resolution Imaging

Spectrometer (MODIS), IEEE Transactions on Geoscience and Remote Sensing, 30, 2-27, 1992.

Koepke, P. Effective reflectance of oceanic whitecaps, *Appl. Opt.*, 23, 1816-1823, 1984.

Koepke, P. and M. Hess, Scattering functions of tropospheric aerosols: the effects of nonspherical particles, *Appl. Opt.*, 27, 2422-2430, 1988.

Koepke P. and H. Quenzel, Turbidity of the atmosphere determined from satellite calculation of optimum viewing geometry, J. Geophys. Res., 84, 7847-7855, 1979.

Langner, J., H. Rodhe, P.J. Crutzen and P. Zimmermann, 1993: 'Anthropogenic influence on the distribution of tropospheric sulphate aerosol', Nature, 359, 712-715

Lenoble, J. and C. Brogniez, 1984: A comparative review of radiation aerosol models, Britr. Phys. Atmosph. Vol. 57, No. 1, -20.

Lee, T. and Y.J. Kaufman, 1986: 'The effect of surface non-Lambertianity on remote sensing of ground reflectance and vegetation index', *IEEE J. Geosc. Rem. Sens.,* GE-24, 699-708.

Li, X., H. Maring, D. Savoie, K. Voss and J.M. Prospero, 1996: Dominance of mineral dust in aerosol light scattering in the North Atlantic trade winds, *Nature, 380* ,416-419.

Liou, K.N., K.P. Freeman and T. Sasamori, 1978, Cloud and aerosol effects on the solar heating rate of the atmosphere, Tellus, 30, 62-70.

Martins, J. V., P. Artaxo, C. Liousse, H. Cachier, Y. Kaufman and A. P. Fattori, Size distribution, elemental composition, carbon measurements and calculated optical properties of biomass burning aerosol particles during the SCAR-C experiment, submitted *Global biomass burning,*, The MIT press, Cambridge MA, 1996.

Martonchik J.V. and D.J. Diner, Retrieval of Aerosol Optical Properties from Multi-Angle Satellite Imagery, *IEEE Transactions on Geoscience and Remote Sensing*, 30, 223-230, 1992.

Mekler Y., H. Quenzel, G. Ohring, and I. Marcus, "Relative atmospheric aerosol content from ERTS observations", J. Geoph. Res., vol. 82, pp. 967-972,1977.

Mészáros, E., 1981, Atmospheric Chemistry - Fundamental Aspect, Studies in Environmental Science 11, Elsevier Scientific Publishing Company, P.O. Box 330, Amsterdam, The Netherlands, pp201.

Mishchenko M. I. and L. D. Travis, Light scattering by polydispersions of randomly oriented spheroids with sizes comparable to wavelengths of observation, *Appl. Opt.,* 33, 7206-7225, 1994

Mishchenko M. I. , A. A. Lacis, B. E. Carlson and L. D. Travis, Nonsphericity of dust-like tropospheric aerosols: implications for aerosol remote sensing and climate modeling, *Geophys. Res. Lett.*, 22, 1077-1080, 1995

Morel, A. and L. Prieur, Analysis of variations in ocean color, *Limnol. and Oceanogr.*, 22, 709-722, 1977.

Nakajima, T., M. Tanaka and T. Yamauchi, 1983: Retrieval of the optical properties of aerosols from aureole and extinction data. *Appl. Opt. 22*, 2951-2959.

Nakajima, T., T. Takamura, M. Yamano, M. Shiobara, T. Yamauchi, R. Goto, and K. Murai, 1986: Consistency of aerosol size distribution inferred from

measurements of solar radiation and aureole. *J. Meteor. Soc. of Japan,* <u>64</u>, 765-776.

Nakajima, T., M. Tanaka, M. Yamano, M. Shiobara, K. Arao and Y. Nakanishi, 1989: Aerosol optical characteristics in the yellow sand events observed in May, 1982 at Nagasaki-Part 2 Models, *J. Meteor. Soc. of Japan, 67, 279-291.*

Norton C.C.,F.R. Mosher,B. Hinton, D.W. Martin, D. Santek and W. Kuhlow, A model for calculating desert aerosol turbidity over oceans from geostationary satellite data, J. Appl. Meteor., 19, 633-642, 1980.

Penner, J. E., R.E. Dickinson, C.A. O'Neill, 1992: Effects of aerosol from biomass burning on the global radiation budget, *Science*, <u>256</u>, 1432-1434.

Petterson, J.T., E.C. Flowers, G.J. Berri, C.L. Reynolds and J.H. Rudisill, 1981: Atmospheric turbidity over central North Carolina, *J. Appl. Meteor., 20*, 229-241.

Prins, E.M. and W.P. Menzel, 1994: Trends in South American biomass burning detected with the GOES VISSR radiometer atmospheric sounder from 1983 to 1991, *J. Geoph. Res, 99*, 16719-16735.

Prospero, J.M., 1981, Eolian transport to the world ocean, The sea, Vol VII, The Oceanic Lithosphere, Ed. C. Emiliani, Wiley, New-York, 801-874.

Prospero, J. M., and R. T. Nees, 1986: Impact of the North African drought and El Niño on mineral dust in the Barbados trade wind, *Nature, 320*, 735-738.

Payne, R.E., Albedo of the sea surface, *J. Atmos. Sci.*, 29, 959-960, 1972.

Pye, K., 1987, Eolian Dust and Dust deposit, Academic Press, London, pp335.

Radke, L.F., L.F., J. A. Coakley and M.D. King, 1989: Direct and remote sensing observations of the effect of ships on clouds, *Science*, **246**, 1146-1149.

Radke, L. F., D. A., Hegg, P. V. Hobbs, J. D. Nance, J. H. Lyons, K. K. Laursen, P. J. Reagan and D.E. Ward, 1991: Particulate and trace gas emission from large biomass fires in North America, *Global biomass burning,* p. 209-224, The MIT press, Cambridge MA.

Rao, C.R.N., E.P. McClain and L.L. Stowe, "Remote-Sensing of aerosols over the oceans using AVHRR data theory, practice and applications", Int. J. Remote Sens., vol. 10, pp. 743-749, 1989.

Remer L.A., S. Gasso, D. Hegg, Y.J. Kaufman and B.N. Holben, Urban/Industrial aerosols: Ground-Based Sun/Sky Radiometer and Airborne in Situ Measurements, *J. Geophys. Res.,*, this issue, 1996a.

Remer, L. A., Y. J. Kaufman, and B. N. Holben, The size distribution of ambient aerosol particles: smoke vs. urban/industrial aerosol, accepted to *Global Biomass Burning,*, The MIT press, Cambridge MA, 1996b.

Roger, J.C. and E.F. Vermote, 1996: Computations and use of the reflectivity at 3.75 μm from AVHRR thermal channels, Rem. Sens. of Environ. in press.

Running, S.W., C.O. Justice, V. Salomonson, D. Hall, J. Barker, Y.J. Kaufman, A.H. Strahler, A.R. Huete, J.P. Muller, V. Vanderbilt, Z.M. Wan, P. Teillet and D. Carneggie, 1994: Terrestrial remote sensing science and algorithms planned for EOS/MODIS", *Int. J. Rem. Sens., 15*, 3587-3620.

Salomonson V.V., W.L. Barnes, P.W. Maymon, H.E. Montgomery and H. Ostrow, 1989, MODIS: Advanced Facility Instrument for Studies of the Earth as a System,I EEE Trans. on Geos. and Rem. Sens., 27, 145-153, 1989.

Santer B. D., K. E. Taylor, T. M. L. Wigley, T. C. Johns, P. D. Jones, D. J. Karoly, J. F. B. Mitchell, A. H. Oort, J. E. Penner, V. Ramaswamy, M. D. Schwarzkopf, R. J. Stouffer an S. Tett, 1996, A search for human influences on the thermal structure of the atmosphere, Nature, Vol. 382, 39-46.

Shettle E.P., 1984, Optical and radiative properties of a desert aerosol model, *Proc. Symposium on Radiation in the Atmosphere, G. Fiocco Ed.*, A. Deepak Publishing, 74-77.

Shettle E.P., and R.W. Fenn, "Models for the aerosol of the lower atmosphere and the effect of humidity variations on their optical properties", AFGL-TR 790214, Opt. Phys. Div., Air Force Geoph. Lab., Hanscom AFB MA, 1979.

Shiobara, M., T. Hayasaka, T. Nakajima and M. Tanaka, 1991. Aerosol Monitoring using a Scanning Spectral Radiometer in Sendai, Japan, *J. Meteor. Soc. Japan,* 69, 57-70.

Schubert S., R. Rood and J. Pfaendtner, An Assimilated Dataset for Earth Science Applications, *Bull. Am. Met. Soc.,* 74, 2331-2342, 1993.

Shettle E.P., Optical and radiative properties of a desert aerosols model, *IRS'84: Current problems in atmospheric Radiation, Eds, G. Fiocco, A. Deepak Pub.,* Hampton, Virginia,, pp 243, 1984.

Shettle E.P., and R.W. Fenn, Models for the aerosol of the lower atmosphere and the effect of humidity variations on their optical properties, AFGL-TR 790214, Opt. Phys. Div., *Air Force Geoph. Lab.,* Hanscom AFB MA, 1979.

Sokolik, I.N. and O.B. Toon, 1996: Direct radiative forcing by anthropogenic airborne mineral aerosol, *Nature, 381,* 681-683.

Soufflet V., Tanré D., Royer A., 1996: Remote Sensing of aerosols over boreal forest and lake from AVHRR/NOAA data, *Rem. Sens. Environ.*, submitted.

Tanré D., J.F. Geleyn and J. Slingo, 1984, First results of the introduction of an advanced aerosol-radiation interaction in ECMWF low resolution global model, In Aerosols and their climatic effects, Eds. H.E. Gerber and A. Deepak, Hampton, Virginia, Deepak Publishing, 133-177.

Tanré D., P.Y. Deschamps, C. Devaux and M. Herman, Estimation of Saharan aerosol optical thickness from blurring effects in Thematic Mapper data, *J. Geophys. Res.*, 15955-15964, 1988a.

Tanré D., C. Devaux, M. Herman, R. Santer and J. Y. Gac, Radiative properties of desert aerosols by optical ground-based measurements at solar wavelengths. *J. Geophys. Res.,* 83, 14,223-14,231, 1988b.

Tanré D., B.N. Holben and Y.J. Kaufman, 1992, Atmospheric correction algorithm for NOAA-AVHRR products, theory and application, *IEEE J. Geosc. Rem. Sens.,* 30, 231-248.

Tanré D., M. Herman, Y.J. Kaufman, Information on the Aerosol Size Distribution contained in the Solar Reflected Spectral Radiances, *J. Geophys. Res.*, in press, 1996.

Tanré D., Y.J. Kaufman, M. Herman and S. Mattoo, 1996: Remote senisng of aerosol over oceans from EOS-MODIS, submitted to JGR-atmospheres special issue on remote sensing of aerosol and atmospheric corrections .

Tanré, D., L.A. Remer, Y.J. Kaufman, S. Mattoo, P.V. Hobbs, J.M. Livingston, P.B. Russell and A. Smirnov, 1999: Retrieval of aerosol optical thickness and size

distribution over ocean from the MODIS Airborne Simulator during TARFOX, *J. Geophys. Res.*, *submitted*,.

Taylor G.S., M.B. Baker and R.J. Charlson, 1983, Heterogeneous Interactions of the C, N and S cycles in the atmosphere: the role of Aerosols and clouds, In B. Bolin and R.B. Cook (eds.), The major biogeochemical Cycles and their interactions, Wiley, New-York.

Tegen, I., A.A. Lacis and I. Fung, 1996: The influence on climate forcing of mineral aerosols from disturbed soils, Nature*, 380 ,419-422.

Travis L.D., EOSP: Earth Observing Scanning Polarimeter, EOS reference Handbook 1993, *G. Asrar and D.J. Dokken Ed.*, NASA, Washington DC, 74-75,1993.

Twomey, S.A, 1977b, Introduction to the mathematics of inversion in remote sensing and indirect measurements, Developments in Geomathematics, 3, Elsevier Scientific Publishing Company, P.O. Box 330, Amsterdam, The Netherlands, pp243.

Twomey, S.A., and J. Warner, 1967, Comparison of measurements of cloud droplets and cloud nuclei, J. Atmos. Sci., 24, 702-703.

Twomey, S.A., M. Piepgrass and T.L. Wolfe, 1984, An assessment of the impact of pollution on the global albedo, Tellus 36b, 356-366.

Van de Hulst, 1957, Light Scattering by Small Particles, J. Wiley & Sons, Inc., N.Y., reprinted in 1981 by Dover Pub., Inc., 180 Varick Street, New York, N.Y., 10014.

Vermote, E., N. El Saleous, C. Justice, Y. J. Kaufman, L. A. Remer, J.C. Roger, and D. Tanré, 1996: Atmospheric correction of visible to middle infrared EOS-MODIS data over land surface, background, operational algorithm and validation., submitted to JGR-atmospheres special issue on remote sensing of aerosol and atmospheric corrections March. 1996

Volz, F., 1954. Himmelslicht und atmospharische Trubung. Wetter und Leben 6:99-104.

Wang, M., and H. R. Gordon, 1993: 'Retrieval of columnar aerosol phase function and single scattering albedo from sky radiance over the ocean: simulations', Appl. Opt., 32, 4598-4609.

Wang M. and H.R. Gordon, Radiance reflected from the ocean-atmosphere system: Synthesis from individual components of the aerosols size distribution, *Applied Optics*, 33, 7088-7095, 1994.

Whitby K.Y., The physical characteristics of sulfur aerosols, *Atmos. Environ.*, 12, 135-159, 1978

Whitlock C. H., D.S. Bartlett and E.A. Gurganus, Sea foam reflectance and influence on optimum wavelength for remote sensing of ocean aerosols, *Geophys. Res. Let* ., 9, 719-722, 1982.

Wigley, T.M.L, 1989: Possible climate change due to SO_2 derived cloud condensation nuclei, Nature, 339, 355-357.

Wiscombe W.J. and A. Mugnai, Scattering from nonspherical Chebyshev particles. 2: Means of angular scattering patterns, *Appl. Opt.*, 27, 2405-2421, 1988.

WMO, 1983: Radiation commission of IAMAP meeting of experts on aerosol and their climatic effects, WCP55, Wiliamsburg VA, 28-30 March, 1983.